UNIVERSITÀ DEGLI STUDI DI BERGAMO
DEPARTMENT OF ENGINEERING AND APPLIED SCIENCES
DOCTORAL PROGRAMME IN ENGINEERING AND APPLIED SCIENCE

CORROSION BEHAVIOR OF ADVANCED AND RECOVERED MATERIALS FOR AGGRESSIVE INDUSTRIAL ENVIRONMENTS

Doctoral dissertation of:

Tommaso Persico

Tutor:

Prof.essa Marina Cabrini

Supervisor:

Prof. Tommaso Pastore

The chair of the Doctoral Program:

Prof.essa Alessandra Marini

COLOPHON

This doctoral thesis was developed within the PhD Programme in Engineering and Applied Science at the University of Bergamo.

This research was funded by the European Union, NextGenerationEU program: MICS – Made in Italy circolare e sostenibile, spoke 6.04 Development of new alloys with improved properties and decreased environmental impact for AM powder production.

Parts of this thesis are based on published or submitted scientific works authored by the candidate, as listed in the Appendix.

Tommaso Persico, 2026

Table of contents

List of Acronym **1**

Preface **1**

Context of the PhD project and MICS – Made in Italy Circolare e Sostenibile (Spoke 6.04) **2**

Thesis overview **1**

Chapther 1. General introduction **3**

1.1 Metal AM: techniques and applications **3**

1.2 Corrosion and material selection in geothermal sectors **8**

1.3 Opportunities and sustainability in geothermal sectors through AM **10**

Chapther 2. Additively manufactured materials for geothermal sectors **13**

2.1 Nickel-based superalloys **13**

2.1.1 Introduction **13**

2.1.2 Strengthening mechanisms **13**

2.1.3 The role of alloying elements **14**

2.1.4 Alloys for geothermal sectors **15**

2.2 Titanium alloys: classification and corrosion behavior **16**

2.2.1 Introduction **16**

2.2.2 Titanium alloy classification **18**

2.2.3 Alloys for reducing acid environments **19**

2.3 AM of titanium alloys **22**

2.4 Powder metallurgy for AM **25**

2.5 Standard and qualification of metal obtained by means of AM **28**

Chapther 3. Case study I: geothermal turbine blades made of nickel-based alloys **30**

3.1 Chapter introduction **30**

3.2 Materials and methods **30**

3.2.1 Materials **30**

3.2.2 Microstructural analysis **31**

3.2.3 Corrosion tests 32
3.3 Results and discussion 32
3.3.1 Condition of blades after operation 32
3.3.2 Mechanism and cause of material degradation 34
3.4 Conclusion and perspective on the material selection obtained through AM 39
Chapther 4. Alloy 625 produced by different AM technologies 41
4.1 Chapter introduction 41
4.2 Materials and methods 41
4.2.1 Materials 41
4.2.2 Microstructural investigation 44
4.2.3 Hardness test 44
4.2.4 Electrochemical corrosion tests 44
4.2.5 Intergranular corrosion test 45
4.2.6 Immersion corrosion test in sulfuric acid 45
4.3 Results and discussion 46
4.3.1 Microstructural investigation and defects characterization 46
4.3.2 Hardness 50
4.3.3 Intergranular corrosion 51
4.3.4 Electrochemical corrosion tests 54
4.3.5 Corrosion in acidic media 56
4.4 Conclusion 59
Chapther 5. Development and qualification of Alloy 725 for AM 61
5.1 Chapter introduction 61
5.2 Materials and methods 61
5.2.1 Feedstock production 61
5.2.2 Optimization of process parameters of LPBF process for Alloy 725 62
5.2.3 Materials 63
5.2.4 Microstructural analysis 65

5.2.5 Hardness test 65
5.2.6 Tensile tests 65
5.2.7 Electrochemical corrosion tests 65
5.2.8 Intergranular corrosion test 66
5.3 Results and discussion 66
5.3.1 Microstructural analysis 66
5.3.2 Mechanical behavior 69
5.3.3 Susceptibility to selective corrosion 71
5.3.4 Corrosion behaviors in chloride acidic environments 73
5.4 Conclusion 75
Chapther 6. Field exposure test of super nickel alloys obtained by means of AM 77
6.1 Chapter introduction 77
6.2 Materials and methods 77
6.2.1 Test chamber and exposure conditions 77
6.2.2 Materials, specimens and microscopy analysis 78
6.3 Results and discussion 80
6.4 Conclusion 85
Chapther 7. Case study II: degradation of titanium alloys in geothermal environments 86
7.1 Chapter introduction 86
7.2 Materials and methods 86
7.2.1 Material 86
7.2.2 Microscopic analysis 89
7.2.3 Hardness testing 90
7.2.4 Hydrogen content analysis 90
7.3 Results and discussion 90
7.3.1 Tube condition 90
7.3.2 Mechanism and cause of fracture 94
7.4 Conclusion 99

Chapther 8. Corrosion behavior of titanium alloys in reducing acidic media produced by AM technologies 100

8.1 Chapter introduction 100

8.2 Materials and methods 101

8.2.1 Materials 101

8.2.2 Microscopic analysis 104

8.2.3 Hardness testing 104

8.2.4 Immersion tests for generalized corrosion in acidic media 104

8.2.5 Immersion tests for localized corrosion 104

8.3 Results and discussion 105

8.3.1 Microstructures and mechanical behavior 105

8.3.2 Generalized corrosion behavior in boiling HCl 108

8.3.3 Localized corrosion behavior in boiling $MgCl_2$ 111

8.4 Conclusion 113

Conclusions and future perspectives 115

General conclusions 115

Limitation of the study 115

Future research and perspectives 116

List of figures 119

List of tables 124

Bibliography 125

Annex ..... Errore. Il segnalibro non è definito.

Indexes ..... Errore. Il segnalibro non è definito.

List of Acronym

Acronym	Meaning
AM	Additive Manufacturing
BJ	Binder Jetting
BM	Base Material
DED	Directed Energy Deposition
DwP	Dew Point
EAC	Environmentally Assisted Cracking
EIS	Electrochemical Impedance Spectroscopy
FESEM	Field Emission Scanning Electron Microscopy
FZ	Fusion Zone
HE	Hydrogen Embrittlement
HW	Hot Worked
LC	Laser Cladding
LPBF	Laser Powder Bed Fusion
MEX	Material Extrusion
OM	Optical Microscopy
OCP	Open Circuit Potential
PH	Precipitation Hardened
PREN	Pitting Resistance Equivalent Number
SCC	Stress Corrosion Cracking
SKPFM	Scanning Kelvin Probe Force Microscopy
UTS	Ultimate Tensile Strength
XRD	X-Ray Diffraction

Preface

This doctoral thesis addresses the study of the corrosion behavior of novel alloys developed for Additive Manufacturing (AM) in aggressive industrial environments. The research activity focused on materials for geothermal energy systems due to the presence of combination of high temperatures, aggressive chemical species, and acidic and reducing fluids.

The thesis investigates the two families of metals commonly employed in the harshest condition for geothermal sectors: nickel-based superalloys and titanium-based materials. The experimental work first introduces both material families through failure analyses to present and study the mechanism of the most critical degradation phenomena that could occur.

Subsequently, the research focuses on the investigation of these materials when produced via AM technologies, adopting different approaches depending on the material system under study. Alloy 625, which is already widely used in AM, was analyzed by comparing different AM technologies in order to deepen the understanding of these emerging production routes and to assess their influence on material behavior.

Alloy 725, which is relatively new to the AM field, was instead selected for a complete material recovery cycle. End-of-life components are processed to obtain reusable feedstock, which is subsequently employed for AM. The newly produced material was characterized in the laboratory and tested directly under the original service operating conditions of the dismissed component. The results are promising and lay the foundation for the integration of closed-loop materials in geothermal sectors through AM.

Finally, titanium-based alloys were investigated and compared under reducing acidic conditions, which represent the most critical environments for the stability of their protective oxide layer. The results enable a comparison between different additively manufactured materials with titanium Grade 5 and its enhanced corrosion version (Grade 29), in order to evaluate their corrosion resistance.

Context of the PhD project and MICS – Made in Italy Circolare e Sostenibile (Spoke 6.04)

This doctoral research was included in the Italian National Recovery and Resilience Plan (PNRR), as part of the MICS – Made in Italy Circolare e Sostenibile research program. MICS is funded by the Ministry of University and Research and is divided into 48 applied research activities developed within the 8 Spokes. The aim of the MICS is to strengthen the competitiveness and sustainability of Italian industry. This doctoral research belongs to Spoke 6.04 which focuses on the development of new alloys with improved properties and reduced environmental impact for AM powder production. Within the scope of this Spoke, the present PhD project is positioned at the final stage of the research chain. While other project partners were primarily involved in the production of new powders from waste materials and in the development of novel alloys, the aim of this PhD project was the characterization and qualification of novel materials produced by means of AM for industrial aggressive environments.

Thesis overview

This doctoral thesis investigated the corrosion behavior of novel materials developed for AM in highly aggressive industrial environments. The main industrial sector considered in this study is geothermal energy, which shows significant interest in AM technologies for applications characterized by severe operating conditions.

As a first step, the work presented two case studies of failure that occurred in geothermal applications, focusing on the two main families of materials commonly adopted in aggressive environments: nickel-based superalloys and titanium alloys. These case studies highlighted the most critical degradation mechanisms that may arise in the geothermal sector. For nickel-based superalloys, inadequate material selection with respect to the aggressiveness of the geothermal fluid may lead to localized corrosion and stress corrosion cracking, whereas titanium alloys may be exposed to the risk of pitting corrosion or hydrogen embrittlement under unfavorable operating conditions.

The first experimental activity investigated how different AM technologies influence the microstructure, mechanical properties, and corrosion behavior of Alloy 625. The results demonstrate that AM technologies cannot be considered equivalent in terms of resulting material produced. The microstructure of Alloy 625 is strongly affected by the manufacturing process employed, which in turn influences both the mechanical and corrosion behavior of the material. Scanning Kelvin Probe Force Microscopy (SKPFM) analyses further revealed that AM routes not only affect the distribution of carbides, but also their nature, thereby significantly altering the susceptibility to intergranular corrosion. Among the analyzed technologies, LPBF and DED emerged as the most promising AM routes for producing Alloy 625, yielding materials with good mechanical properties and no evidence of sensitization. Binder Jetting showed promising potential but further effort is required in process and post-process to obtain a material comparable to fusion-based AM.

In addition, the thesis explored the feasibility of qualifying advanced materials produced by AM through a complete material recovery cycle. Starting from ex-service turbine blades in Alloy 725 from a geothermal plant, the material was atomized and reused as feedstock for the LPBF process to produce new specimens for qualification.

The recovered material exhibited excellent mechanical properties already in the as-built condition, however the best mechanical properties was achieved after precipitation hardening. Corrosion testing in acidic chloride-containing environments showed excellent behavior comparable to the original material. LPBF-manufactured specimens showed a higher susceptibility to intergranular corrosion but the primary cause of sensitization was associated with the precipitation-hardening treatment.

Field exposure tests were designed to replicate the environmental operating conditions experienced by turbine blades under Dew Point (DwP) conditions. The results validated Alloy 725 produced by LPBF, both as-built and precipitation hardened, and Alloy 625 produced by DED as excellent materials for turbine blades operating in direct-cycle geothermal plants. These outcomes open relevant industrial perspectives for the implementation of advanced materials and more sustainable manufacturing routes in the production of geothermal system components.

Corrosion tests in reducing acidic media on titanium-based material indicated that AM does not exhibit significant alterations in corrosion behavior when compared with their conventionally manufactured counterparts. Instead, alloy chemical composition is crucial to governing corrosion resistance under reducing acidic conditions. In particular, aluminum was found to be detrimental to corrosion performance; while alloying elements such as niobium, molybdenum, and ruthenium significantly enhance the stability of the passive oxide layer and improve resistance to degradation in aggressive environments. The Ti-6Al-2Sn-4Zr-6Mo alloy exhibited a corrosion behavior comparable to reference alloy specifically designed for high corrosion resistance in reducing environments, demonstrating its suitability as the most promising candidate for such applications.

On the other side, titanium aluminides showed that a high aluminum content compromises the stability of the protective oxide. However, the Ti-48Al-2Cr-8Nb alloy exhibited unexpected performance in boiling magnesium chloride solution, suggesting further investigation may be worthwhile for evaluate this material for applications in moderately acidic environments.

Chapther 1. General introduction

1.1 Metal AM: techniques and applications

It is important to recognize that AM does not represent a single processing route, but rather a family of technologies characterized by significantly different energy sources, thermal histories, and consolidation mechanisms. The general terminology and principles of AM are defined in ISO/ASTM 52900:2021, while process qualification guidelines are addressed in ISO/ASTM 52920. According to ISO/ASTM standards, AM technologies are classified into seven main categories based on the bonding mechanism and feedstock type. Among these, four process families are currently most relevant for metallic AM, namely Powder Bed Fusion (PBF), Directed Energy Deposition (DED), Material EXtrusion (MEX) and Binder Jetting (BJ) [1].

While the specific material deposition strategy, bonding mechanism, and feedstock type vary depending on the AM process considered, all technologies share a layer-by-layer construction approach. As a consequence, materials produced by different AM routes may exhibit markedly different microstructural features, defect populations, and material properties, even when the same nominal alloy composition is employed [2].

One of the most established industrial AM technologies for metallic materials is Powder Bed Fusion. This technology can be further divided into two main variants depending on the energy source employed. When a laser beam operating in an inert gas atmosphere is used, the process is referred to as Laser Powder Bed Fusion (LPBF). In LPBF, a thin layer of metallic powder is selectively melted according to the component geometry. After solidification, a recoater spreads a new powder layer over the build surface, and the process is repeated in a layer-by-layer manner until the final component is obtained (Figure 1).

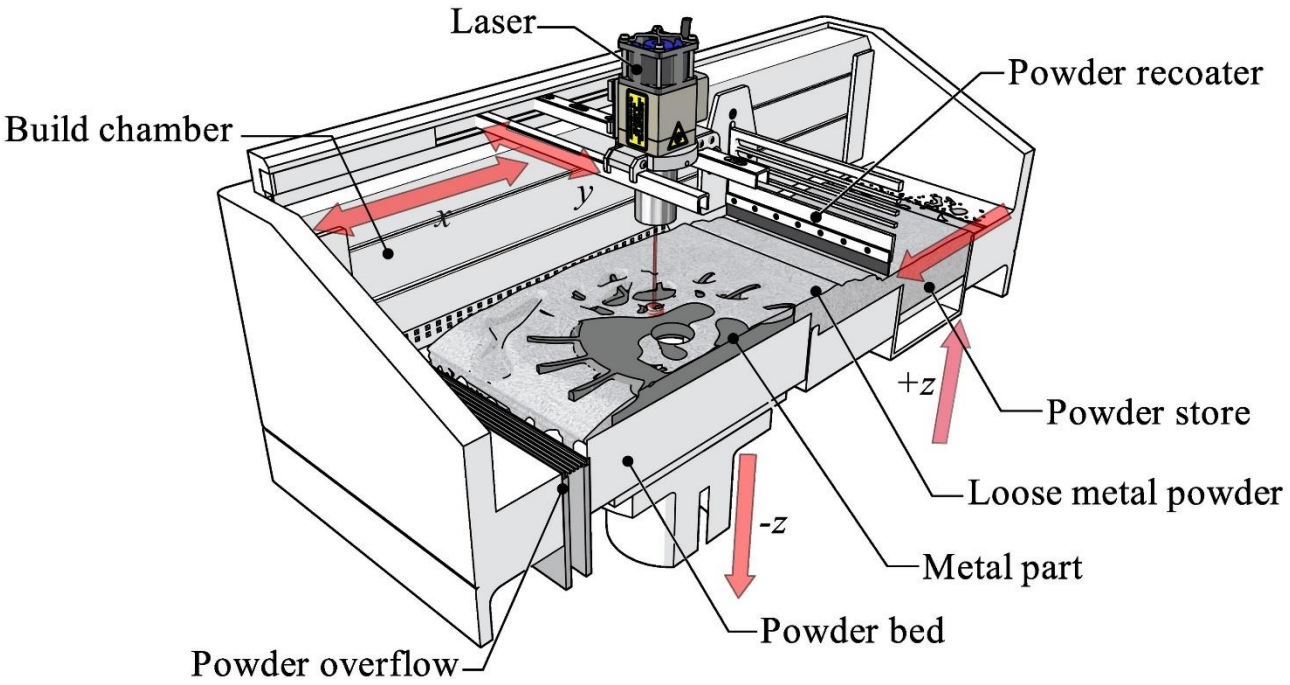

Figure 1 - Schematic of a LPBF machine [1].

When the energy source consists of an electron beam, the process is known as Electron Beam Powder Bed Fusion (EBM). In contrast to LPBF, EBM operates under vacuum conditions rather than in an inert gas atmosphere. The use of an electron beam allows higher beam power and larger melt pools, and the powder bed is typically preheated to elevated temperatures. This results in lower thermal gradients and reduced residual stresses compared to LPBF, but also leads to coarser microstructures and lower geometric resolution. Overall, PBF are technologies that stand out from the others AM techniques by with high dimensional accuracy and relatively low surface roughness, making it particularly suitable for complex, high-precision parts [3,4].

Directed Energy Deposition (DED) technologies are also widely adopted in industrial application such as remanufacturing, cladding and repair operations. In DED, the metallic feedstock (powder or wire) is deposited directly on the surface of a substrate where a focused energy source, laser or electron beam, create a melt pool. Material is deposited and consolidated in a single step, enabling the direct fabrication or modification of components.

Compared to powder bed fusion systems, DED offers significantly higher deposition rates and greater flexibility in terms of component size. These characteristics make DED particularly suitable for the manufacturing of large-scale components, the addition of functional features onto existing parts, and the repair or refurbishment of high value-added components. In addition, the capability to deposit material locally allows DED to be effectively integrated into hybrid manufacturing routes combining additive and subtractive processes.

However, DED processes generally result in lower geometric resolution and inferior surface finish compared to powder bed systems due to a larger melt pools spot. Therefore, post-processing steps such as machining are often required to achieve the desired dimensional accuracy and surface quality. Despite these limitations, its suitability for cladding and remanufacturing operations makes DED highly relevant for sectors characterized by severe service conditions and costly materials, where extending component lifetime and enabling material recovery can provide significant economic and sustainability benefits [1,5].

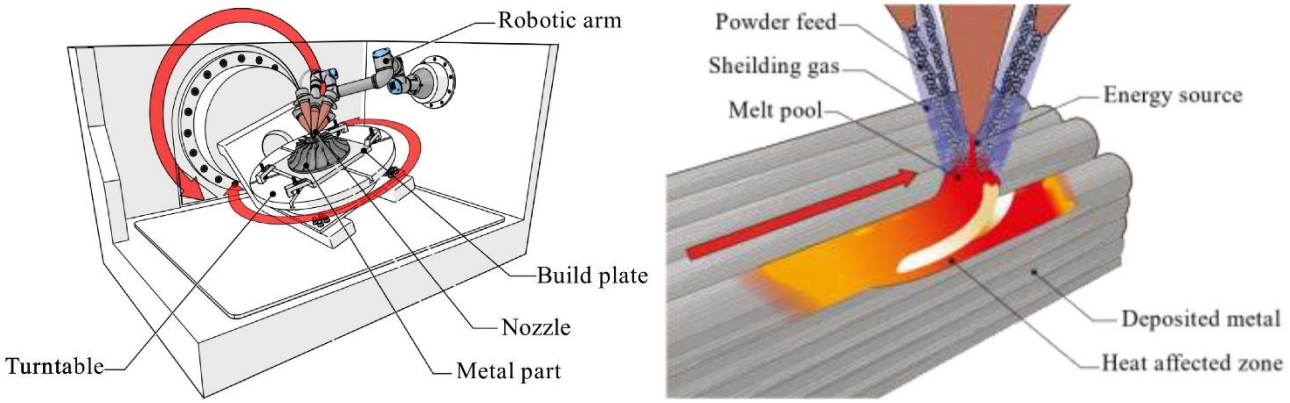

Figure 2 - Schematic of a DED machine [1].

Despite these differences, both LPBF and DED technologies share a common limitation: relatively low production rates, which can restrict their industrial competitiveness [4,6,7]. To address this challenge, a new generation of AM technologies for metallic materials has emerged, based on a fundamentally different printing concept.

In these approaches, metallic particles are not consolidated through melting during the printing stage. Instead, the shaping process relies on the use of a temporary binding phase, typically a polymeric binder, which holds the metal powders together in a so-called green part. By avoiding in-situ metal melting, these technologies significantly simplify the printing system, as they do not require controlled inert atmospheres, complex safety systems, or the precise management of a molten metal pool. As a result, printing equipment can be more cost-effective and operate under less stringent safety requirements [1,8,9].

Following the shaping step, the printed green parts undergo dedicated post-processing treatments, including debinding to remove the polymeric binder and sintering to achieve metallurgical bonding and densification of the metallic powders [8,10]. These sinter-based AM routes have therefore attracted increasing interest as a potential solution to improve production efficiency and reduce manufacturing costs, especially for applications where high geometric resolution is not the primary requirement.

Among these technologies, Material Extrusion (MEX) has gained particular attention. In MEX, a thermoplastic filament charged with metal powders is extruded and deposited layer by layer [9].

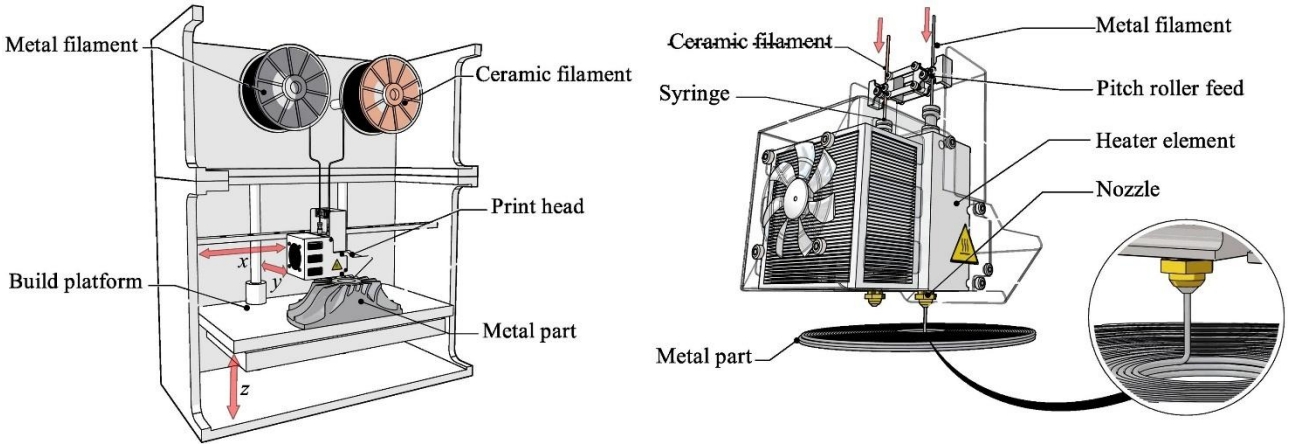

Figure 3 - Schematic of a MEX machine [1].

Despite the advantages associated with this approach, including simplified equipment and potentially higher productivity, previous studies have demonstrated that MEX-processed material may exhibit elongated and interconnected macro-defects with a periodic arrangement. These defects were shown to be strongly dependent on the deposition strategy, highlighting the need for careful process optimization and material qualification when sinter-based AM technologies are employed [9,11,12].

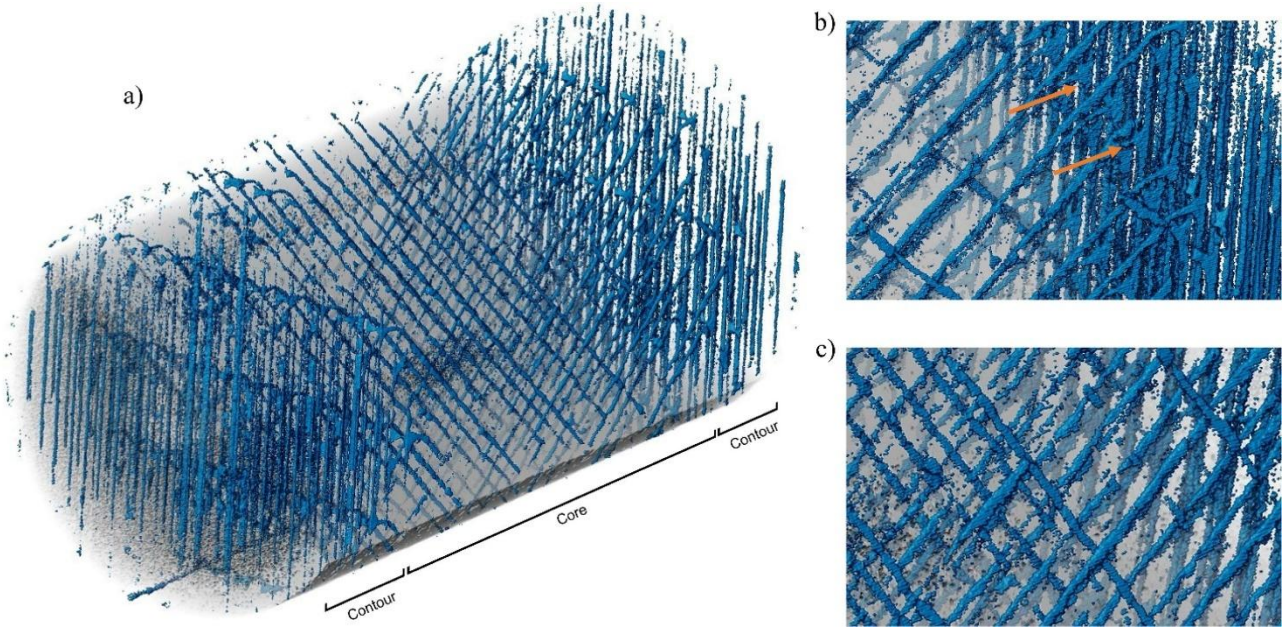

Figure 4 - 3D void structure of Alloy 625 produced by MEX [11]

Another promising metal-polymer AM technology is BJ, which consist in a powder bed, but instead of selectively melting the powder, a liquid binder is selectively deposited to locally bond the particles.

Despite MEX, BJ doesn't present macro-defects induced by the technology process. Nevertheless, also BJ still faces challenges in achieving full densification, as a technology less extensively studied than fusion-based AM routes [8,13,14]. Nowadays, research interest is focused on sintering parameter optimization and post-sintering infiltration, where a secondary metal is introduced into the open-pore network to improve density and structural integrity [8,15,16].

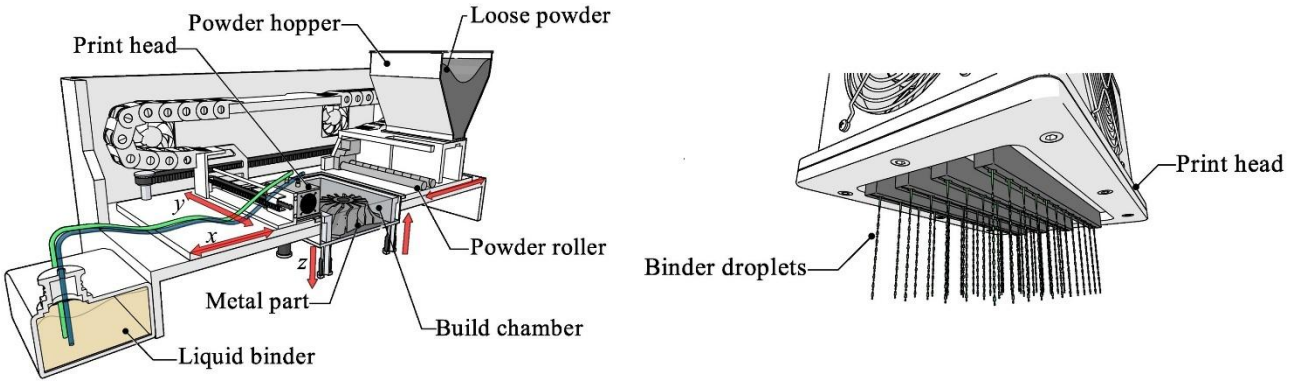

Figure 5 - Schematic of a typical BJ machine [1].

The key advantage of AM processes is the ability to produce components with complex forms without the constraints associated with traditional manufacturing like undercuts and internal cavities. In conventional subtractive manufacturing, the realization of such features limits the design, requires multiple machining steps, or the assembly of several parts [1].

Moreover, in AM the geometric complexity doesn't affect the production costs while in traditional manufacturing, the cost of a component increases with the complexity and the number of features in the object [2,17].

Despite these advantages, AM also presents intrinsic limitations. One of the major drawbacks is that it is not as efficient in mass production as conventional manufacturing technologies. Traditional processes such as casting, forging, or machining remain significantly more cost-effective and productive for large production volumes. Therefore, the decision between AM and traditional manufacturing methods is strongly dependent on the specific application requirements in terms of component complexity, production volume, and cost efficiency [3].

One major driver for the adoption of AM is the improvement of component performance through advanced design strategies such as topology optimization or the integration of internal cooling channels, which can enhance thermal management and mechanical efficiency in applications such as aerospace and energy systems [17].

The reduction of assembly steps through part consolidation in another winning application of AM for simplifying production processes by combining multiple components into a single additively manufactured part [18].

Weight reduction represents the most important reason of adoption of AM in sectors such as aerospace, race and automotive where optimized geometries and lattice structures can significantly decrease component mass while maintaining structural integrity [19].

AM also plays a crucial role in rapid prototyping and product development, as it eliminates the need for dedicated tooling. This capability supports innovation cycles and reduces time-to-market for new products[2].

The application of AM in industrial contexts must be supported by an appropriate material qualification strategy. As discussed above, AM includes multiple processes characterized by fundamentally different metallurgical mechanisms. These range from fusion-based routes involving extremely high solidification rates such as 10^5-10^6 K/s in the case LPBF and for Directed Energy Deposition, where lower cooling rates, typically in the range of 10^3-10^4 K/s, and more complex thermal cycles are involved. In contrast, sinter-based AM routes rely on powder consolidation through solid-state diffusion during post-processing heat treatments rather than rapid solidification from the melt [2,3,20].

As a consequence of these distinct processing conditions, additively manufactured materials can exhibit microstructures that are markedly different from those obtained through conventional manufacturing routes and are highly specific to both the alloy system and the selected AM technology. Such microstructures may include non-equilibrium phase distributions, characteristic grain morphologies, residual porosity, and heterogeneous defect populations. As further discussed in Chapter 2, these features can have a significant impact on the mechanical and corrosion properties of the material and, in some cases, may represent critical factors limiting component performance.

1.2 Corrosion and material selection in geothermal sectors

Geothermal energy systems represent one of the most aggressive industrial environments for metallic materials. Geothermal plants convert the heat stored in the subsurface into usable energy through different technological configurations, including direct-cycle and indirect-cycle power plants, as well as heat exchange systems for district heating [21,22]. The choice of the plant configuration strongly influences both the thermodynamic efficiency of the system, and the severity of the operating conditions [23,24].

1.2 - Corrosion and material selection in geothermal sectors

In direct-cycle geothermal power plants, geothermal fluids extracted from deep reservoirs are expanded directly in turbines to produce electricity. This configuration allows for maximum efficiency of a geothermal plant. In indirect-cycle systems, geothermal fluids transfer heat to a secondary working fluid through heat exchangers, reducing direct exposure of critical components to aggressive geothermal media [22].

Corrosion phenomena are not uniformly distributed throughout geothermal plants, but affect multiple components along the fluid path, including wells, piping, valves, turbines, and heat exchangers. Among these, the most severe conditions are regions where condensation occurs. In direct-cycle geothermal plants, this condition is reached during turbine expansion. Geothermal fluids are typically characterized by high temperatures and pressures, presence of chloride and dissolved gases such as carbon dioxide (CO_2) and hydrogen sulfide (H_2S). At the DwP, volatile species in the steam phase are transferred into the liquid phase, leading to the formation of highly aggressive condensate characterized by high salinity and low pH [25,26]. Moreover, DwP conditions are recognized as the most critical for erosion-corrosion in geothermal wells [27,28]. Under these conditions, the vapor can no longer be considered dry saturated steam but a two-phase fluid, which is sufficient to trigger erosion phenomena. Moreover, there is a synergic corrosion mechanism due to condensates with acidic pH values and high concentrations of chlorides [25].

Scaling and corrosion are interrelated phenomena in geothermal systems and represent a critical aspect of material degradation. Geothermal fluids often contain high concentrations of dissolved salts and minerals that may precipitate as pressure and temperature change [26,29]. As a result, deposits composed of corrosion products and mineral scales can form on metallic surfaces, particularly in piping, turbines, and heat exchange equipment. The composition and morphology of these deposits strongly depend on fluid chemistry and operating conditions [30]. The presence of deposits does not necessarily result in a protective effect. While compact and adherent scales may locally reduce uniform corrosion rates by acting as a diffusion barrier, they can promote localized corrosion in confined micro-environments between the metal and the scale [26,29]. Under-deposit corrosion have been reported on both steels and corrosion-resistant alloys exposed to geothermal fluids [25,31].

A wide range of metallic materials has been employed in geothermal applications, depending on the severity of the exposure conditions and economic considerations. Carbon steels and low-alloy steels are commonly used in less aggressive sections of geothermal plants, particularly where the formation of adherent corrosion product layers may provide partial protection. However, these materials are prone to uniform corrosion and scaling [32].

Stainless steels are widely employed in geothermal systems, particularly in piping, auxiliary components, and heat exchange equipment, due to their favorable balance between corrosion

resistance, mechanical properties, availability, and cost. Austenitic stainless steels are commonly selected for moderate geothermal environments, where operating conditions do not reach extreme levels of acidity or chloride concentration [30,32,33]. Infact, stainless steels are subjected to pitting and SCC when exposed to steam ad DWP condition [25]. Duplex stainless steels generally exhibit improved resistance to stress corrosion cracking compared to austenitic grades; however, their performance may still be limited under highly aggressive geothermal conditions [30,34].

For these reasons, the use of stainless steels in geothermal applications is typically restricted to environments where corrosion severity can be reasonably controlled or predicted. In more aggressive sections of geothermal plants, particularly those exposed to acidic condensates, DwP conditions, or high chloride activity, stainless steels are often replaced by corrosion-resistant alloys such as nickel-based alloys or titanium alloys [25].

Nickel-based alloys are selected for their excellent combination of mechanical strength and corrosion resistance; however, not all superalloys designed for high-temperature applications are suitable for geothermal service. Inadequate alloy selection may lead to localized corrosion or stress corrosion cracking under geothermal conditions [25,35].

Titanium and its alloys are extensively used in geothermal systems due to their generally excellent corrosion resistance, which is associated with the formation of a stable passive oxide film. Commercially pure titanium exhibits negligible corrosion rates in moderate geothermal environments, where acidity and chloride concentration remain limited [32,36]. However, under acidic and reducing conditions, the stability of the protective oxide layer may be compromised, leading to localized corrosion phenomena [37–39]. Nevertheless, titanium alloys may still be susceptible to hydrogen-related degradation mechanisms under specific service conditions, particularly in the presence of hydrogen sulfide or low-pH fluids.

The geothermal sector therefore represents a high value-added industrial field characterized by extreme operating conditions, where material performance is a critical factor for plant reliability and economic sustainability. This context provides a particularly demanding and representative framework for the investigation of corrosion behavior and for the qualification of advanced materials, as addressed in the following chapters of this thesis.

1.3 Opportunities and sustainability in geothermal sectors through AM

AM should be regarded not as a solution to intrinsic corrosion limitations of metallic materials, but rather as an enabling manufacturing technology whose relevance lies in technical innovation, sustainability, and economic viability. From an industrial perspective, AM may offer concrete

advantages for selected components characterized by complex geometries, high buy-to-fly ratios, or demanding machining operations. Typical examples include turbine blades, impellers, valve components, and downhole tool parts, for which conventional manufacturing would require extensive multi-axis machining and specialized tooling [40,41].

A comprehensive techno-economic assessment conducted by Polsky et al. investigated the applicability of AM for different components of geothermal plants and it becomes economically advantageous for parts with high geometric complexity, low production volumes, and opportunities for part consolidation. In particular, PBF technologies were shown to benefit when multiple components are produced within a single build [42,43].

Moreover, AM enable technical innovation of geothermal systems, particularly in the design and realization of components. A clear example is provided by the work of Kabirnajafi et al. [44], who designed and developed a compact, screw-type heat exchanger using LPBF, integrating complex internal helical channels that would be extremely difficult or impossible to obtain through subtractive processes. The proposed design eliminates the need for extensive soil excavation and long piping typically required for conventional geothermal heat exchangers, significantly simplifying installation procedures while reducing space requirements and potential leakage risks. On the same topic, Sabau et al. [45] designed and experimentally validated an additively manufactured counterflow heat exchanger operating under representative geothermal brine conditions, achieving significantly higher overall heat transfer coefficients compared to conventional shell-and-tube designs.

Compared with conventional subtractive manufacturing routes, AM technologies are characterized by significantly improved buy-to-fly ratios. This aspect is particularly interesting for expensive material such as nickel- and titanium-based alloys. By minimizing scrap generation, AM contributes to both economic benefits and a reduced environmental footprint [46,47].

AM also opens relevant opportunities for repair and refurbishment strategies. The possibility to restore locally degraded or worn regions of high-value components can extend service life and reduce the need for complete replacement [41]. This approach is particularly attractive in geothermal applications where components operate under severe conditions and material costs represent critical factors. In a detailed LCA of a nickel-based gas turbine burner repair, Walachowicz et al. [48] reported a reduction in global warming potential (GWP) of up to 85% and a primary energy demand decrease of 60% when using LPBF instead of conventional machining and welding. About geothermal sectors, Polsky et al. [42] identified DED as an opportunity to restore components thanks to the possibility to repair on-site or near-site, fewer size constraints, and greater flexibility for cladding and remanufacturing. Several industrial case studies reported in the literature demonstrate

the successful application of AM for the repair of high-value components affected by wear, corrosion or erosion, extending component service life while avoiding full replacement [6,41,49–51].

An additional economic and sustainability-related advantage offered by AM is the valorization of waste through the recovery and reprocessing of end-of-life components into new feedstock powders. Material recovery through AM consist of atomization of ex-service components to produce new powder that can be used as feedstock for AM techniques. This approach is particularly relevant for specialty alloys, which often need to be specifically commissioned and reduces dependency on primary raw material extraction. Raoufi et al. [52] conducted a LCA on nickel powder production for AM, demonstrating that the use of recycled feedstock can reduce the GWP by more than 96% than using virgin nickel and increase to 99.7% when combined with localized supply chains.

Despite these advantages, the widespread adoption of AM in geothermal applications requires further efforts. The limited availability of geothermal-grade alloys in AM form, combined with the need to qualify newly developed materials produced under non-conventional processing conditions, represents a key barrier. The unique thermal histories associated with AM may generate microstructures that differ significantly from conventional products, making dedicated studies on mechanical integrity and corrosion performance essential prior to industrial implementation.

Chapther 2. Additively manufactured materials for geothermal sectors

2.1 Nickel-based superalloys

2.1.1 Introduction

The term “superalloys” was introduced in the third decade of the twentieth century to describe a new class of metallic materials developed to meet emerging engineering demands for heat-resistant alloys exhibiting superior corrosion resistance and higher strength compared to conventional stainless steels. These requirements arose primarily from the rapid development of high-temperature technologies, particularly in aerospace and power generation sectors [53].

Superalloys can be broadly categorized according to their base element into iron-based, nickel-based, and cobalt-based systems. Among these, nickel-based superalloys represent the most versatile and highest-performing class and are therefore considered the reference materials for the most aggressive service environments. Iron-based superalloys offer more cost-effective solutions for intermediate operating conditions, while cobalt-based superalloys are generally reserved for niche applications where extremely high temperatures and wear condition are presents[54].

Nickel-based superalloys were initially developed to provide outstanding resistance to high-temperature degradation mechanisms, such as oxidation and creep. Currently, nickel-based superalloys account for more than 50% of the advanced components employed in modern aircraft engines, particularly in high-temperature regions where a combination of mechanical strength, creep resistance, and environmental stability is required. However, several alloys have also been specifically designed to exhibit excellent resistance to aqueous corrosion in aggressive environments, including acidic chloride-containing media. This factor has contributed to their application gas and oil equipment, power generation systems, chemical processing plants, heat exchanger tubing, nuclear reactors, marine components, and military and space technologies [55–57].

2.1.2 Strengthening mechanisms

Unlike other metallic material systems, such as titanium or aluminum alloys, nickel-based superalloys do not follow a standardized or normative classification scheme. Instead, they were developed to

address specific performance requirements rather than to conform to a unified compositional or phase-based classification. As a result, the main classification of these materials regards the strengthening mechanisms meaning solid solution or precipitation hardening [53].

In solid-solution strengthened nickel-based superalloys, mechanical strength is primarily derived from the presence of chromium, molybdenum, iron, tungsten, tantalium and cobalt dissolved in the γ matrix. These alloys are generally characterized by high microstructural stability, good weldability, and excellent resistance to corrosion and hot corrosion. Because they do not rely on fine precipitate distributions for strengthening, they are less sensitive to microstructural degradation phenomena such as precipitate coarsening or phase instability during long-term exposure at elevated temperatures. Representative examples of this family include Inconel 625, Hastelloy X, Alloy C-276 and Alloy C-22. These alloys are widely used in chemical processing, power generation, and geothermal applications, where resistance to corrosion and environmental degradation is often more critical than achieving the highest possible creep strength[53,55,58].

The precipitation hardenable class is characterized by the formation of finely dispersed precipitates that give exceptional mechanical properties. The main strengthening phase is γ′ $Ni_3(Al,Ti)$, while in some alloys, such as alloy 718, has an additional phase γ″ (Ni_3Nb) to contribute to strengthening mechanisms. Dislocation motion is effectively hindered by these coherent precipitates, which offer outstanding high-temperature strength, creep resistance, and fatigue performance. Alloys belonging to this category include the Nimonic series, Waspaloy, René alloys, Alloy 718, and Alloy 725. The application of precipitation-strengthened nickel-based superalloys is therefore preferred when high mechanical strength and creep resistance are required at elevated temperatures, such as in turbine disks, blades, and other load-bearing components operating under severe thermal and mechanical stresses[53,56,59].

2.1.3 The role of alloying elements

The material properties of nickel-based superalloys are primarily governed by the type and concentration of alloying elements which plays a specific role in determining mechanical strength, corrosion resistance, and microstructural stability. Nickel constitutes the base element and forms the continuous γ matrix, characterized by a face-centered cubic (FCC) crystal structure. This phase provides excellent ductility and structural stability over a wide temperature range and allows high solubility for many alloying elements [53].

Chromium is one of the most important alloying elements in nickel-based superalloys, it increases corrosion and oxidation resistance thank to the formation of a protective Cr_2O_3 layer on the surface.

Chromium contents typically range from approximately 18 to 23 wt.% in corrosion-resistant nickel-based superalloys, making it particularly important for applications involving oxidizing or chloride-containing environments [53,59].

The addition of molybdenum is commonly employed to enhance resistance to localized corrosion, particularly in environments that are reducing and acidic. It contributes to solid-solution strengthening of the γ matrix and significantly enhances resistance to pitting and crevice corrosion. Molybdenum contents high enough may cause topologically close-packed (TCP) phases to form, which can lead to decreased ductility and compromised long-term mechanical integrity [55].

Aluminum and titanium are often added in couple and are used as alloying elements to promote precipitation hardening. They promote the formation of the γ′ phase which plays a fundamental role in providing high-temperature strength and creep resistance [59].

Another alloying element commonly used to promote precipitation hardening is niobium. Its addition, typically in the range of 3–5 wt.%, is employed to achieve strengthening through the formation of γ″ precipitates. While this mechanism provides excellent mechanical properties, niobium may segregate during solidification or improper heat treatment leading to the formation of brittle intermetallic phases such as Laves phases [55].

Cobalt is frequently added to enhance high-temperature strength and maintain the γ matrix stability. In high-performance superalloys, it is commonly employed as a tuning element to balance mechanical properties and phase stability [53].

2.1.4 Alloys for geothermal sectors

Material selection for geothermal systems among nickel-based superalloys primarily focuses on the Ni-Cr-Mo alloy family, as the most critical requirement is excellent corrosion resistance, particularly in acidic environments with high chloride content[33]. Within this group, Alloy 625 (UNS N06625) represents the reference material for geothermal applications and is extensively used for piping systems, valve components, heat exchangers, and protective claddings [23,60,61]. Its high content of Cr and Mo provides outstanding resistance to localized corrosion and stress corrosion cracking [25,62].

Another alloy belonging to this family is Alloy 59 (UNS N06059), which features a higher molybdenum content, approximately 6 wt.% greater than Alloy 625, and does not contain niobium. The absence of Nb prevents the formation of certain secondary phases that enhance the mechanical properties but contributes to improved resistance to localized corrosion. As a result, Alloy 59 exhibits excellent corrosion resistance in aggressive acidic chloride-containing environments but remains a

solid-solution-strengthened alloy [63,64]. Excluding its high cost, it is a very good alternative to be used in the construction of geothermal facilities having highly saline brines.

For extremely aggressive geothermal conditions, especially in heat exchangers, piping, and chemical handling systems, Alloy C-276 (UNS N10276) can be adopted. It's a solution-strengthen Ni-Mo-Cr alloy with an addition of tungsten having excellent corrosion resistance in a wide range of severe environments. It's known for excellent resistance to pitting and crevice corrosion and good weldability thanks to low carbon content. Another excellent material for pitting and crevice resistance is Alloy C-22 (UNS N06022) which is a Ni-Mo-Cr alloy with reduced alloying element content to balance corrosion resistance and material cost [58,65,66].

However, solid-solution-strengthened alloys are not suitable for components subjected to high mechanical loads, such as turbine blades, except when employed as protective claddings. In this context, Brownlie et al. [23] demonstrated the excellent erosion-corrosion resistance of such alloys, highlighting their suitability for surface protection in geothermal applications.

When higher mechanical strength is required, precipitation-hardened nickel-based superalloys are adopted. Alloy 718 (UNS N07718), widely used in aerospace and high-temperature applications, is one of the most common precipitation-strengthened alloys and has also been tested in geothermal environments. Nevertheless, its lower molybdenum content makes it more susceptible to corrosion phenomena in aggressive geothermal conditions[25,67]. Although Alloy 718 is still employed in some geothermal applications, it is often used as a benchmark material rather than as a long-term solution in particularly aggressive environments. A more suitable alternative is Alloy 725 (UNS N07725), which was specifically designed to combine high mechanical properties with enhanced corrosion resistance through an optimized Cr-Mo balance. Compared to Alloy 718, Alloy 725 exhibits superior resistance to localized corrosion and environmentally assisted cracking in acidic reducing environments, making it more appropriate for critical geothermal components operating under DwP conditions [25].

2.2 Titanium alloys: classification and corrosion behavior

2.2.1 Introduction

Titanium and its alloys have different properties that make it interesting for various industrial sectors. This metal is characterized by low density, excellent strength-to-weight ratio, good fatigue resistance and excellent corrosion behavior [68].

2.2 - Titanium alloys: classification and corrosion behavior

The industrial interest in titanium alloys started after the second world war when titanium was widely used in the aerospace sector thanks to their excellent specific strength which is maintained even at high temperatures. Subsequently, titanium alloys were used for multiple applications in the civil engineering, marine and chemical fields due to their high corrosion resistance in numerous aggressive environments.

The good corrosion behavior is due to the high reactivity of titanium with oxygen which leads to the formation of TiO_2, a very stable and protective oxide. Moreover, this oxide is considered biocompatible, so titanium alloys are also used for biomedical implants [69,70].

Pure titanium has two equilibrium structures that depend on temperature and alloying elements. α phase is hexagonal close-packed crystal structure in equilibrium at room temperature. At 882.5°C there is an allotropic transformation which gives to the material a body-centred cubic structure (β phase) [71].

For alloys, the phase transition temperature varies strongly with the interstitial and substitutional elements as shown in Figure 1. In fact, the alloying elements of titanium can be distinguished in α stabilizers, β stabilizers and neutrals [69].

The most common α stabilizers are Al and the interstitial elements O, N and C. These alloying elements extend the field of the α phase by raising the α+β transition line. Aluminum is the most used element for this purpose because it has a large solubility in α and β phases.

β stabilizers can be classified into two categories: those forms binary systems of the β isomorphous type and those that promote the formation of a β eutectoid. The most used alloying elements that stabilize β isomorphous are V, Mo and Nb. Sufficient alloying of these elements can make the β-phase stable at room temperature. The most common elements in titanium alloys that favour the formation of β eutectic are Cr, Fe and Si.

Alloying elements with negligible influence on T_β are considered neutral. They increase the strength of α phase by solid solution. The most common are Sn and Zr [71,72].

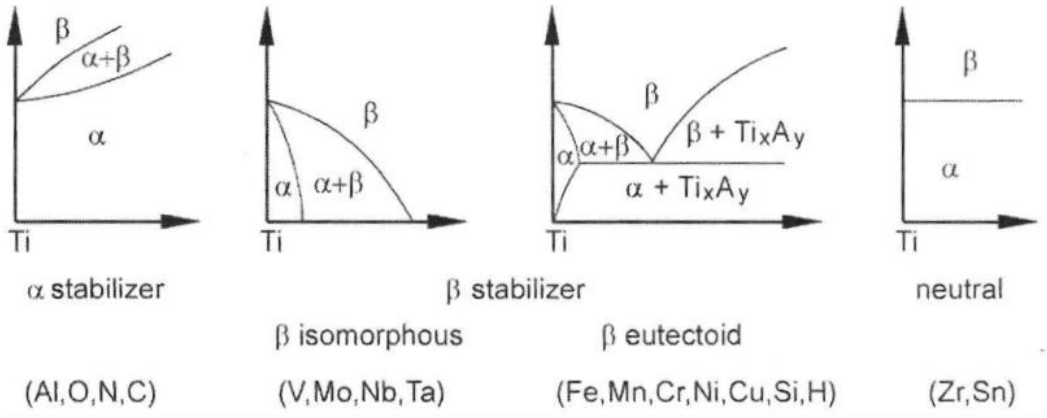

Figure 6 - Effect of alloying elements on phase diagram of titanium alloys [69]

2.2.2 Titanium alloy classification

Titanium alloys are classified conventionally in three main categories according to their position in pseudo-binary β isomorphous diagram shown in Figure 7.

The first class is named α alloys and it comprises commercially pure titanium and alloys with less than 2 wt.% of β stabilizer [72]. Alloys that are entirely single phase α have exclusively α stabilizing or neutral elements, they don't show response to heat treatments and they have outstanding creep resistance and corrosion behavior. The near α alloys are obtained with addition of β stabilizer up to 2 wt.%. These alloys are characterized by 10 vol.% maximum of β and high creep resistance with good strength levels [71,72].

Increasing the amount of β stabilizer there are α+β alloys, they support a mixture of α and β phases. These alloys contain between 10 and 50% of β phase at room temperature. They are characterized by good fabricability and high strength at room temperature. The properties of α+β alloys can be controlled by heat treatment by adjusting the microstructural and precipitational states of the β component [70]. After fast cooling from the β phase field, a martensitic transformation occurs which causes an increase in tensile strength, although creep resistance is reduced.

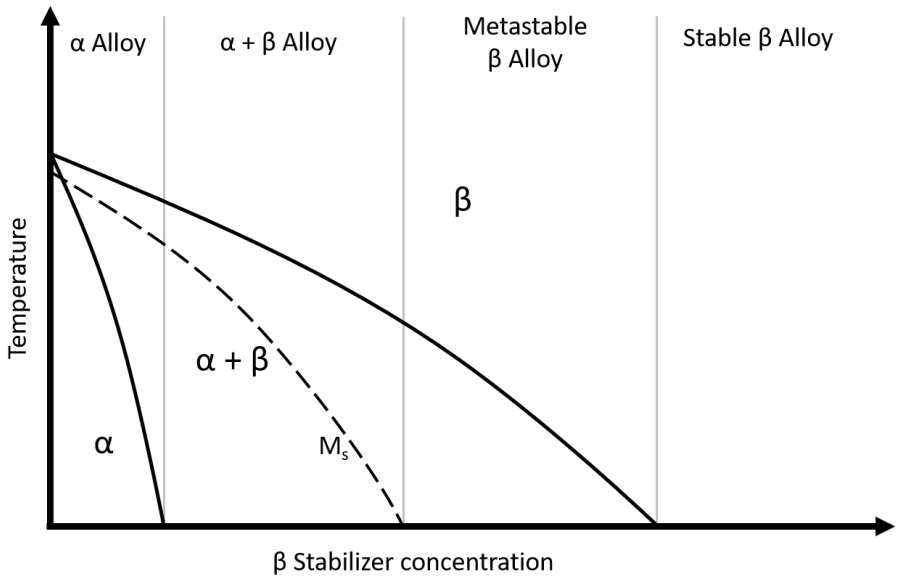

Figure 7 - Pseudo-binary section through a β isomorphous phase diagram [69]

The last group is named β alloys and it is composed of metastable β alloys characterized by the α+β field at the room temperature. Conversely, Stable β alloys are located where there is β single phase field at room temperature, but they do not exist as commercial materials so the expression β alloys usually refers to the metastable β alloys. β alloys do not transform martensitically upon quenching from β phase field, however metastable β alloys precipitate a second phase upon aging while stable β alloys should not be able to be hardened by heat treatments [71].

2.2.3 Alloys for reducing acid environments

The excellent resistance of titanium to corrosion in most environments is well-known. The presence of a thin oxide film on the surface exposed to environment promote the passivation titanium as long as the integrity of the film is maintained. This oxide film is very stable and self-healing in several environments. Titanium shows outstanding resistance in most oxidizing solutions at any pH value, for example in salt solutions, including chlorides, hypochlorites, sulfates, and sulfites, or in nitric and chromic acid solutions [69,71,73].

Nevertheless, the protective nature of the oxide film is no more present in a reducing environment. In these conditions the titanium oxide film becomes unstable and cannot be repaired, especially at low pH values as shown in Figure 8 [71], [74].

The addition of alloying elements to titanium can improve the corrosion resistance. Commercially pure titanium and α alloys exhibit an enhanced corrosion behavior in reducing acidic solutions with the addition of a small amount of metals of the platinum group (PGMs). In the commercialized alloys,

the additions are limited to Pd and Ru. [69,73,75] PGMs facilitates cathodic depolarization by providing sites of low hydrogen overvoltage on alloy surfaces and by shifting alloy potential in the positive direction [76].

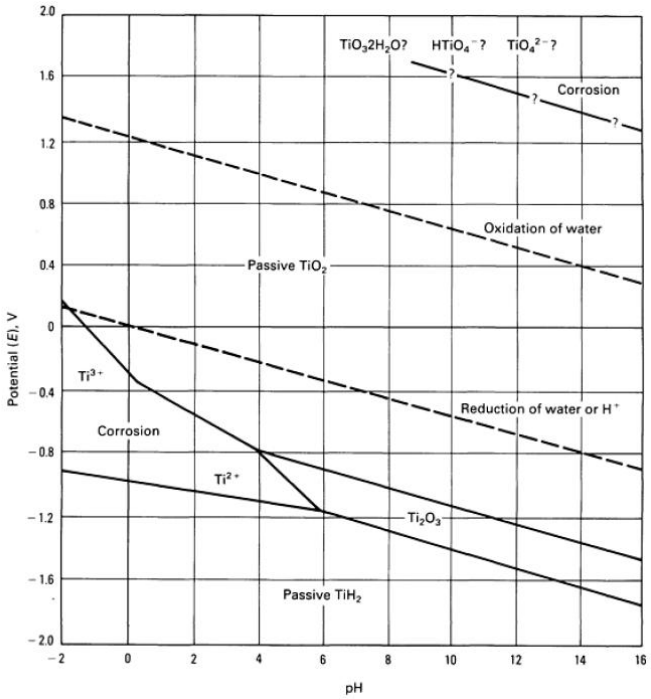

Figure 8 - Pourbaix diagram for the titanium-water system at 25°C [76]

The first developed titanium alloys with a small quantity of Pd were Grade 7 (UNS 52400) and 11 (UNS 52250) with 0.2% Pd. Such an alloys are used in chemically industries for HCl, HBr, H_2SO_4, H_3P0_4, inorganic acids, and acetic, formic, and citric organic acids or for storing media that fluctuate between oxidizing and reducing condition.[69] They have the most corrosion resistance among the titanium alloys commercially available, but the cost of these alloys are twice than unalloyed titanium [75].

Further studies demonstrated that even decreasing the nominal palladium content from 0.2% to 0.05% maintains significant effect on the corrosion behavior in reducing environments. [69,75]

These alloys with lower Pd content cost 30% less than Grade 7 and they have been successfully applied in all conditions except for the most aggressive reducing acid environments.

In order, to reduce the excessive cost, Ti alloys containing 0.1% Ru were developed with a behavior comparable to Ti alloys with 0.05% Pd and a reduction of 20% of the costs [69].

As well the resistance of α+β alloys and β alloys to hot reducing acids could be improved by the addition of PGMs. In fact, the strength of α alloys is not suitable for all engineering applications. For this aim, α+β and β alloys have been developed with a small amount of PGMs. The most studied

alloys with this intention are Grade 5 (UNS 56400), 9 (UNS 56320) and 19 (UNS 58640) which have given rise to some Pd and Ru enhanced alloys visible in the Figure 9 [77–79]. Moreover, it has been shown that other alloys, both α+β and β, also improve their corrosion behavior by adding Pd [70,80].

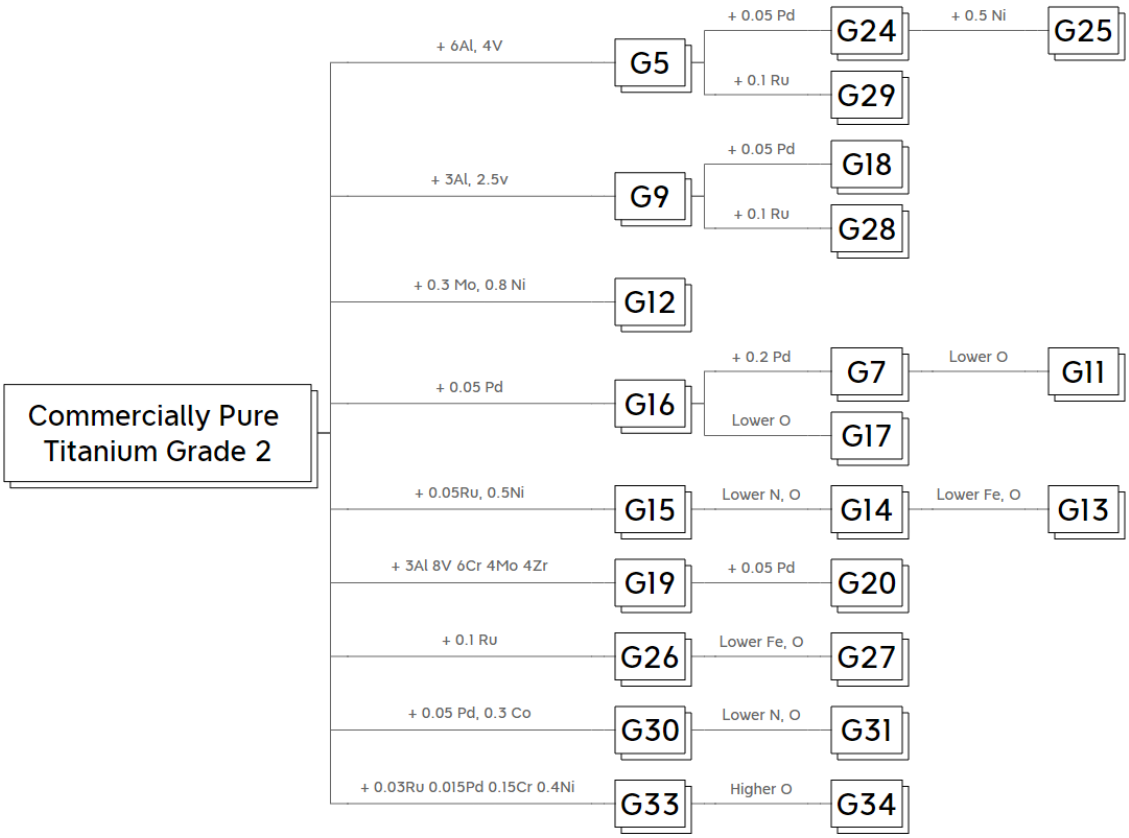

Figure 9 - Classification of titanium alloys for reducing environments from ASTM B 348

Although they do not have an efficiency comparable to PGMs additions, other alloying elements can improve corrosion behavior in reducing acid environments. Contents of molybdenum and zirconium more than 3% and 8% respectively are exceptionally beneficial, whereas vanadium having minor importance [69].

Even an addition of nickel improves the resistance of titanium in acid reducing environments, in fact the Grade 12 with 0.3% Mo and 0.8% Ni is widely used. Grade 12 is an α alloys with a better strength and corrosion resistance. However, the corrosion resistance of this alloy is not as good as the Pd and Ru enhanced titanium alloys [69,73,74,81]. It has been discovered that a percentage of cobalt in titanium alloys improves the corrosion behavior in boiling reducing acid and in boiling chloride solutions [70,82].

The other main alloying elements have adverse effect on corrosion resistance of titanium alloys in reducing acidic environments, especially increasing aluminum levels exceeding 3% [69,73].

Alloys belonging to α+β group typically have corrosion behavior worse than unalloyed titanium. An exception is Ti-6Al-2Sn-4Zr-6Mo (UNS R56260) that is used in deep, sour-well application and in harsh service environment in oil&gas sector. However, it is less resistant to oxidizing media than commercially pure titanium.

The β group covers several alloys characterized by a high amount of β stabilizers and alloying elements in the composition. Some of these alloys have large quantities of alloying elements which enhance the behavior of titanium in reducing acid environments.

Ti-11.5Mo-6Zr-4.5Sn (UNS R58030) and Ti-15Mo-3Al-2.7Nb-0.25Si (UNS R58210) have good corrosion behavior under reduction conditions thanks to the presence of molybdenum and zirconium. They find application in aerospace, chemical, biomedical and in oil&gas for offshore field. Another appropriate alloy in reducing media is Grade 19 (UNS R58640) that is used for tubulars and casings in oil&gas and geothermal wells. The alloy Grade 20 (UNS 58645) was also developed with the addition of 0.05 Pd to extend the fields of application [70,78].

Ti-15Mo-5Zr and Ti-15Mo-5Zr-3Al has an excellent behavior in reducing environment, especially they have a good resistance to atmosphere SCC. These alloys show corrosion resistance in reducing acid environments better than Ti-0.2Pd alloy. They are suitable for sour gas plants for high atmospheric SCC resistance and turbine blades for power plants and erosion shield. Ti-15Mo-5Zr-3Al possesses superior strength, ductility and toughness of Ti-15Mo-5Zr despite worse erosion resistance [70].

2.3 AM of titanium alloys

Nowadays, the powders commercialized for LPBF include commercially pure titanium (CP-Ti), Ti-6AL-4V, Ti-6Al-2Sn-4Zr-2Mo, Ti-5Al-5V-5Mo-3Cr and Ti-6Al-2Zr-1V-1Mo. However, most of the market is formed of powder suppliers who have available CP-Ti and Ti-6Al-4V powders.

CP-Ti obtained for LPBF has been widely studied and the optimization of the process parameters has solved many of the characteristic defects [83–86]. In contrast with traditionally manufactured CP-Ti which is characterized by the α phase, LPBF showed α' martensitic phase microstructure. The difference in the microstructures is related to process parameters including linear energy density and scan speed that affect solidification rate [83]. For cooling rate above 10^3K/s the martensitic phase is observed with lath-type morphology. LPBF can also reach higher solidification rate that defines finer lath-type martensite and fine acicular martensitic morphology at 10^6 K/s [85]. The CP-Ti manufactured by LPBF showed better mechanical behaviors than traditional one thanks to the fine microstructure and the martensitic phase [83,85,86].

2.3 - AM of titanium alloys

In the α+β group, Ti-6AL-4V is the most widespread titanium alloy and is the one most studied and utilized for AM technologies. Ti-6AL-4V is usually composed by α-phase and a small amount of β-phase. The microstructure is defined by the solidification rate that changes with production technology and heat treatment. Wrought and cast components are characterized by slow to intermediate cooling rates that create α-lamellae to form α-Widmanstätten laths or Equi-axed grains of α and transformed β [71,87]. By increasing the cooling rate, the length and thickness of the -lamellae decrease, which increases the mechanical strength. Furthermore, when the cooling rate exceeds 410 K/s, the β phase transforms to the martensitic α′ phase. This transformation increases the strength and hardness of this alloy, although reducing ductility. Ti-6AL-4V produced by LPBF usually has a microstructure where most of β-phase has been transformed into α' martensite [87]. However, Kazantseva et Al. discovered that a $\beta \rightarrow \alpha''$ martensitic transformation can take place. According to their findings, this transformation can occur in previously manufactured layers where the material is subjected to an in-situ heating and cooling cycles [88]. In general, Ti-6AL-4V fabricated by LPBF is not used in as-print condition. The ductility is considerably lower than the same material produced by traditional technologies due to the non-equilibrium α' martensitic microstructure and high residual stress. The most common solution is a heat treatment, mainly stress relieving [89].

The commercialized titanium powders for AM are not suitable for reducing acid environments, however other titanium alloys have already been produced by LPBF or are under development. The main reasons are the academic research and the industrial advancement regarding the feasibility of titanium alloys by means of LPBF. A portion of these titanium alloys can be used for applications in reducing acidic media. In the following studies, the feedstock used have been produced specifically to research and characterize new powders for AM. Indeed, the powders of the following publications are not available on the market but were obtained by atomization of pre-alloyed ingots or by mechanical mixing of powders [86,90].

The Ti-6Al-2Sn-4Zr-6Mo alloy is the most studied. Carrozza et al. investigated different values of laser power, scanning speed and hatching distance and discovered that Volumetric Energy Density (VED) higher than 40 J/mm^3 provide density values markedly greater than 99%. Moreover, the alloy had a different type of martensite, which is orthorhombic (α'') instead of hexagonal, the usual of the other $\alpha + \beta$ alloys. The samples showed markedly low yield strength and hardness values but extensive ductility [91]. In this regard, Carrozza et Al. customized heat treatments to assess the microstructures and the mechanical properties. Annealing temperatures were determined based on the results of DSC thermograph with the aim of characterize the phase transformations. The first result indicates that annealing at 600°C for two hours completely transforms α'' phases toward α + β

microstructure. As a result, there is a significant increase in strength but also a severe decrease in ε. For annealing at higher temperatures, stress relaxation occurred and caused an improvement in ductility despite a reduction in strength [92]. Peng et al. demonstrated the presence of an orthorhombic martensite phase in the as-built specimens too. They optimized heat treatments to transform α'' phase and harden the material. According to the results, the highest peak of hardness is reached heating at 650 °C for 5 minutes, corresponding to the α″ phase decomposition into the α and β phases [93]. Hassanin et al. evaluated the hardness and the porosity of Ti-6Al-2Sn-4Zr-6Mo as a function of the LPBF process parameters. The minimum porosity results at 77 J/mm^3, while the hardness using 158 J/mm^3 of VED. Furthermore, hot isostatic pressing was able to eliminate the porosity and decompose the undesirable α'' martensitic phase into the α and β phases [94].

Mizuno et al. studied Ti-15Mo-5Zr-3Al fabricated via LPBF. They made a characterization of relative density and surface morphology depending on the VED and scanning speed. The result shows that the surface morphology of the specimens tends to change from a porous shape to a flat and swelling shape as the output energy density increases. Differently, the relationship between VED, scanning speed and relative density is more complex. Low values of scanning speed and VED are always inadequate, however too high values of VED can increase the porosity because the gas is entrapped during the collapse of the keyhole-type melt pools. According to the inductively coupled plasma analysis, the concentration of Mo increased during the gas-atomization and LPBF processes due to the evaporation of Ti and Al. Finally, these studies characterized phase stability, tensile residual stresses, tensile properties and crystallographic texture [95–99].

A Ti-15Mo-2.7Nb-3Al-0.2Si specimens were manufactured via LPBF by Macias-Sifuentes et al. achieving an average relative density of 99.9% using Ti–6Al–4 V (wt%) standard set of parameters provided by Renishaw. The as-built alloy was primarily composed of β-phase, with columnar grains oriented along the build direction and had mechanical properties comparable to Ti-15Mo-2.7Nb-3Al-0.2Si fabricated by traditional technologies. The same conclusion was made for the heat treatment: solution treatment and aging of the alloy precipitated the α-phase and outlined similar effect compared to the same alloy produced by non-AM techniques [100]. Pellizzari et al. produced the same alloy by means of LPBF and characterized the properties of different heat treatments. A fully metastable β structure had been obtained in as-built condition. The precipitation of the ω phase occurs with the aging at 350°C for 2h, with minor changes in strength and a slight reduction in ductility. Conversely, aging at 650°C for 2h promotes a strong precipitation strengthening by α phase and a marked decrease in fracture elongation. Finally, the heat treatment at 590 °C for 8 h causes a fine precipitation of intragranular α increasing strength and elastic modulus with no change in fracture elongation. Furthermore, they assessed the material for biomedical applications evaluating the cytotoxicity and

mechanical behavior with compression tests, cyclic compression tests on bulk materials and functionally graded porous structures [101–105].

Madikizela et al. manufactured Grade 19 obtaining samples with densities higher than 98%. The microstructure of the Ti-3Al-8V-6Cr-4Zr-4Mo alloy consisted of columnar epitaxial β grains. The lack of α' martensitic phase ensured higher ductility and fracture toughness compared to the Ti-6Al-4V despite the ultimate tensile strength [106].

Qiu et al. processed palladium modified Ti–6Al–4 V by LPBF at a constant laser power of 400 W but with different laser scanning speeds ranging from 1300 mm/s to 4300 mm/s. The specimens show optimal porosity except for scanning speeds over 3000 mm/s. Pd was completely dissolved into the matrix of Ti64 after LPBF. Moreover, a comparison of the mechanical and corrosion behavior was made between this alloy and a free Pd Ti–6Al–4 V. The results show how the addition of Pd improves corrosion behavior without affecting the mechanical characteristics even for test pieces produced for LPBF [107].

2.4 Powder metallurgy for AM

In addition to the manufacturing process parameters, the properties of the metal powder are crucial to obtaining printed parts of good quality. Over the past decade, it has been one of the most studied topics about AM of metals. There are standards, both ISO and ASTM, that define how to characterize AM powders [108,109]. Powder characterization is commonly used in publications where samples are produced using AM. The system that defines how the properties of the powder can affect the properties of the part is very complex and has still not fully understood. Powder characteristics can be divided into the properties of individual particles and the behaviors of the powder considered as a whole. The powder characteristics are defined by the manufacturing process and influence the property of the final material. The bulk powder properties are crucial to have both a homogeneous spreading and a good packing of powders. In this field, flowability is a very studied characteristic and there are many techniques to quantify it [110,111].

The level of complexity is further increased by evaluating the process parameters related to the powder. They are called in-process performances and describe the behavior of the powder during all the steps of the manufacturing process. Figure 10 describes the relationship between the powder characteristics and the properties of the part [112–115].

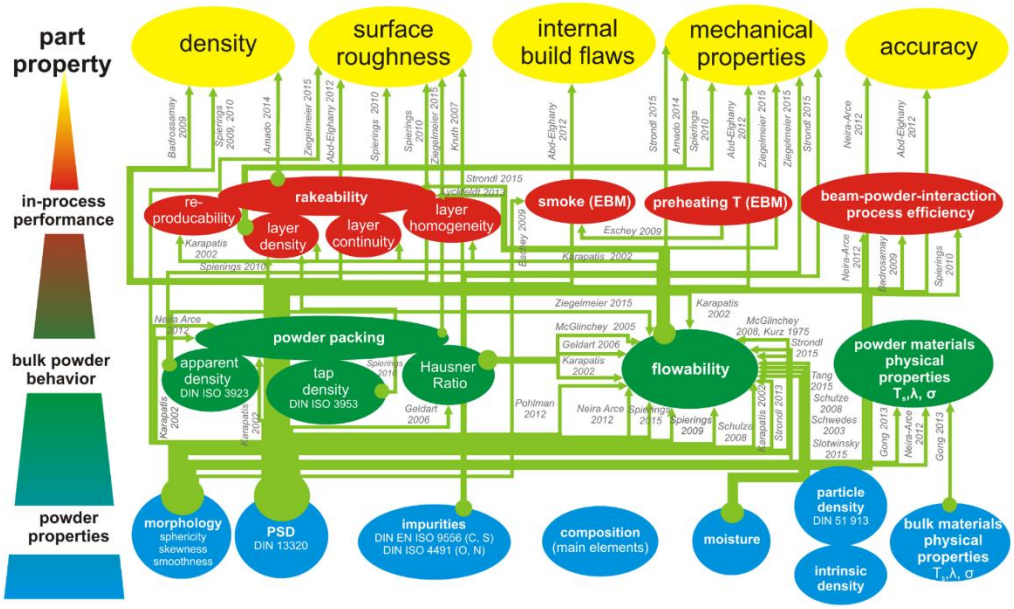

Figure 10 - Relationships between powder properties, bulk powder behavior, powder performance in process and the manufactured part quality *[112]*

In practice the most important characteristics are composition, particle size distribution, morphology and flowability. In accordance with the literature, the difference composition between metal powder and part is a typical occurrence. The reason is that powders are not completely pure or change over time due to stocking methods and repeated exposures in an AM build chamber environment [114]. Powders can take moisture or contaminate and lead to an increase in interstitial elements in the part. This can compromise the mechanical and corrosion properties of the material; a common example oxygen is titanium. Moreover, the manufacturing process can lead to a slight variation in the final composition. A case already studied in literature has been the undesired vaporization of alloying elements such as Mg and Zn during the production of aluminum alloys by means of AM [116,117].

Particle morphology affects the bulk packing and flow properties of a powder batch. The influence of this property is complex and cannot be answered by simple relationships. However, it is known that powders with spherical and smooth shapes have better flowability and packing density than rough and sharp-edged particles [112,118].

The particle size distribution is another important powder property. It defines the minimum layer thickness and the resolution of the finest detail in the component. Furthermore, it influences the packing density [115,118].

Powder metallurgy is a sector that developed before AM. In fact, some technologies for powder production such as the water jet and hydrogenation–dehydrogenation process produce powders that do not match the characteristics suitable for AM technologies. The previous technologies can be used for AM if the powder is post-processed before printing [118–120]. A metal powder production

technology is considered appropriate for AM if it produce powder with a smooth or spherical morphology and a small particle size. The most common technologies to obtain AM powders have a particle size that reaches up to 500 μm while the LPBF and Electron Beam Melting (EBM) technologies work with powders whose particle size varies respectively from 15 to 45 μm and from 45 to 105 μm [112,118]. Particle size and particle size distribution are always optimized with sieving or air classification methods [121].

Atomization is the most common technology for powder production in AM. It consists of two steps: shearing of liquid metals and freezing the liquid droplets. It can be gas or plasma atomization depending on the fluid used during the process.

Gas Atomization uses high-pressure streams of air, steam, or an inert gas to atomize the molten metal. The ingots are melted in a crucible then the molten metal flow through a nozzle. The solidification time is long enough to ensure a spherical shape to the particles. Plasma atomization has metal wire as a feedstock that is melted and atomized by plasma torches. The material reaches a higher temperature than gas atomization, this allows the production of highly spherical particles [118,122,123].

Another technology that produces spherical and highly pure particles is the plasma rotating electrode process. In this technology, the bar surface is melted by a high temperature plasma. The molten droplets are ejected from the surface by the interaction of the rotation and the gas jet. [122] The powder obtained has minimal or no gas pores because the metal droplets are produced by centrifugal forces, not high-pressure gas [124]. However, this technology is much less common as it has a low productivity and high cost [125].

Centrifugal atomization is a well-established but not widespread technology. The molten metal in free fall is sheared by a high-speed rotary disc in a tangential direction. This technology allows the average particle size to be controlled by the rotation speed. This has led to an increase in the rotation speed so that the particles are finer and finer [121,122].

Plasma spheroidization is a technology that is highly interesting for the AM sector, as it allows to obtain powders with highly spherical morphologies starting from powder with irregular geometries with sharp edges. A gas carries the powder particles into the central confinement tube where there are electromagnetic fields generated by induction coils. Here, the gas turns into plasma with high temperatures around 3,000–10,000 K. The plasma partially or fully melts the particles, the surface tensions reshape the particles into spheres and then solidify at high cooling rates while falling under gravity [126].

Titanium is not suitable for all powder production technologies. The main reason is that molten titanium is very reactive to most common metals and ceramics. The use of ceramic crucibles to

contain molten titanium results in contamination of the powder produced and wear of the crucible [122,124]. The problem is not present in PA and PREP because the feedstock is not molten metal. In particular, the PA was intentionally developed to produce titanium powder [124]. This difficulty is present in GA, the leading technology for producing metal powders. To overcome this issue, Electrode Induction Gas Atomization (EIGA) and Plasma Inert Gas Atomisation (PIGA) technologies have been developed. These processes offer a superior quality of inert gas atomization. The difference with the traditional GA lies in the heat source for melting, following the molten metal is atomized by an inert gas flow at high pressure as in the usual technique. The EIGA process uses inductive coils, whereas the PIGA process uses a plasma gun [121,122,124].

2.5 Standard and qualification of metal obtained by means of AM

In the current market, AM powders are available for a limited number of Ti alloys, although the qualification of new powders is constantly increasing [86].

The main reasons are that the AM industry is recent and still takes a lot of work before achieving a complete consolidation. AM technologies have different metallurgies than traditional ones [127]. Therefore, a complete standardization of AM processes and materials is necessary to guarantee the adoption of AM parts in industrial applications. ISO and ASTM are the leading developers of voluntary international standards about AM since 2011. The main topics of the standards published are terminology, characterization of feedstock and AM materials, test methods of AM parts, qualification principles and design guidelines. The technology that has the most standards is LPBF, while the materials are nickel and titanium alloys [128]. These standards assess the performance of AM products for assuring their quality, however they do not cover all aspects about the characterization and the qualification of the AM parts. A neglected topic in standards until a few years ago is the corrosion assessment. It is a common knowledge that materials fabricated by AM can have a different corrosion behavior compared to traditional ones [129]. ISO/TC 156 published standards for testing localized corrosion and environmentally assisted cracking of additively manufactured metals and alloys. The standards were published because AM produce parts with distinctive properties and defects that can impinge on corrosion behavior and conventional testing methods have shown limited ability for evaluation of those factors [130–132]. There are government institutes and commercial companies that have developed metal AM standards in collaboration with ASTM and ISO. Requirements, specifications, testing standards, material data sheets and qualifications were the main topic of these standards. Some of these companies are developing guidelines for the qualification and certification of AM parts for certain industrial sectors [128,133,134].

2.5 - Standard and qualification of metal obtained by means of AM

A technical committee was established by the Society of Automotive Engineers (SAE) to develop and maintain aerospace specifications for the use of AM parts.

The National Aeronautics and Space Administration (NASA) published a standard (MSFC-STD-3716) and a further specification (MSFC-SPEC-3717) for evaluating AM parts during their development and production for spaceflight applications. The American Petroleum Institute (API) published 20S Standard for the AM qualification process. The goal was to develop a system for evaluating AM metal parts for oil and gas sector [128]. The Association for Materials Protection and Performance (AMPP) is also investigating the use of AM in oil and gas applications. They are creating a technical report that presents the current state of knowledge and gap analysis on corrosion testing of metallic materials fabricated by AM [135]. For the marine and offshore industries, Det Norske Veritas (DNV) published the class guideline DNV-CG-0197 which provides a framework for approval and certification of materials, products and components fabricated by means of AM through a systematic qualification approach [128,134].

Chapther 3. Case study I: geothermal turbine blades made of nickel-based alloys

3.1 Chapter introduction

As discussed in Chapter 1.2, when the geothermal steam expands and approaches the DwP, highly aggressive operating conditions are developed due to the formation of acidic and chloride-rich condensates. Over the years, several mitigation strategies have been proposed to limit corrosion-related damage in geothermal turbines. Process-based approaches, such as steam washing with alkaline solutions, can reduce the aggressiveness of the condensates but ead to a decrease in plant efficiency [136]. Consequently, the adoption of CRAs represents a more energy-efficient and, ultimately, economically viable solution for geothermal applications [25].

In this context, the present chapter reports a case studies of turbine blades manufactured from two nickel-based superalloys, Alloy 718 and Alloy 725, retrieved from a direct-cycle geothermal power plant operating under DwP conditions with no steam washing.

The aim of this chapter is to identify the degradation mechanisms developed during service and to assess the suitability of these alloys for application in aggressive geothermal environments. Alloy 718 is a widely adopted superalloy for high-temperature turbine components and is currently available for production through advanced AM routes. Alloy 725, on the other hand, has been specifically designed to enhance corrosion resistance in aggressive environments, owing to its higher chromium and molybdenum content combined with excellent mechanical properties [137]. Particular attention is devoted to the identification of corrosion and cracking mechanisms, providing the basis for subsequent material selection strategies and for the development of alternative manufacturing and material recovery approaches discussed in the following chapters.

3.2 Materials and methods

3.2.1 Materials

The material investigated consists of two turbine blades that had 4 years of service in a geothermal plant based in Larderello and provided from Enel Green Power S.P.A. (EGP). The samples were taken from the most critical stages of the turbine, corresponding to sections where the expanding fluid reaches dew-point conditions. The service conditions were estimated in previously study and consists

in a superheated steam at a temperature of 150°C at pH 3.5 with 7 000 ppm of chlorides and 60 000 - 80 000 ppm of boric acid [25].

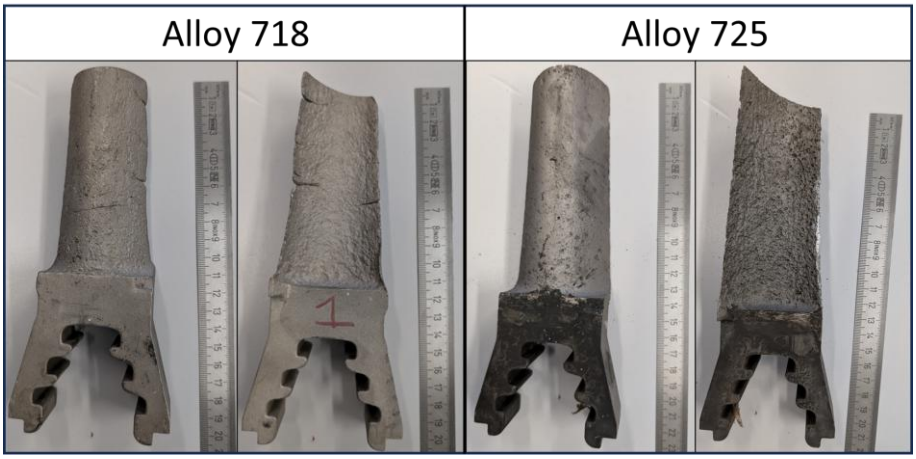

Figure 11 - Images of ex-service turbine blades

The turbine blades are made two different nickel super alloy, known as Alloy 718 (UNS N07718) and Alloy 725 (UNS N07725), composition visible in Table 1. Both components were in the aged condition, with hardness values of 41 HRC for Alloy 718 and 37 HRC for Alloy 725.

Table 1 - Composition of Alloy 718 and 725 following ASTM standards

Alloy	Type	PREN	Ni	Cr	Fe	Nb+Ta	Mo	Ti	Al
718	ASTM B637	26.2-29.9	50.0-55.0	17.0-19.0	Bal.	4.75-5.50	2.80-3.30	0.65-1.15	0.20-0.80
	EDS analysis	28.8	52.63	18.98	18.35	5.64	2.97	1	0.43
725	ASTM B805	42.1-53.85	55.0-59.0	19.0-22.5	Bal.	2.75-4	7.00-9.50	1.00-1.70	≤0.35
	EDS analysis	50.7	56.65	21.24	7.23	3.99	8.93	1.52	0.3

3.2.2 Microstructural analysis

Keyence VHX-7100 digital optical microscope (OM) was used to document the condition of the turbine blades after the service and for metallographic purpose. A Zeiss Gemini Sigma 300 field emission scanning electron microscope (FESEM), equipped with an Oxford x-act probe for energy-dispersive X-ray spectroscopy (EDS), was employed to analyze the fracture characteristic and identify second phase and corrosion product through EDS analysis. To remove corrosion products,

the samples were pickled in diluted hydrochloric acid with hexamethylenetetramine as an inhibitor before the fractographic analysis. Mixed acid reagent (15 mL HCl, 10 mL HNO_3, 10 mL CH_3COOH) was used to reveal the microstructure. X-ray diffraction (XRD) analyses were carried out using a Malvern PANalytical diffractometer equipped with Cu K_α radiation, operating in Bragg-Brentano geometry. Diffraction patterns were collected in the 2θ range 30–100°, with a step size of 0.013° and a counting time of 35 s per step.

3.2.3 Corrosion tests

Corrosion tests have been assessed following standard ASTM G 28 method to evaluate the susceptibility of intergranular corrosion. Before these tests, the specimens were mechanically ground with SiC emery papers up to 4000 grit and then polished with 1 µm diamond suspension. To highlight the microstructure before OM and FESEM analyses, the samples were also chemically etched with Kroll's reagent for approximately 5 seconds. The specimens were measured with a Vernier caliper with 0.05 mm resolution and weighted with an analytical balance of 0.00001 g sensitivity before and after each test, to measure the weight loss and calculate the average corrosion rates. The cross section of tested specimens was analyzed with FESEM to evaluate the morphology of corrosion. Alloy 725 in forged condition has been considered as a reference material.

3.3 Results and discussion

3.3.1 Condition of blades after operation

The turbine blades experienced erosion-corrosion during the service, exhibiting craters on the surfaces (Figure 12). This surface morphology is a characteristic indicator of erosion–corrosion processes and suggests that the blades operated under conditions close to the DwP. In addition to erosion–corrosion phenomenon, turbine blade made in Alloy 718 exhibits a breaking pattern characterized by long transverse cracks, mainly located at the leading and trailing edges as well as on the suction side (Figure 12 D-E).

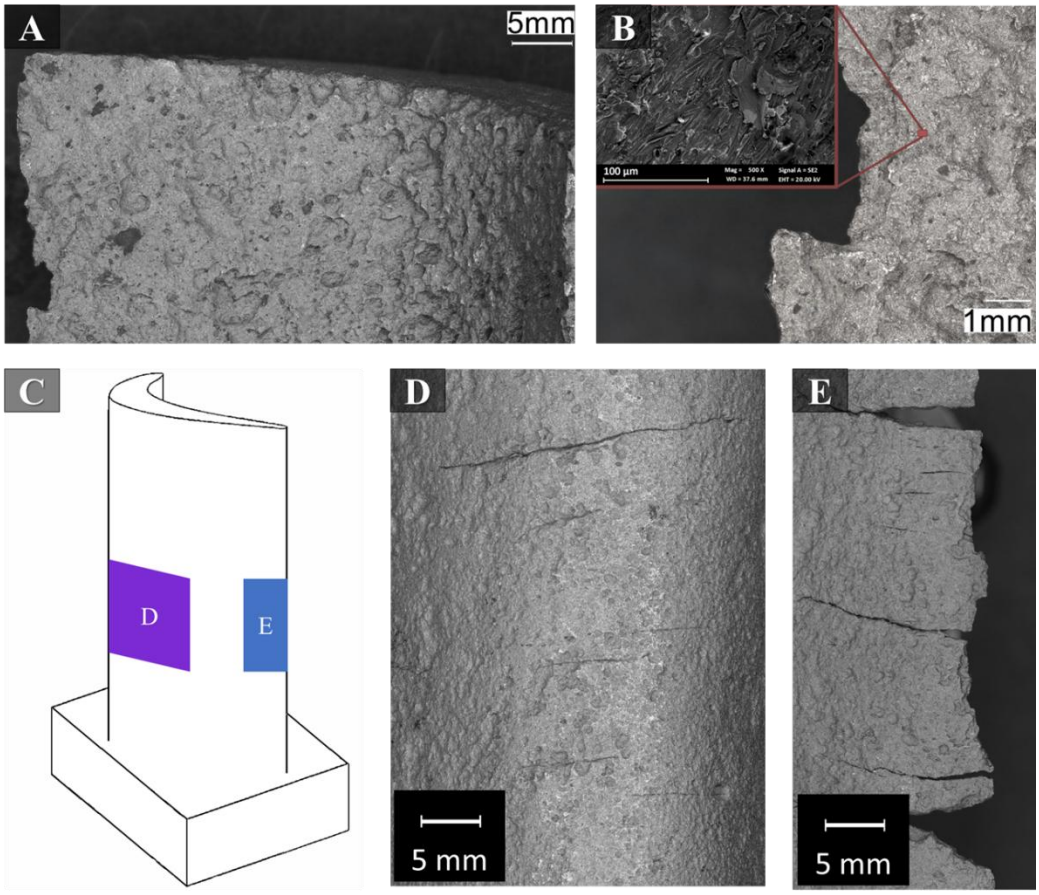

Figure 12 - Details of degradation in turbine blades. A, B) craters of corrosion-erosion of component made in Alloy 725 and C, D, E) craters of corrosion-erosion and cracks of SCC of component made in Alloy 718

No cracks were observed in any region of the blade made of Alloy 725, indicating the full resistance of this material. Cross section of turbine blade made with Alloy 718 highlighted cracks with branching and a predominantly intergranular propagation (Figure 13A). The fracture surfaces of cracks were covered of corrosion products containing chlorine and sulfur (Figure 13B). After the chemical cleaning, the surface showed an intergranular propagation. All these characteristics are typical of chloride SCC [138].

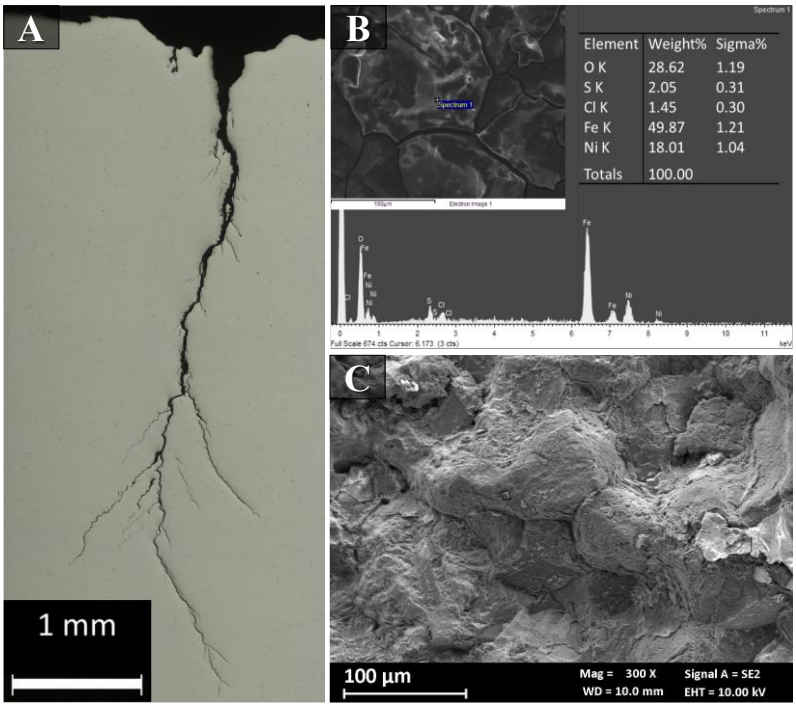

Figure 13 – A) Cross-sectional FESEM micrograph showing a crack in an Alloy 718 turbine blade; B) EDS analysis of corrosion products inside the crack; C) FESEM fracture surface of cracks in the Alloy 718 turbine blade.

On the pressure side, no cracks were detected also in Alloy 718 however the cross-sectional analysis revealed an additional degradation mechanism, as visible in Figure 14. In fact, Alloy 718 turbine blade exhibited localized corrosion attacks unlike the Alloy 725 component. Despite this difference, both alloys showed evidence of surface degradation attributable to erosion-corrosion.

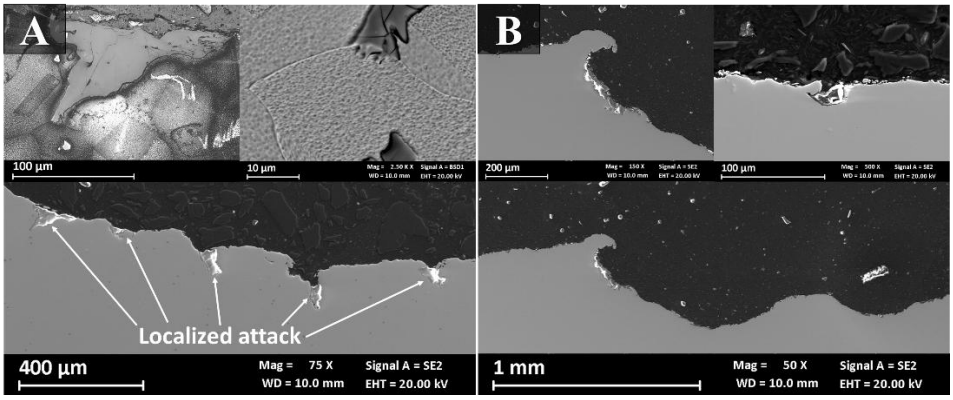

Figure 14 - Cross-sectional micrograph of the pressure side of the components made with alloy A) 718 and B) 725.

3.3.2 Mechanism and cause of material degradation

The first degradation mechanism is associated with the impingement of a two-phase geothermal fluid on the blade surfaces. In direct-cycle geothermal power plants, these condensates typically contain aggressive chemical species, such as acidic chlorides, which enhance the material degradation through electrochemical processes. As a result, this condition is intrinsic to the service environment and can simply be managed by adopting materials that are excellent for resistance to corrosion-erosion, including those already applied.

In contrast, other degradation phenomena detected on turbine blade in Alloy 718, such as localized corrosion and stress corrosion cracking, represent a failure mechanism that should be always avoided. Unlike erosion-corrosion, these processes are highly localized, difficult to control and can lead to unexpected rupture.

The susceptibility of nickel-based superalloys to localized corrosion and SCC in geothermal environments is strongly influenced by nickel content and the Pitting Resistance Equivalent Number (PREN). A previous study [25], carried out using a different geothermal fluid from the same geothermal field, had already investigated the resistance to SCC and localized corrosion of corrosion resistant alloys. Field exposure tests performed on specimens did not reveal SCC phenomenon in either Alloy 725 or Alloy 718; however, the latter exhibited localized corrosion phenomena as visible in **Figure 15**. Conversely, this case of failure analysis conducted directly on turbine blades revealed the presence of SCC as well as localized attacks in Alloy 718, demonstrating that this material is not suitable for this application, particularly when operating in geothermal fluids containing acidic chlorides.

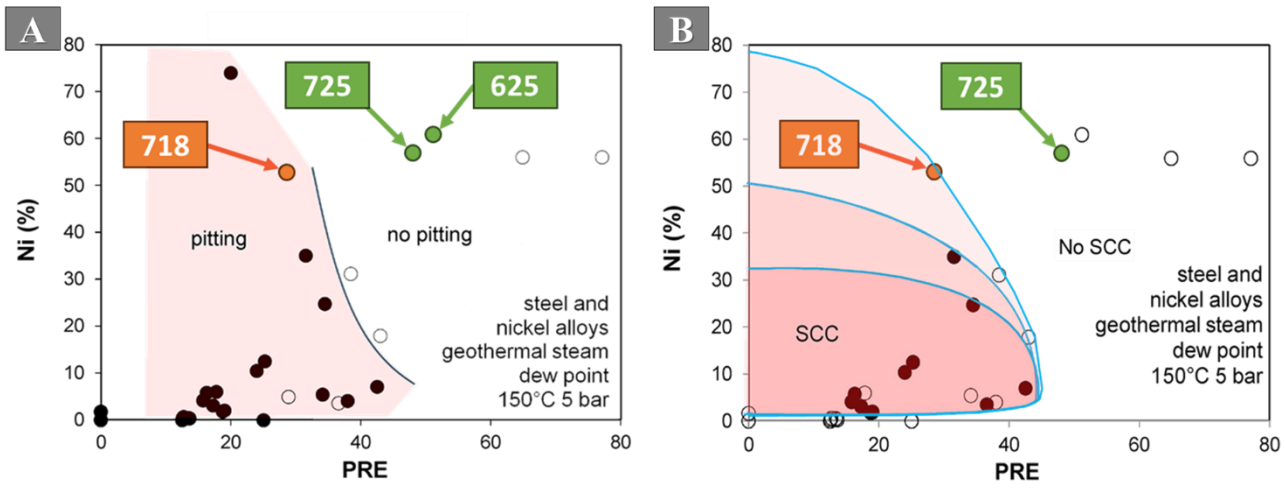

Figure 15 - Effect of nickel content and PREN value on A) pitting and B) SCC in geothermal fluid at 150 °C and 5 bar, figure adapted from Cabrini et Al. [25]

The mechanisms of pitting corrosion and SCC are governed by microstructure and secondary phases. In Alloy 718, extensive literature report that the δ phase plays a detrimental role in SCC resistance, acting as a preferential site for localized corrosion and intergranular crack. Wang et al. [139] demonstrated that the presence of δ phase at grain boundaries not only reduces the material's toughness, but also acts as a preferential site for the initiation of pitting as well as for the formation and growth of intergranular SCC cracks. Yazdanpanah et al. [140] investigated for the first time the initiation of SCC in Alloy 718 produced via L-PBF. Their results showed that the additively manufactured alloy exhibits increased resistance to SCC due to the absence of δ phase; however, crack formation still occurs via localized dissolution of the matrix in the regions adjacent to subgrain boundaries, promoted by local galvanic coupling. Ning et al. showed that, in the presence of δ phase, SCC initiation is anticipated and the crack propagation is predominantly intergranular. Similarly, Zhu et al. reported the same findings and discovered that crack growth is strongly promoted along the δ/matrix interface, where the formation of non-protective Nb_2O_5 lead to interfacial decohesion and intergranular crack propagation. In contrast, Alloy 725, for the aging temperatures relevant to the turbine blades considered in this study, tends to form different types of precipitates at grain boundaries [141,142]. The lower niobium content of Alloy 725 reduces the tendency for δ and Laves phase formation instead favoring the formation of $M_{23}C$ and M_6C carbides [142]. To the authors' knowledge, no studies have reported a detrimental effect of these precipitates on SCC resistance of Alloy 725.

The microstructure of both alloys consists of equiaxed austenitic grains with titanium- and nitrogen-rich precipitates (Figure 16), which are likely corresponding to titanium nitrides [143]. Alloy 725 presents secondary phase discontinuously distributed along the grain boundaries. Differently, Alloy 718 exhibits secondary phases at the grain boundaries but also globular Nb- and Mo-rich phases homogeneously dispersed throughout the matrix.

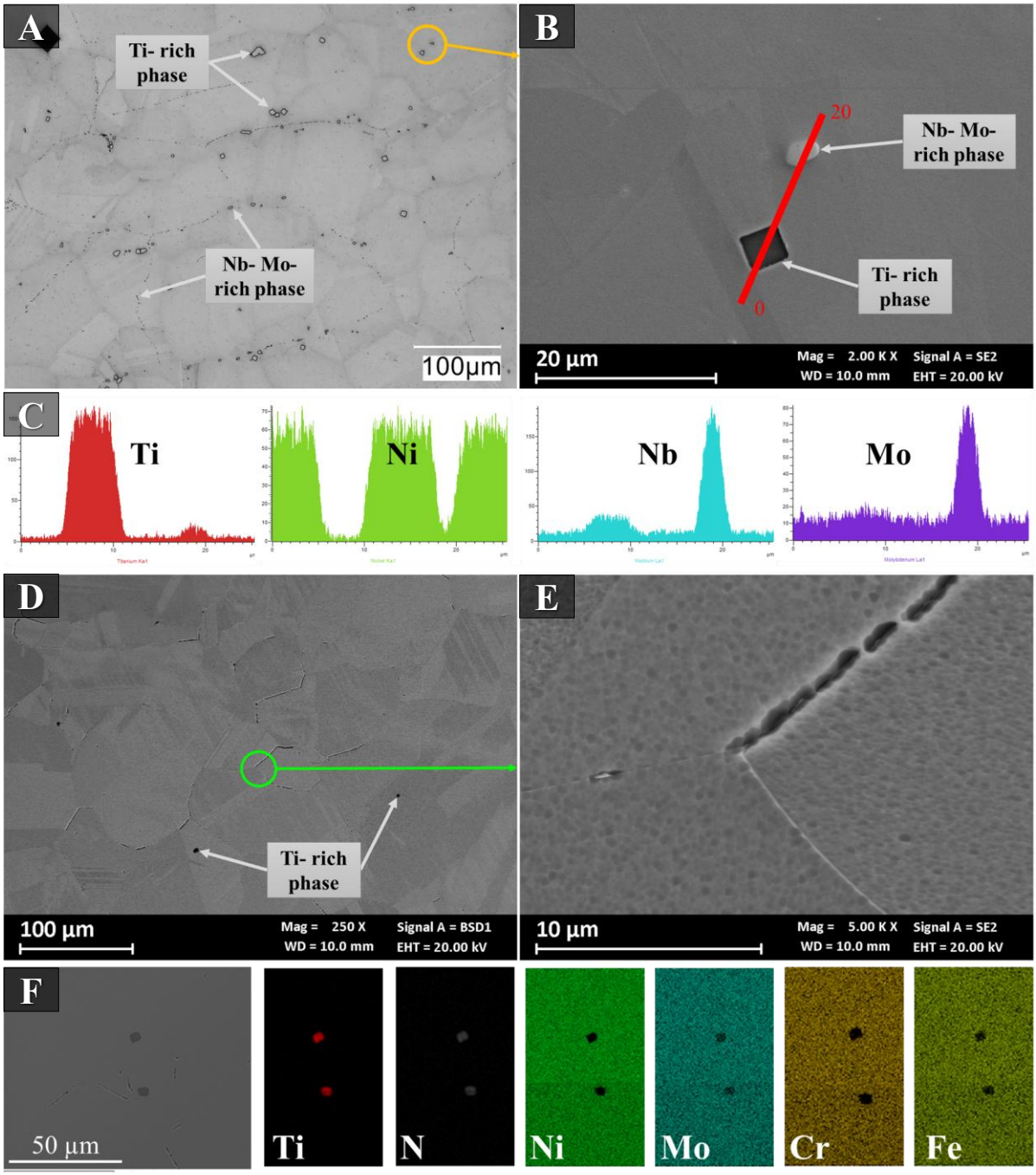

Figure 16 – A, B) Representative microstructures of Alloy 718; C) EDS line scan performed across precipitates in Alloy 718; D, E) Representative microstructures of Alloy 725; F) EDS elemental maps of precipitates in Alloy 725.

XRD analysis detected peaks attributable to the γ phase (fcc Ni-based matrix), as reported in Figure 17. It is reasonable to think that potential precipitates formed during precipitation hardening are too fine or homogeneously dispersed in the γ matrix to produce distinct and resolvable diffraction peaks.

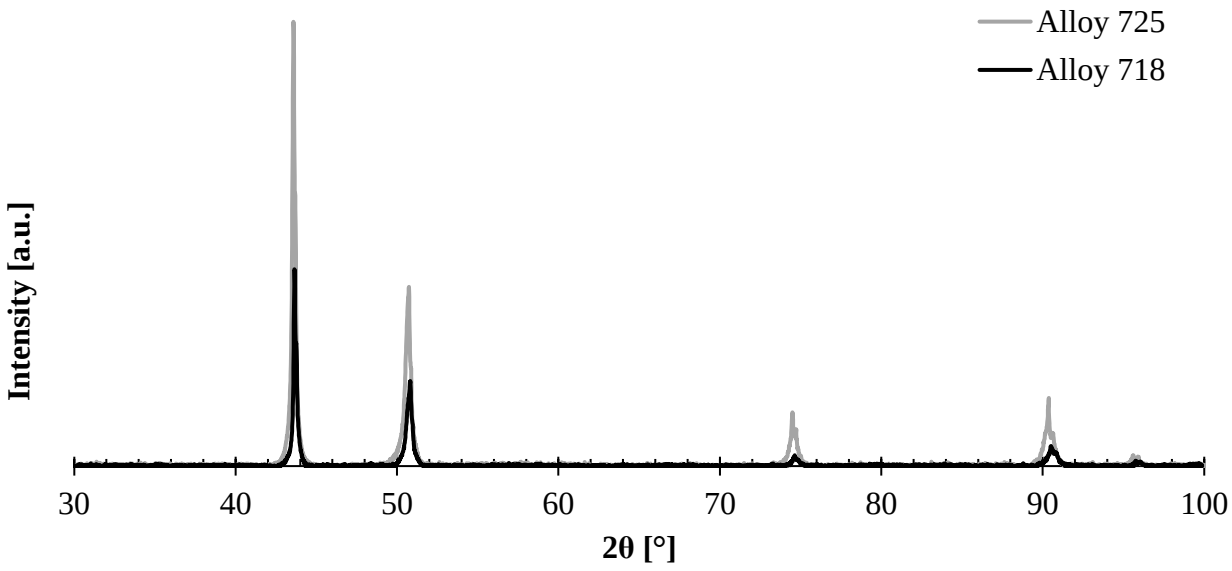

Figure 17 - XRD analysis of turbine blade in Alloy 718 and 725

To assess the possible presence of grain boundary precipitates below the detection limit of XRD, complementary intergranular corrosion tests were performed according to ASTM G28 Method A. Although this test is not specifically designed to directly evaluate stress corrosion cracking susceptibility, it can be considered an effective indicator of grain boundary sensitization and, consequently, of the potential presence of secondary phases along grain boundaries. The ASTM G28-A tests revealed a selective corrosion behavior in both Alloy 718 and Alloy 725, indicating a sensitized condition of the grain boundaries consistent with the applied aging heat treatments. High corrosion rates were measured for both materials, amounting to 1268 mdd for Alloy 718 and 1865 mdd for Alloy 725, in contrast with the reference Alloy 725 condition, which exhibited a significantly lower corrosion rate of 146 mdd. Moreover, the corrosion morphology observed after testing shows that, in both alloys, the attack is not homogeneous but rather localized along preferential paths, suggesting the occurrence of selective dissolution phenomena (Figure 18). Even if these results alone are not sufficient to conclusively identify or quantify specific secondary phases, they clearly indicate that both investigated components are sensitized which is generally recognized as the worst condition to SCC of nickel-based superalloys. These findings support the conclusion that the primary cause for SCC in Alloy 718 is its lower PREN value, which makes this alloy not suitable for geothermal applications involving aggressive chloride-containing environments.

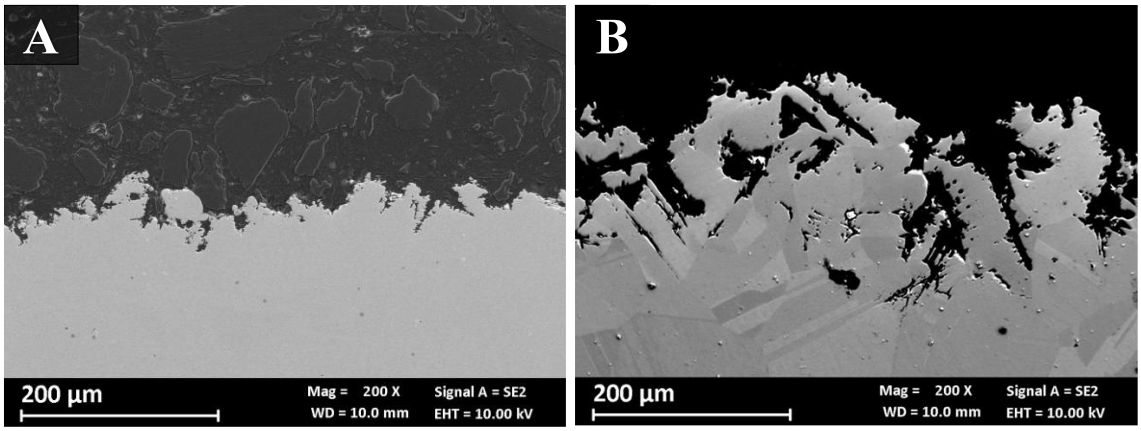

Figure 18 - Cross section of alloy A) 718 and B) 725 tested according to ASTM G28-A

3.4 Conclusion and perspective on the material selection obtained through AM

Turbine blades operating in geothermal power plants are exposed to highly aggressive conditions from both a mechanical and a corrosion point of view. High mechanical loads require the use of alloys with superior mechanical performance. In addition, the expansion and cooling of geothermal steam along the turbine stages lead to the DWP condition. These setting represents the most aggressive and detrimental environment. The working fluid becomes biphasic, inevitably promoting erosion phenomena, which can only be mitigated through appropriate material selection.

This study, based on a failure analysis approach, investigated the degradation state of geothermal turbine blades in order to assess the suitability of two nickel-based superalloys for this application. Both materials exhibited degradation associated with operation in biphasic geothermal fluids, confirming that erosion-corrosion under dew-point conditions is an unavoidable wear mechanism. However, Alloy 718 experienced also SCC and pitting corrosion due to its lower nickel content and reduced PREN compared to Alloy 725.

Despite its widespread use in high-temperature turbine applications and its availability for AM, Alloy 718 proved to be unsuitable for geothermal turbine blades operating under dew-point conditions.

Conversely, Alloy 725 exhibited superior resistance to environmentally assisted cracking and corrosion-related damage, confirming its potential as a reference material for geothermal turbine components. However, Alloy 725 is currently not commercially available for AM, and only one publication reports the production via AM [144]. In addition, Alloy 725 is a specialty alloy, characterized by high costs and limited market availability. These aspects provide the reasoning for the investigations presented in Chapther 5, which focus on the development and qualification of Alloy 725 for AM through material recovery from end-of-life components.

In parallel, Alloy 625 was also considered in Chapther 4. This material is already widely adopted in AM for industrial application. It possesses a PREN value comparable to Alloy 725, providing excellent corrosion resistance in aggressive environments. However, Alloy 625 is not precipitation-hardenable and therefore does not reach a yield strength required for geothermal turbine blade. Nevertheless, Alloy 625 represents one of the most promising materials for repair and surface engineering of geothermal turbine components through Direct Energy Deposition technology.

Chapther 4. Alloy 625 produced by different AM technologies

4.1 Chapter introduction

Alloy 625 is one of the nickel-based superalloys that has attracted significant interest in AM, as it is available for production through multiple AM routes, including LPBF, DED, MEX and BJ. However, each of these technologies is characterized by distinct metallurgical histories and consolidation mechanisms, which may lead to variations in both mechanical and corrosion behavior. This aspect is particularly relevant for Alloy 625, which is prone to the formation of secondary phases depending on the thermal history experienced during processing.

While several studies have demonstrated that Alloy 625 produced by fusion-based AM technologies, such as LPBF and DED, can achieve material properties comparable to those of conventionally manufactured material, a systematic understanding of novel sinter-based AM routes, including MEX and BJ, remains limited. Comparative investigations addressing multiple AM technologies under identical testing conditions are scarce, especially with regard to corrosion behavior.

For these reasons, the present chapter aims to provide a comparative assessment of the corrosion behavior of Alloy 625 produced by different AM technologies. The study focuses on identifying the influence of manufacturing-induced microstructural features on corrosion performance. The results presented in this chapter provide a critical basis for evaluating the suitability of different AM technologies for the production of Alloy 625 intended for applications in aggressive environments.

4.2 Materials and methods

4.2.1 Materials

Four AM technologies were considered to produce Alloy 625 (UNS N06625): LPBF, DED, MEX, BJ. Conventional hot working (HW) was studied as a benchmark. EOS Eosint M270 Xtended was used to fabricate LPBF-manufactured cylindrical specimens (5 mm in height and 15 mm in diameter). The composition of the feedstock powder, supplied by EOS Gmbh, is reported in Table 2. Detailed information regarding the equipment and processing parameters can be found elsewhere [145]. DED specimens were produced using a custom-built apparatus equipped with a laser beam and metal wire feedstock, with composition reported in Table 2. MEX-manufactured specimens were fabricated using a Metal X system by Markforged, employing a commercial Alloy 625 powder-loaded polymer filament with composition in accordance to ASTM B443 standard (Table 2). Further details on the

MEX and DED systems, along with their respective processing parameters, can be found in a previous study from the authors [11]. Shop System™ was used to produce BJ cylindrical specimens (5 mm in height and 15 mm in diameter). Thermal debinding and sintering were carried on with a Shop System™ Furnace, with a process gas composed of Ar and 3% of H_2 in volume and a maximum temperature of the sintering cycle of 1300 °C for 2 hours. Process parameters, gas flow, and further temperature and time of the cycles are secreted by Desktop Metal and remain undisclosed. Chemical analysis of BJ-produced specimens is reported in Table 2. A hot-worked bar with a diameter of 16 mm was used as benchmark material. The bar was supplied in the Grade 1 condition, in accordance with ASTM B446. Its chemical composition is also reported in Table 2.

Table 2 - Chemical composition of the studied materials.

Technology	C	Si	Mn	P	S	Cr	Mo	Ni	Nb	Ti	Al	Co	Ta	Fe
BJ	0.08	0.32	0.16	–	–	21.2	9.2	Bal.	3.56	–	–	–	–	2.7
LPBF	0.01	0.08	0.03	<0.001	0.002	22.4	8.2	Bal.	3.73	0.18	<0.01	0.17	0.13	0.45
DED	0.01	0.07	0.01	0.003	<0.001	22.3	9	Bal.	3.47	0.22	0.1	0.01	0.01	0.19
MEX	0.08	0.52	0.4	0.006	0.004	19.6	8.6	Bal.	3.28	0.022	<0.001	0.047	–	2.61
HW	0.036	0.25	0.19	0.007	0.001	21.6	8.3	Bal.	3.66	0.243	0.199	0.02	0.01	3.11
ASTM B443	Max 0.1	Max 0.5	Max 0.5	–	–	20–23	8–10	Bal.	3.15–4.15	Max 0.4	Max 0.4	Max 1	–	Max 5

4.2.2 Microstructural investigation

Methodology and experimental equipment for metallographic analysis and microscopy investigation are the same reported in chapter 3.2.2 – materials and methods, except for XRD analysis and SKPFM measurement.

The BJ-produced specimens were investigated by means of XRD. Measurements were carried out using a Bruker Advance D8 diffractometer equipped with Cu Kα radiation (λ = 1.541 Å). The instrument operated at 40 kV and 40 mA with a step size of 0.01°.

SKPFM measurements were carried out under ambient condition using a Park Systems NX10 atomic force microscope using a Pt-coated rectangular conductive cantilever (ElectriMulti75-G) characterized by 75 kHz resonant frequency and 3 N/m spring constant. Scans were performed at a 0.05 Hz scan rate and adopting single-pass methodology.

4.2.3 Hardness test

Vickers microhardness measurements were carried out using a UHL VMHT microhardness tester, applying a load of 1000 gf for 15 seconds (HV1). A minimum of 15 indentations were performed on each sample condition.

4.2.4 Electrochemical corrosion tests

Electrochemical tests were carried out on a circular area with 10 mm diameter. Before the test, samples were ground using SiC abrasive papers up to 4000 grit and polished with 1 μm diamond suspension. All specimens were cleaned with distilled water and soap, ultrasonically cleaned in acetone, and allowed to passivate in air for 1 hour. Duplicate tests were performed for each condition. The tests were performed in a 1 L standard three-electrode cell (according to ASTM G5), equipped with a PTFE sample holder, a Saturated Calomel Electrode (SCE) as the reference, and two graphite rods as counter electrodes. Prior to testing, the electrolyte was deoxygenated by nitrogen purging for 24 hours and kept under continuous nitrogen flow throughout the measurements. The temperature was maintained using a thermostatic bath and monitored by a standard thermometer. Tests consisted

in Open Circuit Potential (OCP) monitoring for 1 hour followed by potentiodynamic or potentiostatic polarization tests.

The test solutions consisted of 0.5 M H_2SO_4 at 30 °C (prescribed by ASTM G5) to evaluate the corrosion behavior in acidic and oxidizing solution. The effect of chloride ions and acidity was evaluated with polarization tests in 0.6 M NaCl both near-neutral (pH 7) and acidic (pH 3, acidified with HCl) at 40 °C. These environments have been selected as they can be representative of common conditions in marine and Oil&Gas applications.

Anodic potentiodynamic polarization tests were performed at a scan rate of 10 mV/min, starting from 10 mV below the OCP up to 1 V vs. SCE. The potential scan was then reversed until reaching 50 mV below the repassivation potential, except for tests conducted in 0.5 M H_2SO_4. To evaluate the corrosion current density, the anodic Tafel region was identified within the potential range between +100 and +150 mV with respect to the open circuit potential. The current density in passivity region was determined as the average current density within the passive region, defined between 0 V and +0.5 V for the test solution at pH 3, between −0.1 V and +0.3 V for the neutral solution, and between +0.1 V and +0.7 V for the 0.1 M H_2SO_4 solution. The breakdown potential was defined as the potential at which the anodic current density reached 10 μA cm^{-2}, corresponding to the onset of localized breakdown of the passive film.

Potentiostatic tests were performed at fixed potentials of +200 mV or +500 mV vs. SCE for 24 hours in neutral NaCl solution (pH 7) and in the acidified chloride solution (pH 3). The data acquisition rate was set to 1 Hz. Passivation current density has been calculated as a mean of current density value of the last 2 hours of tests.

4.2.5 Intergranular corrosion test

Susceptibility to intergranular corrosion tests were performed in compliance to ASTM G28 standard method A and detailed information can be found in chapter 3.2.3 – Corrosion tests.

4.2.6 Immersion corrosion test in sulfuric acid

Immersion corrosion tests were performed in accordance with ASTM G31. Methodology, experimental set-up and specimen preparation steps are equal to intergranular corrosion test G28 method A. The considered solution consists of 50 wt.% H_2SO_4 solution at 50 °C, 80 °C, and boiling temperature (120 °C). After 24 hours of immersion, the specimens were removed from the solution, washed with distilled water, rinsed in acetone, and dried. They were then reweighed to determine the

mass loss. All corroded specimens were subsequently examined by OM and FESEM for surface analysis.

4.3 Results and discussion

4.3.1 Microstructural investigation and defects characterization

Porosity values obtained through image analysis are reported in Table 3. Alloy 625 produced by means of LPBF and DED showed an excellent relative density, comparable to the values currently reported in literature [146,147]. Otherwise, AM techniques with polymer support exhibited a significantly higher porosity. These results underline the need of more effort to fully develop polymer-assisted AM processes, unlike well-established AM technologies such as LPBF and DED.

Table 3 – Volumetric porosity and relative fraction pores with Feret diameter higher than 50 µm

Manufacturing technology	LPBF	DED	MEX	BJ
Porosity (%)	0.06	0.06	3.54	1.7
Pores > 50 µm (%)	0	0.02	0.37	0
Reference	[11]	[11]	[11]	-

Porosity values are critical and can be detrimental for several material properties as already reported in literature [148,149]. Despite specimens produced by BJ, revealed the presence of numerous pores, they were relatively small (<50 µm), with spherical shape, and homogeneously distributed within the material. This pore morphology has been demonstrated to be the least detrimental to the mechanical properties [150]. In contrast, MEX-processed specimens displayed both small, spherical porosity and macro-defects induced by the filament deposition during the printing process. Such process-induced macro-defects are strictly related to the adopted scanning strategy, and sintering proved to be ineffective in closing these cavities. In fact, they are periodic, elongated, and interconnected, forming a network of channels along all the samples as visible in Figure 19. A previous study analyzed the nature of these defects and how affected mechanical properties and IGC resistance [11,12].

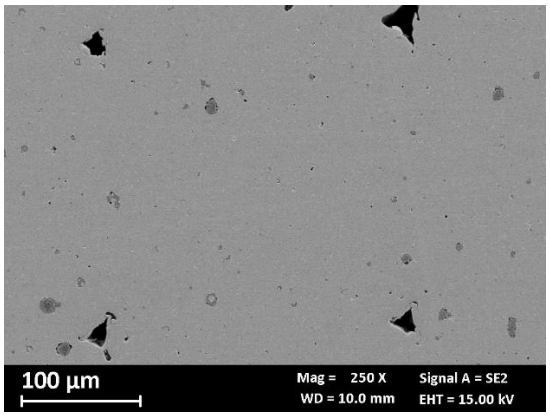

Figure 19 - Cross section of MEX-manufactured specimen showing macro-defects

Moreover, Jasik et al. [9] highlighted the presence of process-inherent macro-defects that parts fabricated by MEX can exhibit a reduction in tensile strength compared to laser-based processes. Similarly, Suwanpreecha et al. [151] demonstrated that path-to-path voids degrade mechanical strength of MEX parts. Lorenzi et Al. reported that the defect pattern interconnection impacts on the overall plastic deformation, limiting ductility and promoting premature failure depending on the scanning strategy adopted [12]. The absence of endogenous macro-defects is a promising result for BJ technology, revealing that this sintering-based process does not lead to the formation of critical defects in the produced material.

Microstructural analyses highlighted another relevant difference between AM technologies involving in-process fusion (LPBF and DED) and those relying on post-processing treatments to consolidate the part (MEX and BJ). In fact, Alloy 625 produced by BJ exhibited coarse equiaxed grain structures with several twins and elongated Nb-, Mo- rich phases along the grain boundaries. Similarly, MEX specimens exhibit austenitic, equiaxed grains with the presence of globular Nb-, Mo- rich phases. In addition, MEX material also showed a high number of inclusions rich in Al, Si and Cr. These were identifiable as aluminum- and chromium-oxides, and were surrounded by secondary phases enriched in Mo and Nb. Conversely, Alloy 625 produced by LPBF was characterized by epitaxial columnar grains composed by fine cellular/dendritic substructures. The characteristic melt pools of this technology were also visible. The specimens manufactured by DED consisted of large dendritic regions with some small (≈ 1 µm) oxide inclusions. Oxides were probably generated during DED process due to the lack of a sealed process chamber and the high affinity of oxygen with Ti, Al and Cr. The finer microstructures observed in Alloy 625 obtained via LPBF can be attributed to the higher cooling rate ($\approx 10^6$ K/s) compared to wire-based DED process ($\approx 10^3$ K/s) [152,153]. Finally, conventional HW 625 was characterized by the typical microstructure for the annealed material, which consists of equiaxed austenitic grains with twins.

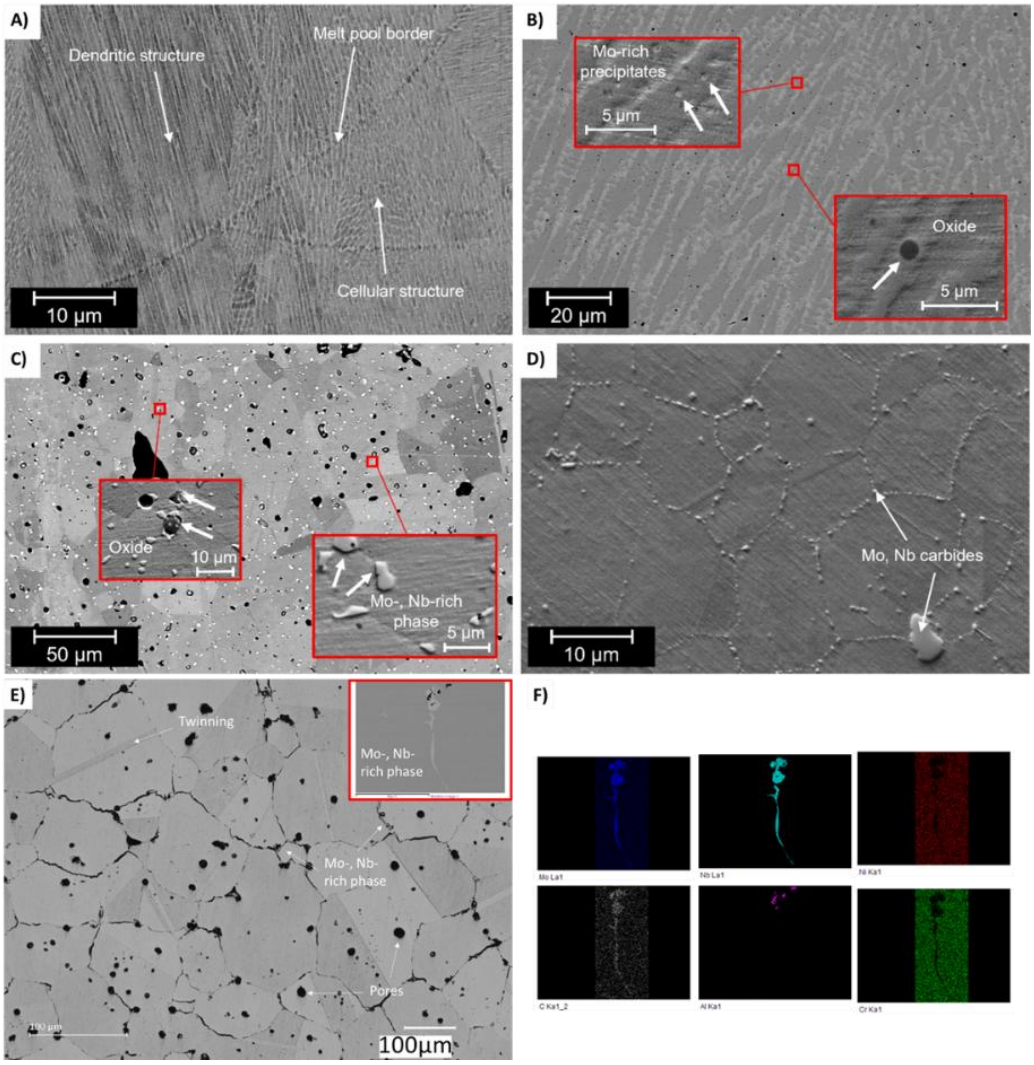

Figure 20 - Microstructures of the LPBF (a), DED (b), MEX (c), HW (d) and BJ (e) specimens adapted from Carrozza et Al.[11].

Alloy 625 can exhibit several secondary phases, including ordered fcc γ′, ordered body-centered tetragonal γ″, oxide, carbides (MC, $M_{23}C_6$ and M_6C types) and intermetallic compounds. The formation, stability and distribution of these phases strongly depend on the thermal exposure, specifically the temperatures reached and the duration of the heat treatments [154,155]. The characterization of the secondary phases highlighted a complete difference in both type and distribution of precipitates depending on the manufacturing technology. LPBF and DED samples exhibit a microstructure without visible precipitates with FESEM observations. Mohammadpour et Al. [156] identified the presence of NbC in the interdendritic areas of the microstructure in Alloy 625 produced by means of LPBF. Conversely, Mo-rich precipitates were detected in the interdendritic regions of the DED processed specimens, as confirmed by the literature [157–159]. Marchese et al. [160] demonstrated through transmission electron microscopy (TEM) that very small (<100 nm) Nb-rich MC carbides are present in this material. In contrast, MEX specimens are characterized mainly

by M_6C carbides, distributed throughout the entire austenitic matrix, occurring in a blocky morphology and elongated along the grain boundaries [11]. In the BJ specimens, the carbides are intergranular and very large in size, being visible even at low magnifications during OM observation just after polishing. XRD analyses confirmed that these grain-boundary segregations correspond to MC carbides (Figure 21).

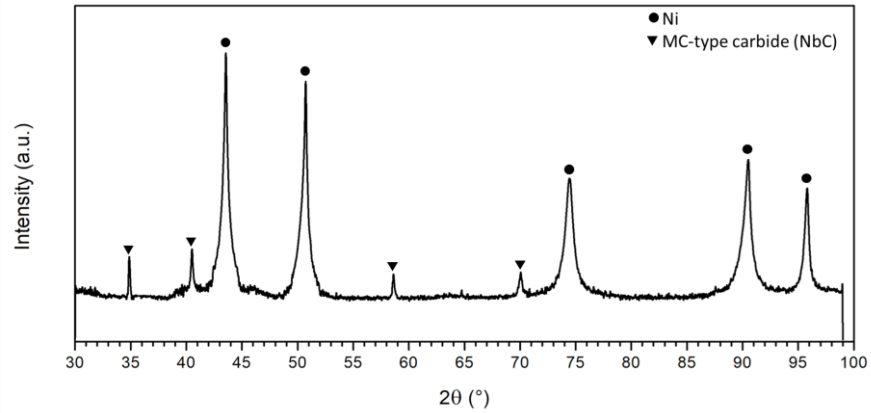

Figure 21 - XRD analysis of Alloy 625 obtained by means of BJ

For sinter-based AM, the difference in carbide is primarily governed by the sintering cycle parameters. Floreen et al. [155] characterized the formation the carbide in Alloy 625, showing that MC carbides, mainly NbC with minor amounts of Mo, Ni and Cr, tend to form already during solidification and remain thermodynamically stable up to approximately 1090 °C. In contrast, M_6C carbides, rich in Mo and Cr, typically develop only after prolonged exposures at intermediate temperatures. Aditya et al. [161] investigated Alloy 625 fabricated by MEX and reported the presence of MC carbides after sintering at 1290 °C. In their study, samples sintered for 5 min displayed spherical uniformly distributed carbides, while sintering for 4 h exhibited coarsened carbides preferentially located at grain boundaries. Similarly, Enrique et al. [162] found that Alloy 625 produced via Binder Jetting develops MC carbides along grain boundaries, a phenomenon attributed to elevated carbon levels during sintering due to the residual binder decomposition. Mostafaei et al. [163] also observed the formation of MC carbides during sintering at 1280 °C, as well as during subsequent aging treatments of BJ-processed Alloy 625. The difference in carbide types between MEX and BJ can therefore be attributed to the specific thermal process experienced during consolidation. Moreover, the composition of feedstock filament for MEX process has 0.52% of Si, which was found to facilitate the formation M_6C type carbides. Indeed, Jiang et al. [164] demonstrated that silicon additions promote the formation of M_6C rather than M_2C carbides in Ni-Mo-Cr alloys. Flooren et Al. [155] showed that increasing silicon content in Alloy 625 enhances the formation of

M_6C carbides and Laves phases, whereas higher carbon content increases the tendency to precipitate MC carbides. It is worth noting that both BJ- and MEX-processed alloys exhibit relatively high carbon contents, although still compliant with ASTM B443 standard. The control of carbon concentration is a critical point for sinter-based AM techniques. Several studies confirmed that the process parameters of debinding and sintering strongly influence the residual carbon content and, consequently, the carbide precipitation. For instance, Lecis et al. [165] demonstrated that adopting reducing Ar atmosphere during debinding increases the carbon content in BJ-manufactured stainless steel 316L. Raza et al. [166] similarly investigated different atmosphere in post-processing powder-injection-moulded 316L achieving <0.01 %C in vacuum condition. In H13 tool steel, Nandwana et al. [167] demonstrated that higher binder saturation results in higher carbon retention which led to carbide precipitation, due to incomplete removal of polymeric residues. Levenfeld et al. [168] characterized the carbide evoution in M2 tool steels, demonstrating that M_6C are always present. More recently, Schnell and Colin [169] showed that debinding can trigger the formation of MC-type carbides during sintering in BJ-manufactured Inconel 718. All these results clearly indicate that optimizing post-printing processes is a crucial aim for controlling both chemical composition and microstructure of metals produced with sinter-based AM routes. Finally, the benchmark HW material was characterized by MC-type carbides, rich in Mo and Nb, whose are intergranular and elongated in shape due to the low cooling rate achieved at the end of the hot working process.

4.3.2 Hardness

Hardness values of AM-processed Alloy 625 highlighted a clear difference between fusion-based and sinter-based AM techniques, as shown in Figure 22. Specimens produced by LPBF and DED exhibited high hardness, mainly due to the very fine dendritic microstructure. In particular, LPBF samples showed slightly smaller dendritic cells, resulting in the highest hardness values. Conversely, materials consolidated through sintering displayed a course, equiaxed grain microstructure leading to lower hardness values compared to fusion-based AM. BJ specimens showed a slightly larger grain size and, consequently, a lower hardness (180 ± 6 HV) compared to MEX specimens.

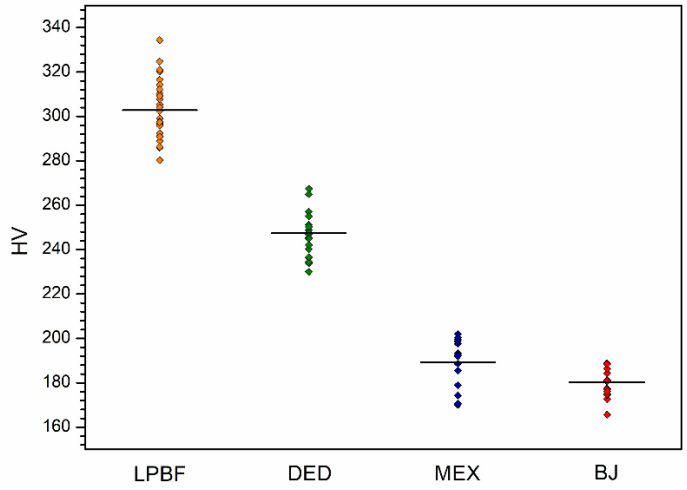

Figure 22 - HV1 test for the AM-processed specimens (the horizontal lines represent the average values) adapted from Carrozza et Al. [11].

4.3.3 Intergranular corrosion

Results of corrosion tests in boiling ferric sulfate/sulfuric acid solutions (ASTM G28 Method A) evaluated the susceptibility of intergranular corrosion of Alloy 625 in function of AM technique considered. Average corrosion rates, visible in Figure 23, underlined a different behavior between AM technologies.

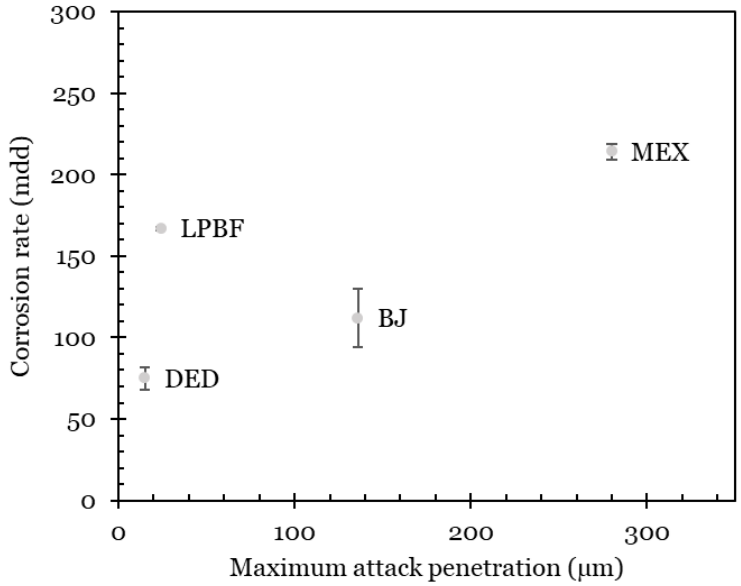

Figure 23 - Corrosion rates and maximum attack penetration after ASTM G 28-A tests on Alloy 625 produced by means of different AM techniques. LPBF data from [170] and DED data from [11]

DED-processed specimens exhibited the best corrosion behavior, showing both the lowest corrosion rate and the smallest maximum penetration depth. LPBF-processed Alloy 625 displayed higher corrosion rates but the maximum penetration attack remained very limited. In contrast, BJ-processed specimens showed a corrosion rate slightly lower than that of LPBF, but a markedly higher maximum penetration depth. No significant evidence of intergranular attack was detected in either the LPBF or DED-processed materials.

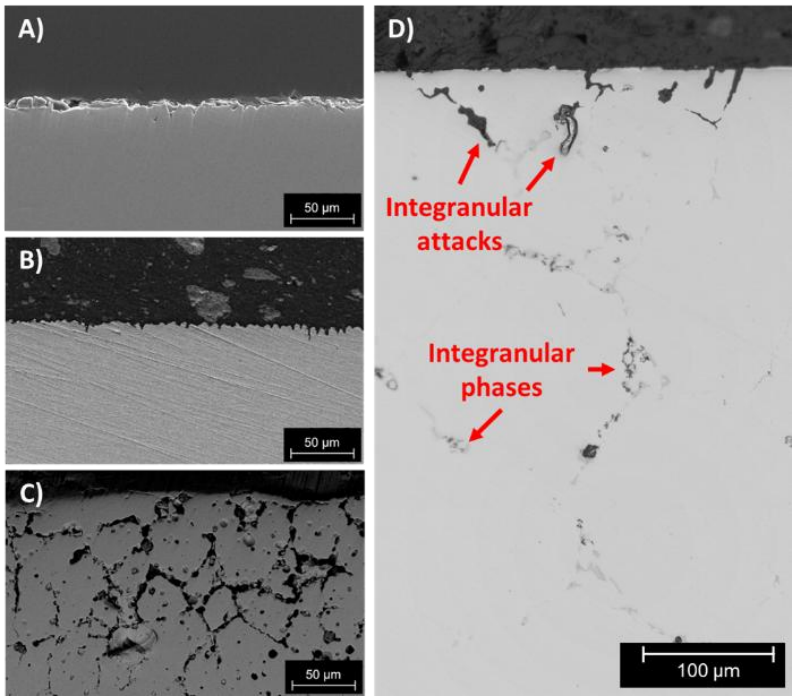

Figure 24 - Cross section of specimens after ASTM G28-A test produced by different AM techniques. A) LPBF [170] B) DED, C) MEX [11] AND D) BJ

Conversely, both BJ and MEX specimens displayed evident intergranular corrosion attacks, as visible in Figure 24, indicating that the selective corrosion path followed the distribution of carbides. The relatively low overall corrosion rate measured for BJ can be partially attributed to its very coarse grain structure as reported in Table 4. Indeed, larger grains are known to reduce the number of grain boundaries per unit area, thereby reducing the IGC susceptibility and lowering the related corrosion rate [171].

Table 4 - Grain size of specimen produced by MEX and BJ following ASTM E 112

Technology	Mean intercept (mm)	ASTM grain size number
MEX	0.03	6.5
BJ	0.12	2.7

The difference in corrosion penetration and corrosion rate between the MEX- and BJ-processed specimens cannot be explained only considering the grain size. The susceptibility of intergranular corrosion in Alloy 625 is associated with the formation of secondary carbides enriched in Cr and Mo. This precipitation causes a depletion of corrosion-resisting elements in the area surrounding the grain boundary, and this area becomes anodic to the remainder of the grain [74]. It is well recognized that niobium additions are used to reduce the susceptibility to IGC, avoiding the formation of Cr-, Mo-depleted zones. The addition of Nb, Ti, and Ta controls the formation of Cr-, Mo-rich carbides ($M_{23}C_6$ and M_6C) by promoting the precipitation of MC-type carbides [74,172,173]. In XRD analysis, MEX-produced specimen showed M_6C carbides while Alloy 625 obtained by means of BJ exhibited MC-type carbides enriched in Nb. This distinction has played a fundamental role in the IGC behavior. To deeply investigate how different carbides influence the corrosion behavior of Alloy 625, SKPFM measurements were also carried out. The results of these measurements are reported in Figure 25. LPBF and DED specimens showed very small local Volta potential variations (≈10 mV) within the microstructure. Slight differences were also observed between sub-grains and their boundaries in LPBF, and between dendritic and interdendritic regions in DED. These gradients are consistent with the local Nb- and Mo-enriched segregations reported for fusion-based Alloy 625 [174,175]. Slight local Volta potential difference may explain the light interdendritic morphology observed in DED cross-sections (≈10 μm), as documented in the literature [175]. Oxide inclusions in DED has a Volta potentials of 100 mV higher than the austenitic matrix, but the IGC results suggested that they do not act as efficient cathodes. In contrast, sinter-based materials exhibited pronounced Volta potential differences between carbides and the γ matrix. In MEX-specimens, oxide inclusions displayed the highest potentials (≈ +150 mV vs γ-Ni), whereas M_6C carbides exhibited significantly lower potentials (≈ -50 mV) with respect to the matrix. To the best of our knowledge, no previous investigations have been carried out on the electronic behavior of M_6C carbides. These findings contradict the well-documented correlation between volta potential values and anodic or cathodic behavior of phases. However, recent studies have reviewed in depth why the direct correlation between the potential differences measured by SKPFM and galvanic corrosion activity cannot be generalized, as this relationship is complex and depends on the material, the environmental conditions, and the specific analytical approach used [176,177]. Schmutz and Frankel, who first introduced this technique for characterizing corrosion behavior, had already highlighted that certain intermetallic in aluminum alloys do not follow this correlation [178,179]. Liew et al [180] reported different second phases in aluminum alloy AA5083 with higher Volta potentials than the matrix in air, however Mg_2Si have a nobility inversion under ambient condition. An inverse correlation between the measured Volta potential difference and the observed corrosion behavior has been

reported also for a biphasic nickel aluminum bronze [181]. Conversely, BJ-manufactured specimens showed Nb-rich MC carbides with a difference of approximately +100 mV of Volta potential compared to austenitic grains. Lourenço et Al. [182] has already investigated Alloy 625 through SKPFM and found that laves phase presented negative Volta potentials while MC presented positive Volta potentials compared to the matrix. Guo et Al. [183] highlighted Laves and G phases with nearly 80 mV lower than matrix in Alloy 625 welds. Kong et Al. demonstrated that TiC particles have a higher Volta potential than the austenitic grains in Alloy 718 [175]. Overall, the SKPFM results demonstrated that both MC and M_6C carbide types are characterized by a difference in Volta potential if compared to the matrix, and both played a crucial role in defining the IGC behavior of Alloy 625.

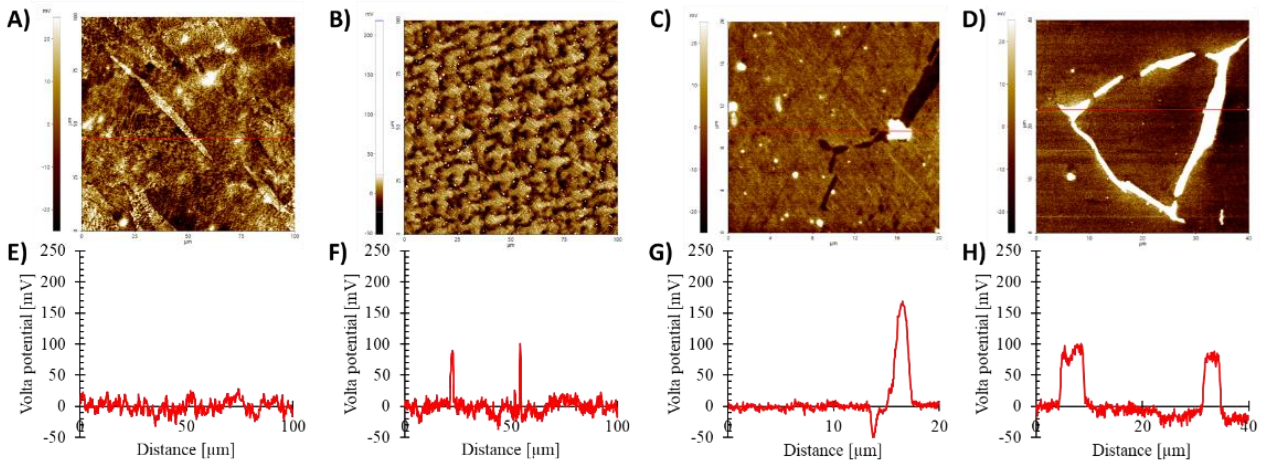

Figure 25 – Volta potential map measured under ambient condition using AFM of Alloy 625 produced by means of LPBF A), DED B), MEX C) e BJ D) measured under ambient condition using AFM. The red line refers to the line scan potential profile of E) LPBF, F) DED, G) MEX and H) BJ.

4.3.4 Electrochemical corrosion tests

Potentiodynamic polarization tests are reported in Figure 26. The tests performed in 0.5 M H_2SO_4 (pH ≈ 1) revealed an excellent passive behavior, with an extended passive region up to oxygen evolution potential (≈ 0.93 V vs SCE). This indicated a highly stable oxide film throughout the entire anodic polarization for Alloy 625 produced with every technology considered. Test conducted in neutral (pH 7) 0.6 M NaCl solution showed also comparable behavior of the studied materials, all characterized by effective passivation. The breakdown potential likely corresponds with the transition from $Cr(OH)_3$ to $HCrO_4^-$ reported in Pourbaix diagram of Cr, suggesting the absence of any localized corrosion initiation [184]. This interpretation was further supported by the reverse scan, which exhibited no hysteresis. Conversely, relevant differences among the different manufacturing routes

were noticed during tests in acidified (pH 3) 0.6 M NaCl solution. Also in this case, there is a clear distinction in corrosion behavior between material produced by means of fusion-based additive processes (LPBF, DED), and sinter-based technologies. Alloy 625 obtained through fusion-based AM showed excellent corrosion resistance comparable to the wrought alloy, with the formation of a stable passive film up to potentials associated with CrO_4^{2-} formation. In contrast, materials produced through sinter-based manufacturing displayed compromised passive film stability, with the appearance of an instability region already during the forward scan in MEX-produced specimens (Figure 26H). For both sinter-based technologies, the reverse scan shows pronounced hysteresis (Figure 26F), indicative of localized corrosion attack that did not completely repassivate until reaching a potential of approximately +0.1 V vs SCE. This behavior was confirmed by FESEM observations, which revealed the presence of crevice corrosion under the gasket (Figure 26I).

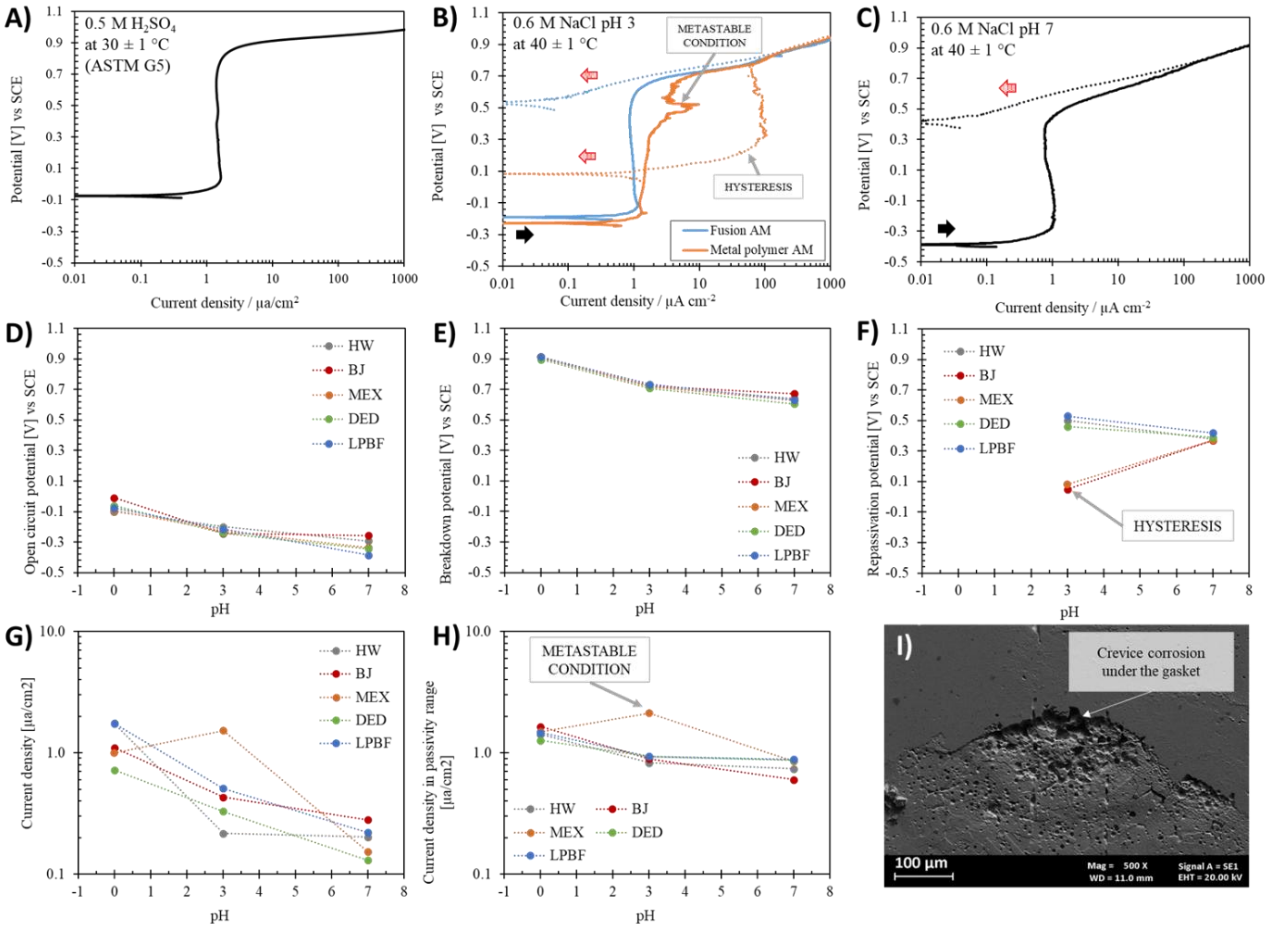

Figure 26 - Potentiodynamic polarization curves of Alloy 625 produced by mean of different AM technologies in A) 0.5 M H2SO4 (pH0) and 0.6 M NaCl at B) pH3 and C) pH7. The corresponding values of open circuit potential, breakdown potential, repassivation potential, current density and current density in passivity range are reported respectively in D), E), F), G), H). Image FESEM analysis showing crevice corrosion in sintered based AM are visible in I).

The excellent corrosion behavior of this alloy was also demonstrated by the potentiostatic polarization tests. The average current density of last two hours of tests are reported in Figure 27. All potentiostatic tests showed a rapid decrease in current density, which stabilized within a few hours and remained essentially constant for the whole duration of the experiment. These findings indicated the absence of any localized corrosion initiation and a formation of a protective oxide film on the surface under all conditions. A slight increase in current density was observed when polarizing at 500 mV at pH 3, which can be ascribed to a minor reduction in passive film stability in such condition. In contrast, in neutral solution a more pronounced increase in current density occurs at 500 mV, as this potential is at the beginning of the transpassive region.

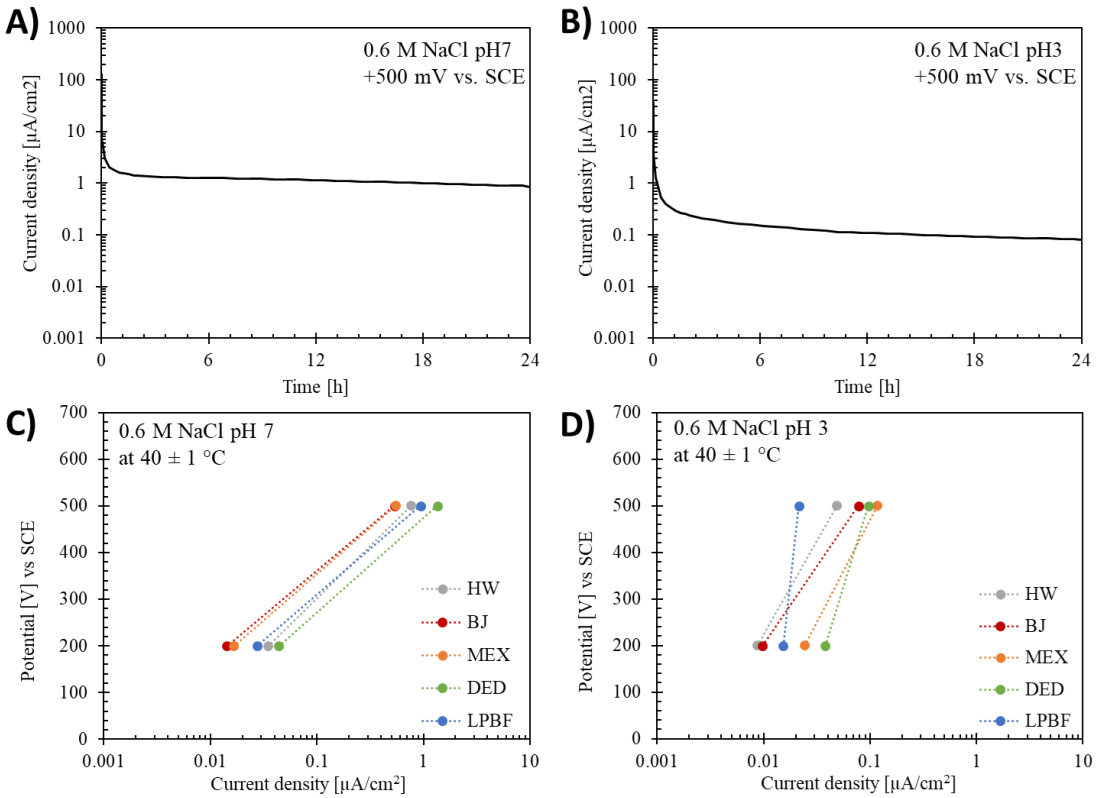

Figure 27 - Potentiostatic polarization curves of Alloy 625 produced by mean of different AM technologies in 0.6 M NaCl at A) pH7 and B) pH3. The corresponding values of current density at C) pH7 and D) pH3

4.3.5 Corrosion in acidic media

The immersion tests in 50 wt.% H_2SO_4 conducted at 50 °C, 80 °C, and boiling temperature revealed a strong dependence of the corrosion rate of Alloy 625 on temperature due to the loss of passivity and the acceleration of both anodic and cathodic reaction kinetics. This behavior was observed for specimen obtained with every manufacturing technology considered and is visible in Table 5. At 50

°C, Alloy 625 maintained excellent corrosion resistance except for the MEX-manufactured alloy, that showed a markedly higher corrosion rate (≈ 0.2 mm/y). Increasing the temperature to 80 °C resulted in a significant worsening for all manufacturing routes, with corrosion rates rising by one to two orders of magnitude. The conventionally manufactured Alloy 625 exhibited the lowest corrosion rate, about one-third than the AM counterparts. At boiling temperature, all materials experienced severe weight losses, but HW condition experienced again the lowest corrosion rate.

Table 5 - Weight loss and corrosion rates of Alloy 625 produced by different technologies after 24 h immersion in 50 wt.% H_2SO_4 at 50 °C, 80 °C, and boiling temperature.

Temperature [°C]	Technology	Weight loss [mg]		Corrosion rate [mm/y]	
		Mean	Dev. St.	Mean	Dev.St.
50	BJ	0.07	0.10	0.01	0.01
	DED	0.13	1.25	0.01	0.00
	HW	0.16	0.28	0.01	0.01
	LPBF	0.18	0.01	0.01	0.01
	MEX	3.29	0.36	0.23	0.06
80	BJ	27.20	0.08	1.92	0.21
	DED	20.26	0.38	1.56	0.15
	HW	9.59	0.11	0.63	0.00
	LPBF	35.25	1.29	2.47	0.66
	MEX	29.78	1.24	2.01	0.53
Boiling temperature	BJ	475.62	0.06	33.50	10.50
	DED	247.82	0.58	19.07	7.78
	HW	111.75	0.06	7.31	0.83
	LPBF	400.40	0.73	28.80	5.25
	MEX	616.78	1.29	41.38	4.89

The surface of MEX-manufactured specimens after tests at 50°C revealed corrosion phenomena following microstructure texture, while for Alloy 625 obtained with the other technologies there was no evidence of corrosion at this temperature, as visible in Figure 28. After tests at 80 °C, preferential grain-boundary attacks were observed in the HW, MEX, and BJ Alloy 625 specimens, confirming that carbides promoted micro-galvanic coupling with γ-matrix. Furthermore, specimens produced by LPBF and DED exhibited a corrosion morphology that reflects columnar grains and dendritic structures, respectively. At boiling temperature, the exposed surface of every condition exhibited severe corrosion phenomena, with a morphology that make difficult to distinguish microstructure-related corrosion path due to the extensive material loss. MEX-produced specimens were

characterized by the highest corrosion rates in every temperature considered. These results can also be ascribed by the process-induced cavities. Indeed, macro-defects were proved to widen during exposure to H_2SO_4 solution, indicating that corrosion preferentially propagates inside the defect increasing the overall surface exposed to the aggressive environment.

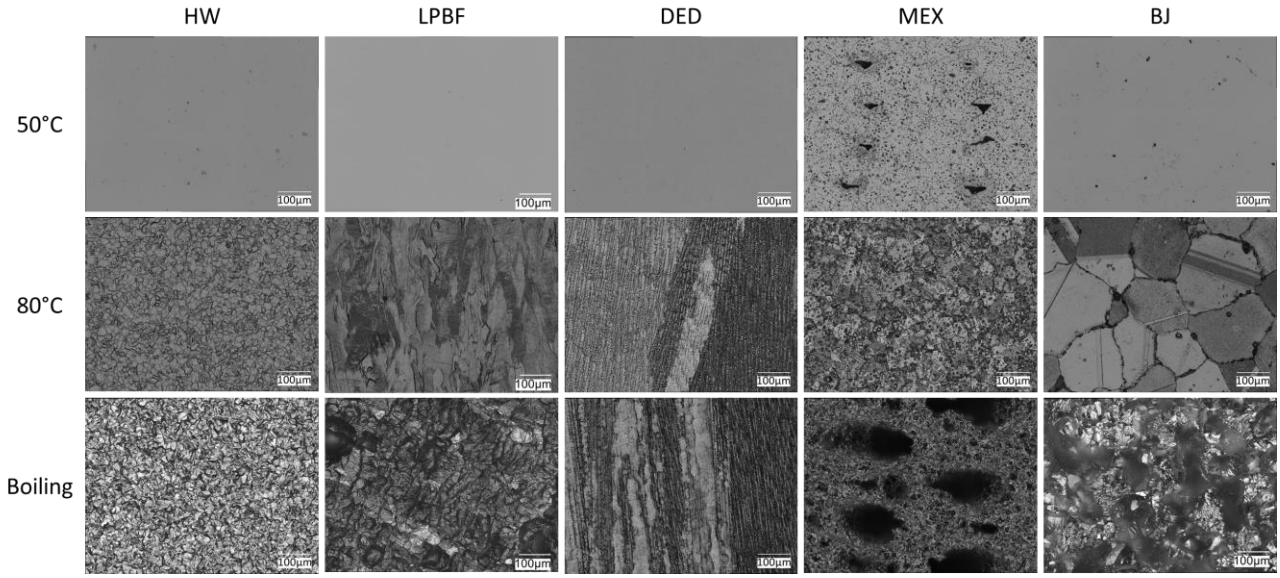

Figure 28 - Optical image analysis of exposed surface of Alloy 625 to 50% of H_2SO_4

Further SEM analyses demonstrated that the anodic stimulation of carbides also occurs in strongly acidic environment, promoting micro-galvanic coupling with preferential dissolution of grain boundary zones, as shown in Figure 29. This effect was clearly visible in microstructures with equiaxed austenitic grains, where carbides are predominantly located along the grain boundaries, thereby facilitating preferential attack along these regions.

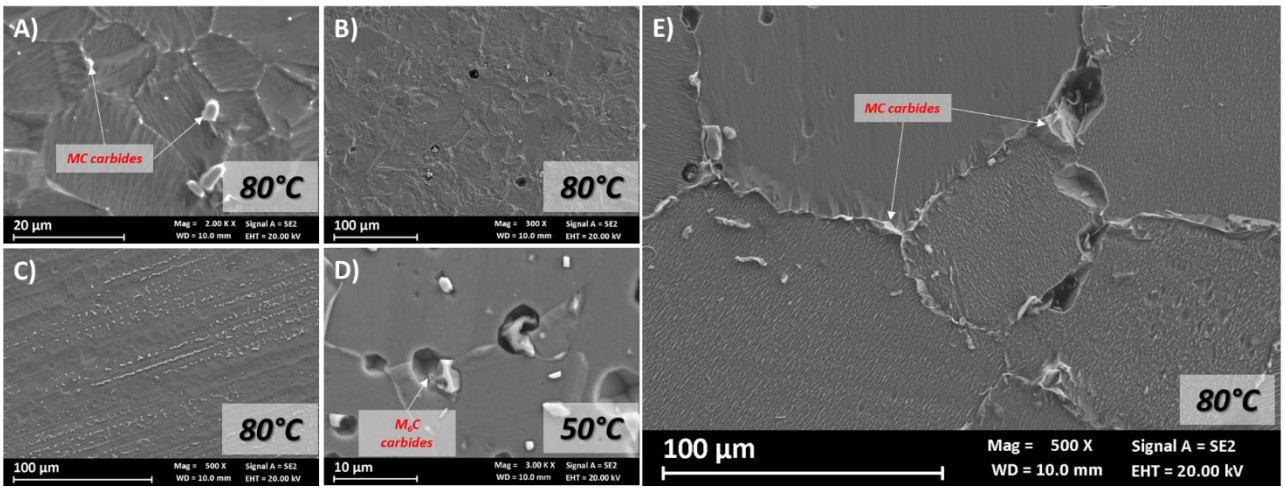

Figure 29 - FESEM image analysis of exposed surface of Alloy 625 to 50% of H_2SO_4 produced by means of A) HW, B) LPBF, C) DED, D) MEX and E) BJ

Iso-corrosion maps are useful to predict corrosion rates of materials in specific environments before industry applications [185,186]. Therefore, the corrosion behaviors found in this work were compared with the standard iso-corrosion maps found in the literature [187]. The corrosion rates achieved were compliant with iso-corrosion maps of Alloy 625 in H_2SO_4 solutions, except for MEX-manufactured specimens during the tests at 50°C (Figure 30).

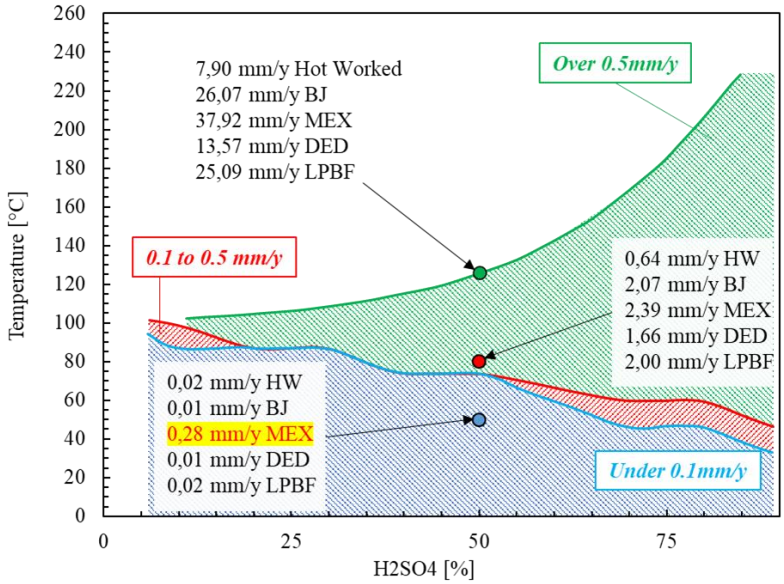

Figure 30 - Corrosion rate of Alloy 625 obtained by means of different AM techniques in immersion tests in H_2SO_4 at different temperatures [187]

The high corrosion rates observed for Alloy 625 produced by MEX can be primarily attributed to the microstructure and then to the presence of macro-defects. As shown in Figure 28, the entire surface of the MEX specimens exposed to sulfuric acid at 50 °C exhibited corrosion phenomena. This finding suggests that even in the absence of defects, MEX-processed Alloy 625 would not be able to maintain a stable and protective oxide film displaying corrosion rates not compliant with the expected performance of this material.

4.4 Conclusion

This study provides an overview of the corrosion behavior of Alloy 625 produced by different AM technologies, in comparison with the conventionally hot-worked material. The investigation of microstructure, defects, electrochemical behavior, intergranular corrosion susceptibility, and immersion tests in acidic media provides a clear description of how different AM techniques can affect the corrosion behavior of Alloy 625.

The results demonstrated that AM technologies can successfully produce Alloy 625 with corrosion behavior comparable to benchmark, except for MEX where intrinsic process-induced macro-defects strongly affect both corrosion resistance.

Fusion-based technologies (LPBF and DED) are characterized by rapid solidification, which leads to fine cellular or dendritic microstructures and annihilating coarse carbides segregation. Therefore, they exhibit high mechanical properties, no susceptibility to intergranular corrosion and good corrosion behavior in harsh acidic environments.

In contrast, Alloy 625 obtained through sinter-based technologies has a microstructure and carbide type determined by specific post-processing. Sintering processes led to coarse austenitic grains and presence of carbides predominantly located along grain boundaries. These features significantly compromised both mechanical properties and intergranular corrosion resistance. Nevertheless, BJ specimens, containing Nb-rich MC carbides, showed lower susceptibility to intergranular corrosion than MEX.

Although sinter-based technologies do not yet match the microstructural and corrosion performance of LPBF and DED, Binder Jetting seems to represent a promising AM technology to produce Alloy 625 components.

Chapther 5. Development and qualification of Alloy 725 for AM

5.1 Chapter introduction

The failure analysis discussed in Chapther 3 indicated Alloy 725 as an excellent material for turbine blade operation in DWP condition in a direct-cycle geothermal plant. However, Alloy 725 is currently largely unexplored for AM [144]. As a consequence, there is a lack of systematic studies addressing the feasibility of processing Alloy 725 by AM technologies and evaluating the resulting microstructure, mechanical properties, and corrosion behavior. Moreover, the adoption of AM becomes especially relevant for expensive and low-availability materials, where the implementation of closed-loop material would be a winning strategy. In this context, EGP provided decommissioned turbine blades, like the one analyzed in Chapter 3, for a feasibility study focused on material recovery. The powder atomization was carried out in collaboration with Politecnico di Torino, followed by specimen production via LPBF technology in collaboration with the University of Bergamo.
The present chapter focuses on the mechanical, corrosion and microstructural characterization of recovered Alloy 725, providing a comparison between the original material and the new material produced by AM. As a benchmark, a forged Alloy 725 was also included in the study to evaluate the effect of precipitation hardening by comparing LPBF-processed material with its conventionally manufactured counterpart.

5.2 Materials and methods

5.2.1 Feedstock production

The Alloy 725 powder was produced from twenty ex-service turbine blades provided by Enel Green Power S.p.A. These end-of-life components were in the same material condition as the Alloy 725 considered in Chapther 3 and the chemical composition can be seen in Table 6.

Table 6 – Mean value and deviation standard of chemical composition of ex-service turbine blade made of Inconel 725 (wt%)

Element		Fe	Ni	Cr	Mo	Ti	Nb	Al	Si
Turbine blades	Mean [%]	7.62	56.42	21.37	8.75	1.61	3.77	0.27	0.18
	D.St. [%]	0.65	0.54	0.36	0.34	0.13	0.18	0.07	0.11
ASTM B805	Max	/	59.00	22.50	9.50	1.70	4.00	0.35	0.20
	Min	/	55.00	19.00	7.00	1.00	2.75	/	/

The atomization has been carried out through a VIGA atomizer which further details of experimental setup are reported in [188]. Before the atomization, the turbine blades were sandblasted and mechanically cut into smaller pieces and loaded into an alumina crucible. The material was melted through induction heating under vacuum conditions (approximately 6×10^{-12} mbar), followed by backfilling with inert gas at around 1000 °C to limit the evaporation of alloying elements with low vapor pressure. The molten alloy was superheated to 1540 °C to reduce melt viscosity. Gas atomization was carried out using argon both as cover gas and as atomizing medium. The atomization chamber was pressurized to 1.24 bar to ensure a stable flow of molten metal through the melt delivery nozzle. Alumina crucibles and delivery tubes were adopted in accordance with industrial practice to reduce chemical contamination of the melt. Three atomization trials were performed by progressively increasing the atomization gas pressure from 35 to 45 bar to identify the optimal compromise between powder yield and process stability. As shown in Table 7, the chemical composition of the obtained powder is compliant with ASTM B805 standard for Alloy 725.

Table 7 - Chemical composition of the Inconel 725 recycled powder (wt%)

Element		Fe	Ni	Cr	Mo	Ti	Nb	Al	Si	C	S
This study		7.95	57.45	21.25	7.86	1.65	3.4	0.29	0.14	0.008	0.00042
ASTM B805	Max	/	59.00	22.50	9.50	1.70	4.00	0.35	0.20	<0.03	<0.015
	Min	/	55.00	19.00	7.00	1.00	2.75	/	/	/	/

5.2.2 Optimization of process parameters of LPBF process for Alloy 725

All specimens were fabricated using a LPBF system (Print Genius 150, Prima Additive S.r.l., Italy) equipped with a 300 W ytterbium-fiber laser operating at a continuous wavelength of 1070 nm. The laser spot diameter was set to 100 µm. Fabrication was carried out under a high-purity argon with the oxygen level below 0.1%. The build plate was preheated to 80 °C. A stripe scanning strategy with a stripe width of 5 mm was adopted, combined with a 67° counterclockwise rotation. Before the production of specimens for test conducted in Chapther 5 and Chapther 6, a systematic experimental campaign was performed to optimize of the process parameters of LPBF for Alloy 725. Twenty different combinations of laser power and scan speed were investigated while keeping hatch spacing and layer thickness constant. Porosity, hardness, and surface roughness were measured to identify the

optimal processing parameters, as reported in Table 8. Further details about the research of LPBF techniques for Alloy 725 can be found in [189].

Table 8 - LPBF process parameters used for the design of experiments and relative material characteristics

Sample	Power	Scan speed	Porosity [%]	HV1	Sa [µm]
1	100	500	0.98	315	14
2	100	1000	1.62	309	15
3	100	1500	7.73	307	17
4	100	2000	6.05	239	16
5	150	500	0.03	327	9
6	150	1000	0.11	322	10
7	150	1500	0.51	306	16
8	150	2000	1.81	301	12
9	200	500	0.05	314	6
10	200	1000	0.04	310	9
11	200	1500	0.03	315	12
12	200	2000	0.19	318	11
13	250	500	0.29	328	6
14	250	1000	0.01	311	8
15	250	1500	0.01	316	9
16	250	2000	0.05	318	11
17	300	500	0.61	291	7
18	300	1000	0.13	322	8
19	300	1500	0.02	312	8
20	300	2000	0.02	317	11

5.2.3 Materials

The process optimization campaign revealed a broad and well-defined processing window capable to produce dense Alloy 725. Among the investigated conditions, the combination of 250 W laser power and 1000 mm/s scan speed was selected to produce new specimen to evaluate the mechanical properties and the corrosion behavior. The selected parameters fall within the center of the optimal

process window identified through Gaussian process regression, ensuring process stability and reproducibility to produce test specimens.

The specimens were fabricated with their longitudinal axis oriented horizontally with respect to the build platform, with the main faces parallel to the build plane, as schematically illustrated in Figure 31. The total height of the print was 20 mm to obtain sufficient material for subsequent specimen preparation. Subsequently, Half of the specimens were obtained from the building plane through wire electrical discharge machining (W-EDM). This cutting technique was selected to obtain the final specimen thickness of 5 mm while minimizing the introduction of mechanical stresses, plastic deformation, or thermal damage associated with conventional machining processes. half of the specimens were subjected to a precipitation-hardening heat treatment in accordance with ASTM B805 before the W-EDM cutting. The heat treatment consisted of a solution annealing step carried out at 1040 °C for 1 h, followed by water quenching, and a two-step aging treatment performed at 732 °C for 8 h, furnace cooling to 621 °C, holding for 8 h, and final air cooling.

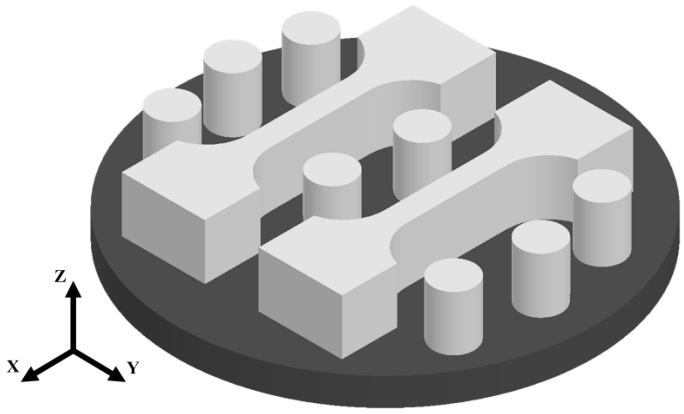

Figure 31 - program of the printing samples for mechanical and corrosion behaviors tests

The specimens fabricated were cylindrical, with a diameter of 15 mm and a height of 5 mm. These samples were produced for microstructural characterization, hardness measurements, porosity analysis, and corrosion-related testing. Tensile test specimens with a cross section of 5 × 8 mm and a gauge length of 36 mm were produced in accordance with UNI EN ISO 6892-1:2020. Two reference conditions of wrought Alloy 725 were included in the experimental campaign. The first condition corresponds to the as-forged material. For PH benchmark reference, specimens were extracted from a turbine blade previously analyzed in Chapther 3.

5.2.4 Microstructural analysis

Methodology and experimental equipment for metallographic analysis and microscopy investigation are the same reported in chapter 3.2.2 – materials and methods.

5.2.5 Hardness test

Rockwell C hardness measurements were performed in accordance with the UNI EN ISO 6508-1 standard. Tests were carried out on specimen surface polished with silicon carbide paper up to 1200 grit. For every condition considered has been conducted 5 measurements.

5.2.6 Tensile tests

A Galdabini Sun 5 universal testing machine with a 50 kN load cell was utilized for tension testing. The tests were conducted under quasi-static loading conditions, in displacement control, in accordance with the procedures of UNI EN ISO 6892-1:2020 standard. Evaluation of mechanical response included yield strength, ultimate tensile strength, and elongation to failure.

5.2.7 Electrochemical corrosion tests

The specimen preparation is compliant to 4.2.4 – electrochemical corrosion tests. Tests consisted in Open Circuit Potential (OCP) monitoring for 1 hour followed by electrochemical impedance spectroscopy (EIS) and potentiodynamics polarization tests carried out with Ivium CompactStat potentiostat.

The test solutions consisted of 0.6 M NaCl both near-neutral (pH 7) and acidic (pH 3, acidified with HCl) at 40 °C to evaluate the resistance against chloride ions and acidity. This solution was selected as it was found to be the most severe for Alloy 625 in Chapther 4. After the OCP, a sinusoidal perturbation with an amplitude of 10 mV was applied over a frequency range from 40,000 Hz to 0.01 Hz, acquiring five frequencies per decade for a total of 34 measured frequencies. Anodic potentiodynamic polarization tests were performed at a scan rate of 10 mV/min, starting from 10 mV below the OCP up to 1 V vs. SCE. The potential scan was then reversed until reaching 50 mV below the repassivation potential.

5.2.8 Intergranular corrosion test

Susceptibility to intergranular corrosion tests were performed in compliance to ASTM G28 standard method A and detailed information can be found in chapter 3.2.3 – Corrosion tests.

5.3 Results and discussion

5.3.1 Microstructural analysis

Metallographic analyses of Alloy 725 highlight the presence of distinct microstructures due to the manufacturing route and the eventual following heat treatment as visible in Figure 32. The LPBF process promotes the formation of unique microstructural features thanks to the extremely high cooling rates involved, which are fundamentally different from those produced by conventional technologies such as forging. In the forged condition, Alloy 725 exhibited a regular equiaxed grain structure with twins, whereas the LPBF-manufactured Alloy 725 exhibits a very fine dendritic-to-cellular microstructure. As shown in Figure 32C, metallographic etching also reveals the presence of melt pool boundaries and elongated grains grown in an epitaxial direction, characteristics that have already been widely reported in the literature for nickel-based superalloys processed by LPBF [11,144]. Following precipitation hardening, the forged alloy largely preserves its equiaxed grain with twins morphology; however, secondary phases tend to preferentially decorate the grain boundaries, reflecting diffusion-driven precipitation during aging. A similar evolution is observed in the LPBF-manufactured material after heat treatment, where the original solidification structure is partially replaced by recrystallized grains with annealing twins, accompanied by the formation of precipitates along grain boundaries.

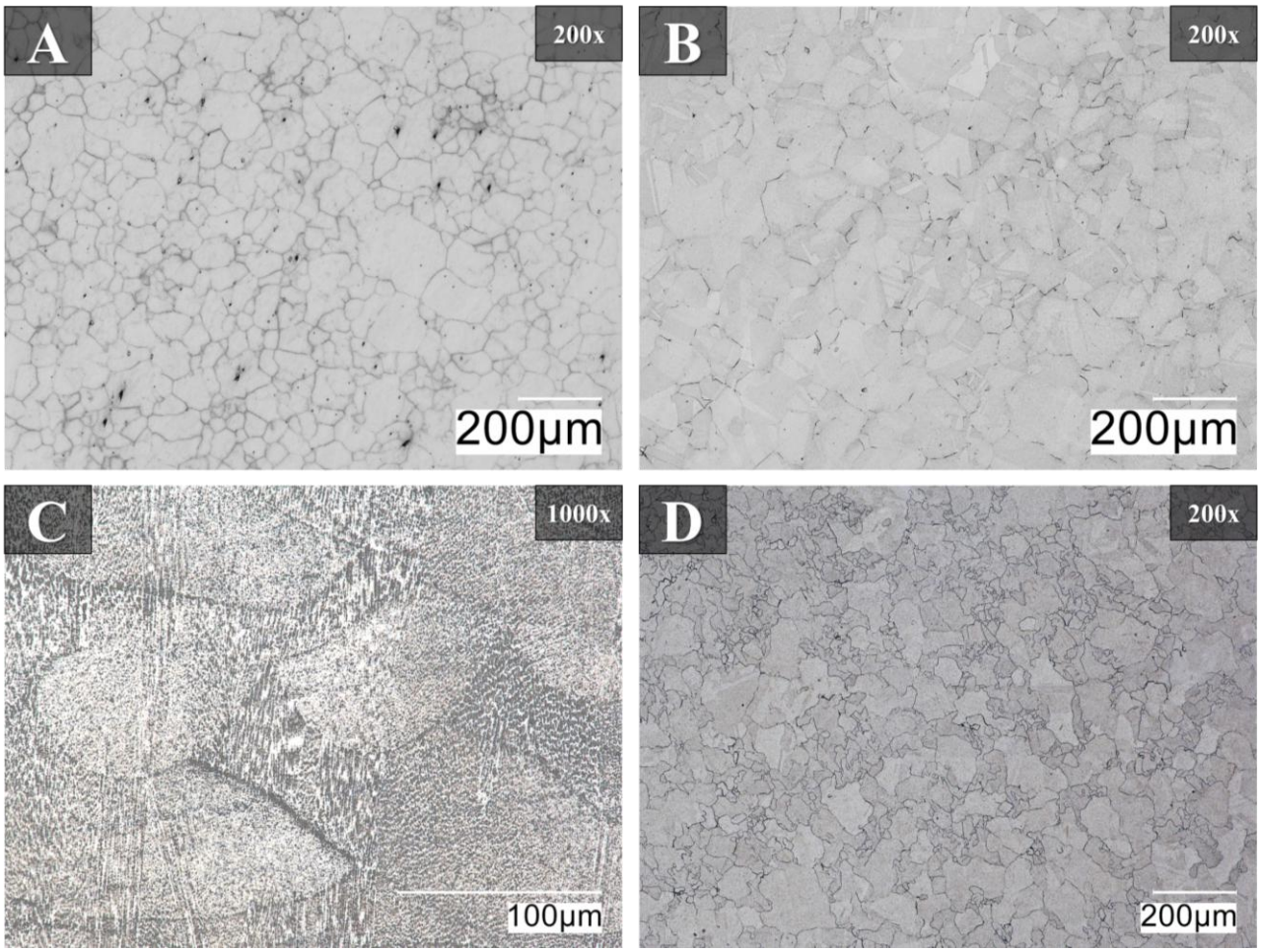

Figure 32 - Metallography at OM of Alloy 725 in different manufacturing and heat treatment conditions. A) Forged B) Forged and precipitation hardened C) LPBF D) LPBF and precipitation hardened

Alloy 725 is a precipitation-hardenable nickel-based superalloy whose material properties are strongly influenced by the formation, distribution, and morphology of secondary phases. Strengthening is primarily achieved through the aging treatment thanks to the precipitation of fine and homogeneously dispersed γ′ ($Ni_3(Al,Ti)$) phases [190]. Unlike Alloy 718, Alloy 725 has a lower niobium content that significantly reduces the tendency to form δ (Ni_3Nb) and Laves phases, which are detrimental for corrosion resistance. Nevertheless, prolonged or high-temperature aging treatments can still promote carbides, mainly the $M_{23}C_6$ and M_6C type, and other secondary precipitates at grain boundaries [142,191]. Iannuzzi and Hazarabedian [192] demonstrated that precipitation hardening in Alloy 725 promotes the formation of $M_{23}C$ carbides and F phase at grain boundaries, leading to sensitization and preferential crack propagation during hydrogen embrittlement. The precipitation of second phases is fundamental and must be a correct balance between mechanical strengthening and corrosion performance, particularly in aggressive environments where intergranular corrosion and environmentally assisted cracking may occur.

The forged Alloy 725 in the as-forged condition exhibits relatively uniform distribution of globular secondary phases within the matrix, as reported in EDS map in Figure 33A. Elemental mapping confirms that these precipitates are enriched in Nb, Mo and Ti. In contrast, the LPBF-manufactured alloy displays a dendritic to cellular microstructure without evidence of second phases detectable through FESEM analysis. In the forged alloy, precipitation hardening results in an equiaxed austenitic grain structure with secondary precipitates at the grain boundaries. In addition, there are titanium nitrides, previously discussed in 3.3.2. Conversely, the LPBF material undergoes partial recrystallization during precipitation hardening, leading to the formation of new austenitic grains that are predominantly elongated in the epitaxially direction. At the same time, intergranular precipitates become evident along grain boundaries, indicating that the heat treatment promotes both microstructural recovery and grain boundary precipitation.

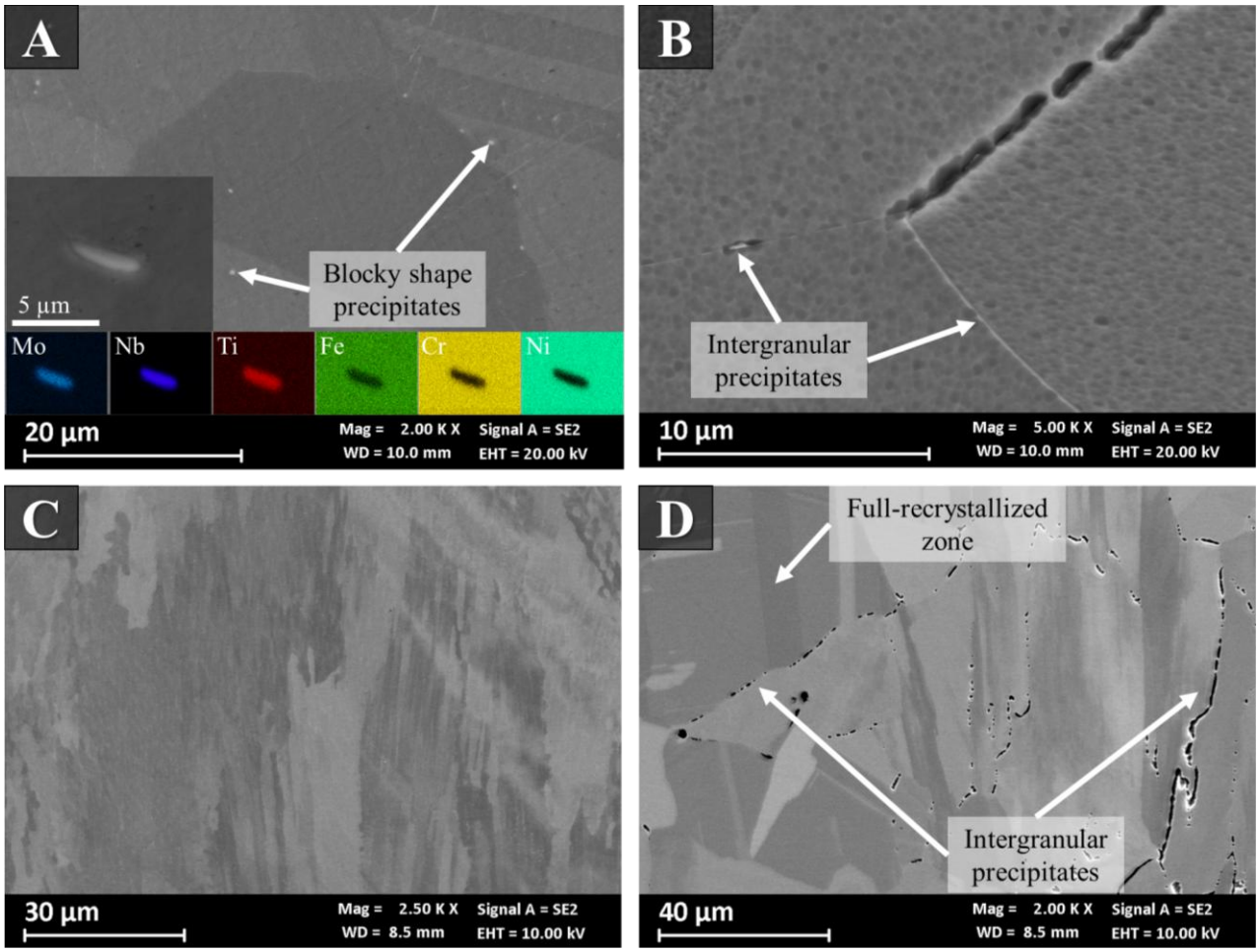

Figure 33 - FESEM micrographs of microstructure of Alloy 725 in different manufacturing and heat treatment conditions. A) Forged B) Forged and precipitation hardened C) LPBF D) LPBF and precipitation hardened

Although FESEM observations identified different secondary phases, X-ray diffraction analyses are dominated by peaks corresponding to the γ phase with FCC crystal structure, with the main peaks

indexed to the (111), (200), (220), and (311) crystallographic planes (Figure 34) [193]. No additional peaks attributable to secondary phases were detected within the sensitivity limits of the XRD technique. A difference in peak intensity was observed between additively manufactured specimens and the reference materials. In particular, the LPBF-produced Alloy 725, both in the as-built and precipitation-hardened conditions, exhibit a pronounced intensity of the (200) reflection. This preferential orientation in LPBF-manufactured nickel-based superalloys is directly related to the directional solidification conditions. After heat treatment, a reduction in the intensity of the (200) peak is observed, which can be attributed to a mitigation of the anisotropy associated with the columnar grain structure through partial recrystallization [144,194]. In contrast, the wrought Alloy 725 specimens, both in the as-forged and precipitation-hardened conditions, display a more isotropic diffraction pattern, consistent with an equiaxed grain structure.

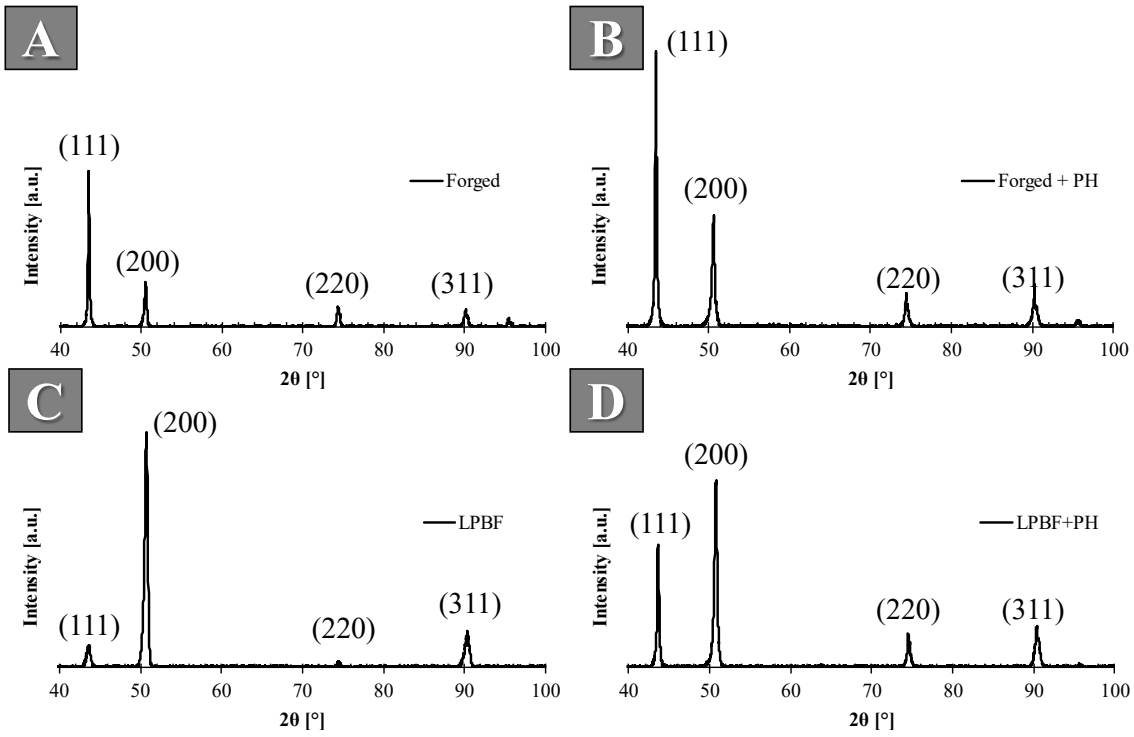

Figure 34 – XRD analysis of Alloy 725 in different conditions. A) Forged, B) Forrged + PH, C) LPBF and D) LPBF + PH

5.3.2 Mechanical behavior

Both heat treatment and manufacturing technology affected the Hardness values (Table 9). In the forged condition, the alloy exhibits low hardness value of about 28 HRC, consistent with Alloy 725 with no strengthening precipitates. A light higher hardness value is observed for the LPBF condition (31 HRC) thanks to the fine cellular-dendritic substructure. Nonetheless, the intrinsic strengthening

of LPBF microstructures is not comparable with the hardness increase through heat treatment for this alloy. In fact, the forged heat-treated condition reaches a hardness of 37 HRC, demonstrating the precipitation of fine and coherent γ′ in the material. Moreover, the LPBF heat-treated specimens exhibit the highest hardness value, reaching about 44 HRC. This enhanced response to heat treatment can be attributed to the combined effect of a more pronounced precipitation strengthening compared to the forged condition and the intrinsically fine microstructure produced by the LPBF process.

Table 9 - Hardness (HRC) of Alloy 725 for different processing and heat treatment conditions.

Condition	Solution annealing		First aging		Second aging		Hardness
	T [°C]	t [h]	T [°C]	t [h]	T [°C]	t [h]	HRC
Forged	\	\	\	\	\	\	28
Heat treated	1030	2	710	6	621	7	37
LPBF as-printed	\	\	\	\	\	\	31
LPBF heat treated	1030	1	732	8	621	8	44

In the as-printed condition, the alloy exhibits a yield strength of approximately 721 MPa and an ultimate tensile strength of about 1014 MPa, combined with a high elongation at fracture close to 36% (Table 10). This balanced combination of strength and ductility reflects the fine cellular-dendritic microstructure generated by the LPBF process. When compared with the minimum requirements specified by ASTM B805 for wrought Alloy 725, the LPBF-produced material significantly exceeds the standard limits for the solution-annealed condition. However, yield strength remain below the requirements for the precipitation-hardened condition. This behavior was expected and is consistent with the hardness measurements, which evidence that the primary strengthening of this material is obtained precipitation hardening. In fact, LPBF-manufactured specimens after the heat treatment reaches a yield strength of 1116 MPa and an ultimate tensile strength of 1407 MPa, corresponding to an increase about 50% in YS and 40% of UTS. This strengthening is accompanied by a reduction in elongation to about 27% due to the formation of γ′ precipitates that enhances resistance to plastic deformation at the expense of ductility. However, elongation values remained above the minimum values required PH condition following ASTM B805. This finding demonstrates that the LPBF route is capable of producing Alloy 725 components with mechanical properties completely compliant with those of traditional wrought products.

Table 10 - Tensile properties of LPBF-manufactured Alloy 725 and comparison with ASTM B805 standard.

Condition	Value	YS (MPa)	UTS (Mpa)	E (%)	Reference

LPBF as-printed	Mean	721	1014	35.9	This study
	Dev.Std.	2	2	0.8	
LPBF precipitation hardened	Mean	1116	1407	27.4	
	Dev.Std.	7	8	1.2	
Solution annealed	Min.	310	758	30	ASTM B805
Precipitation hardened	Min.	827	1137	25	

5.3.3 Susceptibility to selective corrosion

Nickel-chromium-molybdenum (NiCrMo) alloys may undergo selective corrosion due to local depletion of alloying elements responsible for passivation, mainly chromium and molybdenum, in the regions adjacent to grain boundaries [195–197]. This phenomenon is associated with the precipitation of secondary phases, such as M_6C, $M_{23}C$, MC and certain intermetallic [198,199]. The resulting condition is commonly referred to as sensitization and may develop when the alloy is exposed to temperature range between approximately 600 and 1100 °C depending on the alloy and its composition. Alloy 625 represents a well-documented example in this regard, owing to its widespread use in aggressive environments. Brown et Al. [199] investigated Alloy 625 annealed at different temperature to evaluate the susceptibility of this alloy through ASTM G28-A. The finding identified the temperature range between 700 and 950 °C to be detrimental for selective corrosion in Alloy 625 with increase of corrosion rates from 150 mdd to values exceeding 1000 mdd. Alloy 725 is a material derived from Alloy 625, developed by additions of aluminum and titanium to enable age hardening while preserving the excellent corrosion resistance characteristic of Alloy 625 [138]. Although Alloy 725 is not explicitly included among the materials listed in the ASTM G28 standard, the test assesses if secondary phases precipitated during heat treatment could be deleterious to its resistance to selective corrosion. The results of the ASTM G28-A intergranular corrosion tests are summarized in Table 11. In the forged condition, the alloy exhibits a relatively low corrosion rate (155 mdd), comparable to that reported for non-sensitized Alloy 625. A moderate increase is observed for the LPBF-processed material in the as-built condition (376 mdd), which can be attributed to the finer microstructural features and possible microsegregation associated with the rapid solidification of melt pools. Consistent with this interpretation, several studies on Ni–Cr–Mo alloys have reported that heat-affected zones (HAZ) in welded components exhibit an increased susceptibility to intergranular corrosion due to microsegregation and precipitation phenomena induced by localized

thermal cycles [195,196,198]. Nevertheless, the substantial increase in corrosion rate is observed after precipitation hardening for both manufacturing processes. The forged precipitation-hardened condition shows 1890 mdd, while the LPBF precipitation-hardened alloy exhibits the highest values, exceeding 3000 mdd. These results clearly indicate that precipitation hardening promotes a sensitized condition.

Table 11 - Corrosion rates of Alloy 725 after ASTM G28-A

Conditon	**Corrosion rate [mdd]**		**Corrosion rate [mm/y]**	
	Mean	Dev.Std.	Mean	Dev.Std.
Forged	155	12.1	0.68	0.05
Forged + PH	1890	35.2	8.30	0.15
LPBF	376	24.3	1.65	0.11
LPBF + PH	3113	52.0	13.67	0.23

Cross section provide insight into the corrosion morphology developed during the test conducted Figure 35. In the untreated condition, both forged and LPBF, the corrosion attack remains relatively uniform, with shallow penetration and no clear preferential path, in agreement with the low corrosion rates measured for these conditions. After precipitation hardening, a marked change in corrosion morphology is observed in the forged alloy. The attack morphology evidences deep selective penetrating features. Several penetrating attacks exhibit a straight-line morphology, suggesting that corrosion paths follow annealing twins rather than only grain boundary. Conversely, the LPBF precipitation-hardened condition has a distinct corrosion morphology. Although selective attacks are still present, they are generally less deep than those observed in the forged counterpart. This behavior may indicate a different distribution of secondary phases formed during precipitation hardening. Despite the reduced penetration depth of individual attacks, the overall corrosion rate measured for the LPBF precipitation-hardened condition remains higher. This suggests that corrosion is more uniformly distributed over the exposed surface, rather than concentrated in a limited number of deeply penetrating sites. Such behavior is consistent with the presence of a higher density of finely dispersed secondary phases and locally alloy-depleted regions, which can promote widespread micro-galvanic coupling within the material [200].

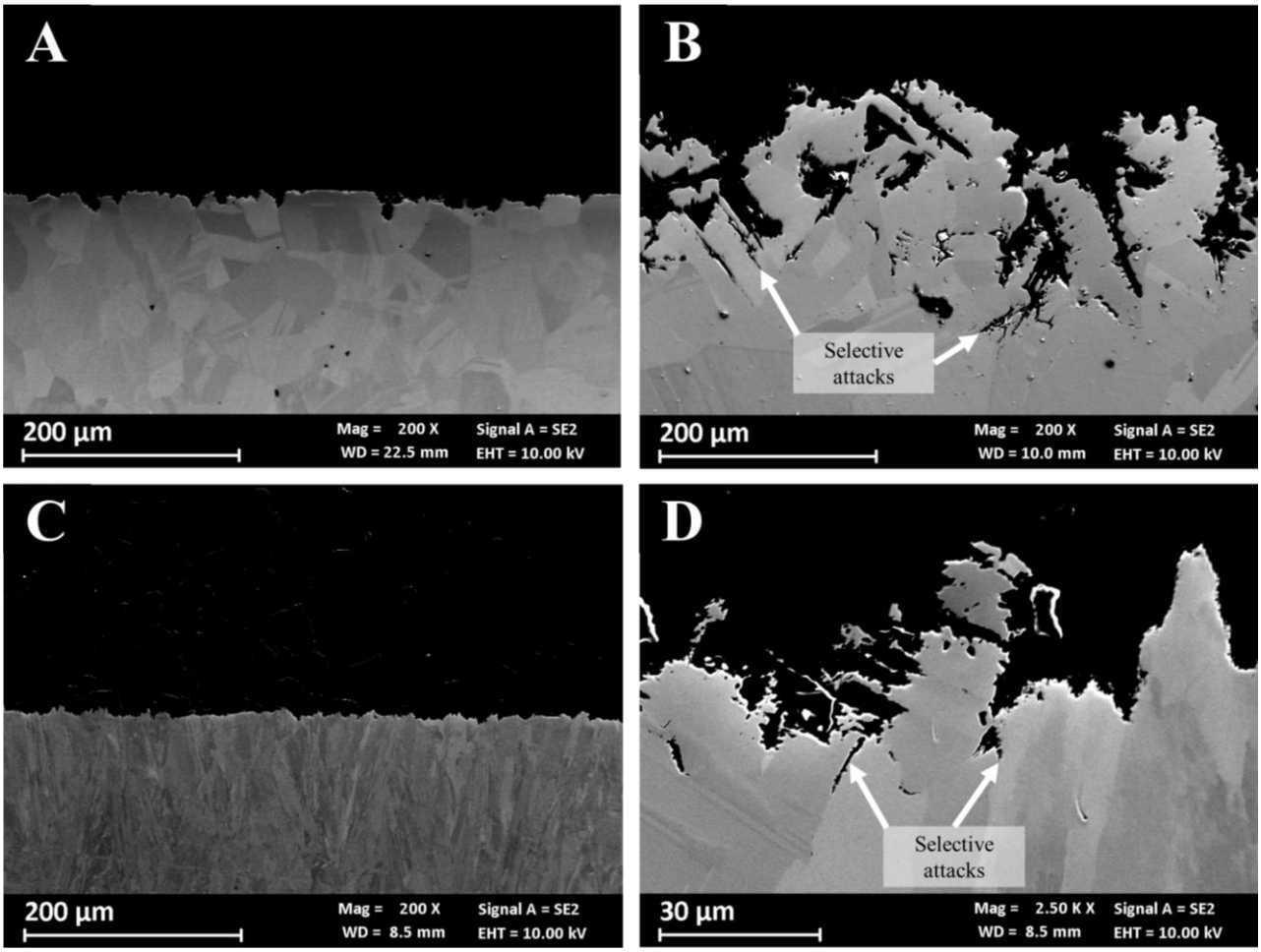

Figure 35 – FESEM cross-section micrographs of Alloy 725 specimens after ASTM G28A intergranular corrosion testing in different manufacturing and heat treatment conditions.

5.3.4 Corrosion behaviors in chloride acidic environments

Electrochemical impedance spectroscopy (EIS) is a useful tool for investigating the properties of passive oxide films formed on metallic materials in the considered environment. The Bode plots measured at OCP in 0.6 M NaCl acidified to pH 3 at 40 °C are reported in Figure 36. The results indicate an excellent and comparable corrosion response for every condition evaluated. At high frequencies, the impedance modulus reaches a well-defined plateau, which is associated with the electrical resistance of the surface film formed on the tested specimens. Impedance values are between 10^5 and 10^6 $\Omega \cdot cm^2$ were measured, indicating the formation of a compact and protective passive film. Slight differences can be observed between precipitation-hardened and non-heat-treated specimens in the phase angle response around 10^{-2} Hz frequencies. This behavior suggests the presence of an additional time constant related to a charge-transfer process, which is likely associated with differences in passive film stability and interfacial processes induced by the heat treatment.

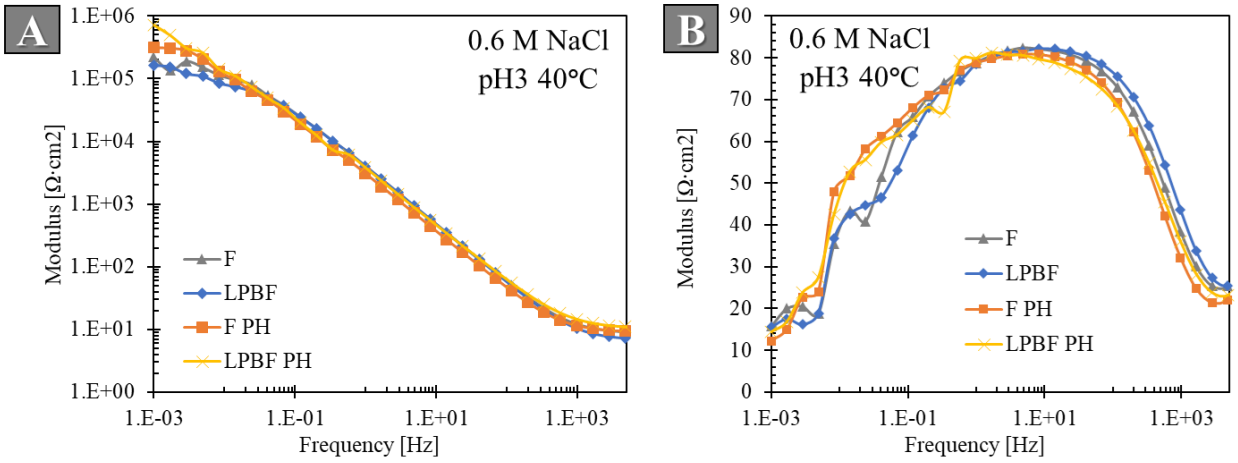

Figure 36 - The Bode plots for passive films of Alloy 725 in 0.6 M NaCl acidified to pH 3 at 40 °C

The potentiodynamic polarization curves revealed an excellent passive behavior for all the investigated conditions (Figure 37). These results, in agreement with the EIS measurements, confirm the formation of a stable and protective oxide film on Alloy 725 in acidic chloride-containing environments, regardless of the manufacturing techniques or heat treatment. The polarization curves are characterized by an extended passive region. The breakdown potential is associated with the formation of CrO_4^{2-} species as test conducted on Alloy 625 present in section 4.3.5. There are no rapid current increase during the passive region indicating an excellent resistance to localized corrosion. This interpretation is further supported by the reverse scan, which exhibits no hysteresis, indicating the absence of pit stabilization and confirming the reversible nature of passive film breakdown.

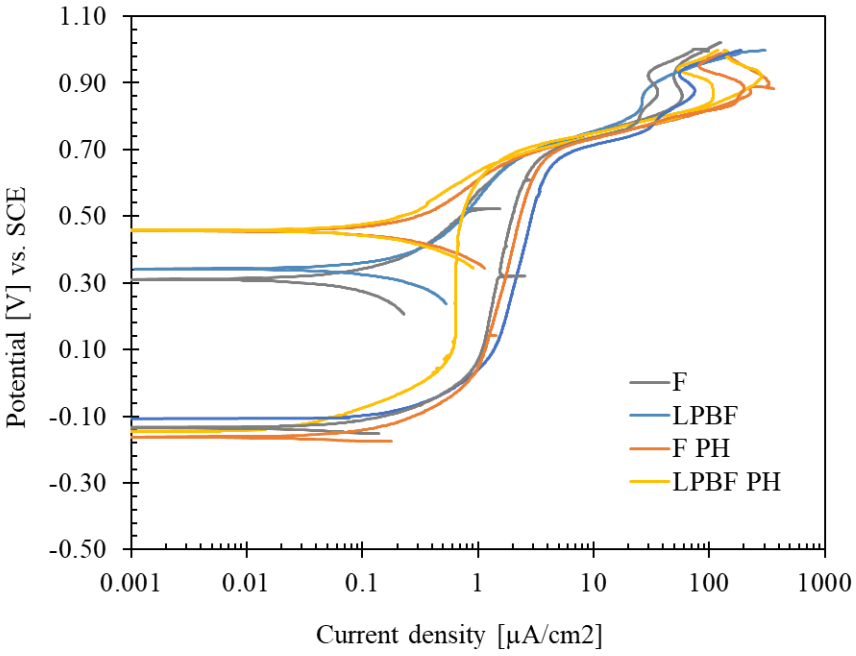

Figure 37 – Potentiodynamics polarization test of Alloy 725 in 0.6 M NaCl acidified to pH 3 at 40 °C

5.4 Conclusion

This study characterized the microstructure and material properties of a novel alloy produced via AM starting from end-of-life components. Alloy 725 manufactured by LPBF exhibits the typical melt pool features associated with this technology. Its microstructure is characterized by epitaxial columnar grains with cellular and dendritic substructures, which provide excellent mechanical properties compared to the wrought Alloy 725.

Despite its good strength and ductility observed in the as-printed condition, the strengthening of Alloy 725 is primarily achieved through precipitation hardening rather than through solid-solution or microstructural refinement. Following heat treatment, the LPBF-manufactured alloy undergoes partial recrystallization and exhibits excellent hardening response, leading to mechanical properties that significantly exceed the minimum requirements for ASTM B805 while maintaining adequate elongation at fracture.

The unique microstructure generated by the LPBF process also influences the susceptibility of Alloy 725 to selective corrosion. Both in the as-printed and precipitation-hardened conditions, Alloy 725 exhibits higher corrosion rates compared to its forged counterpart. Nevertheless, a clearly sensitized condition is observed only after precipitation hardening, which leads to a significant increase in corrosion rate for both forged and LPBF-produced materials.

Electrochemical investigations confirmed the formation of a stable and protective passive film for all investigated conditions in acidic chloride-containing environments. Both EIS and potentiodynamic polarization measurements revealed that LPBF process produce an Alloy 725 with comparable corrosion behavior in acidic chloride solution of conventionally manufactured material.

Overall, the characterization of Alloy 725 demonstrates that the recovery of specialty nickel-based alloys from end-of-life components is a feasible strategy to produce new high-performance materials via AM. The LPBF route enables the fabrication of Alloy 725 with outstanding mechanical properties and corrosion behavior comparable to conventionally manufactured material. These results highlight the feasibility of material recovery through AM to create closed material loops of advanced alloys in demanding industrial applications.

Chapther 6. Field exposure test of super nickel alloys obtained by means of AM

6.1 Chapter introduction

Laboratory corrosion testing provides fundamental insight into material behavior and into how different manufacturing technologies may influence degradation mechanisms. Reproducing fully service-relevant conditions in controlled laboratory settings is a challenge due to the combination of a steam rich in chemically aggressive species, elevated temperatures and high pressures. It is necessary to conduct exposure tests using real geothermal steam. These tests enable the direct evaluation of degradation mechanisms under realistic operating conditions typical of direct-cycle geothermal power plants.

This chapter presents the results of exposure tests performed in a chamber operated by Enel Green Power and directly fed with steam extracted from a geothermal well. The investigation focuses on nickel-based alloys as promising candidates for geothermal turbine blade applications. Based on the results obtained in the previous chapters, Alloy 725 produced by LPBF in both the as-printed and precipitation-hardened conditions, as well as Alloy 625 produced by DED for potential turbine blade cladding applications, were selected for testing in the exposure chamber. Among the materials tested by Enel Green Power, conventionally manufactured Alloy 725 and a supermartensitic stainless steel, known to be susceptible to stress corrosion cracking under these environmental conditions, were considered as reference materials.

The findings demonstrate the suitability of additively manufactured nickel-based superalloys for geothermal applications and provide a basis for integrating new, more sustainable manufacturing approaches in the geothermal sector, including material recovery strategies and laser-based repair and cladding technologies.

6.2 Materials and methods

6.2.1 Test chamber and exposure conditions

The test chamber is powered by steam extracted from geothermal power plant “Selva 4” operated by Enel Green Power S.p.A. (Larderello, Italy). A regulation and monitoring section of temperature and pressure allow to reproduce dew-point conditions representative of the most aggressive operating zones encountered in direct-cycle geothermal turbines. The geothermal steam used in the tests is

endogenous and unwashed, ensuring realistic chemical conditions. Prior to material qualification tests, a preliminary assessment of exposure homogeneity was performed using carbon steel cylindrical specimens without sharp edges.

The exposure started on 27 July 2025 and continued uninterrupted until 9 September 2025, for a total duration of 1032 hours. At the beginning of the test, the operating parameters inside the chamber were 161-166 °C at the specimen plate, a pressure of 6.5 bar, and a steam flow rate of 0.32 t/h, with an estimated steam fraction of 4.3%. These values were taken as the reference operating conditions. Throughout the test, temperature and pressure were continuously monitored. Until 25 August 2025, the chamber operated with temperatures generally between 140 and 165 °C and pressures between 4 and 7 bar. In the subsequent period, the operating conditions stabilized at lower values, with temperatures of 120-130 °C and pressures of 2.5-2.7 bar.

6.2.2 Materials, specimens and microscopy analysis

The materials investigated in this study include nickel-based superalloys produced through different manufacturing routes and discussed in the previous chapters. Alloy 725 was produced by LPBF and investigated both in the as built and precipitation hardened condition. To evaluate the potential influence of microstructure on SCC resistance, Alloy 725 U-bend specimens were manufactured with orientations along the vertical (XZ) and horizontal (XY) build directions. Alloy 625 was produced by DED and tested in the as built condition. As a benchmark material is considered a conventionally manufactured wrought Alloy 725 to establish if super nickel alloys produced with advanced technologies have a comparable corrosion behavior. Further details of materials used for this test can be found in section 615.2.1. To ensure the harshness of the environment through the test a martensitic stainless steel grade X5CrNiMo12-6-1.5 were included which is known to be susceptible of pitting and SCC in DWP condition of geothermal vapors.

Table 12 – summary table of materials

Material	Type	N°	Condition	Heat treatment
X5CrNiMo12-6-1.5 (S41425)	Crevice specimen	1	/	Quenched and tempered
	U-bend	2	/	Quenched and tempered
Alloy 725	Crevice specimen	3	/	Precipitation hardened
	U-bend	4	/	Precipitation hardened
Alloy 725 LPBF	Crevice specimen	5	XY	/
	Crevice specimen	6	XY	Precipitation hardened
	U-bend	7	XY	/
	U-bend	8	XY	Precipitation hardened
	U-bend	9	XZ	/

	U-bend	10	XZ	Precipitation hardened
Alloy 625 DED	Crevice specimen	11	XY	/
	U-bend	12	XY	/

Two main specimen geometries were employed for evaluate the corrosion rate and morphology, crevice resistance and susceptibility to SCC. Flat plate specimens (Crevice specimens) with dimensions of 50 × 50 × 3 mm were used to evaluate corrosion morphology and localized corrosion behavior. In fact, these specimens were coupled with crevice formers and assembled in accordance ASTM G78 standard (Figure 38A). The crevice formers are assembled to generate a circular array of sectors, producing well-defined occluded regions that act as preferential sites for crevice corrosion initiation. Specimens to investigate SCC were developed following U-bend type B in according to ASTM G30 and mounted as reported in Figure 38B. All specimens were grinded up to 1200 grit with SiC papers, cleaned and weighed.

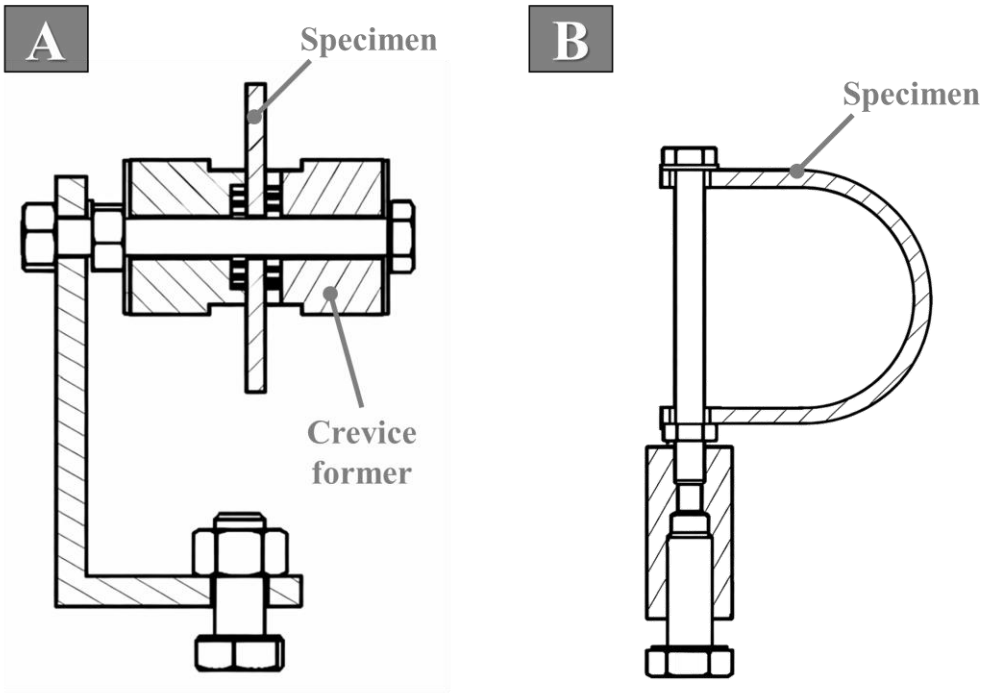

Figure 38 - Assembly diagram of the A) Crevice and B) U-bend specimens on the plate

After field exposure test all the specimens followed a sequential procedure based on ASTM G1 to clean the specimens. The cleaning method consisted of successive surface cleaning steps. An initial mechanical cleaning by brushing was carried out to remove the coarsest deposits from the specimen surfaces, after which a first weighing was performed. This was followed by successive pickling cycles in accordance with ASTM G1, consisting of acetone cleaning, drying, immersion in hydrochloric acid with hexamethylenetetramine for 10 minutes, rinsing in water combined with mechanical cleaning

using a plastic brush or scraper, subsequent acetone cleaning, and final drying. Surface morphology and cross sections were then investigated by Keyence VHX-7100 digital optical microscope optical microscopy and Zeiss Gemini Sigma 300 field emission scanning electron microscope, with particular attention to under-deposit attack and crevice corrosion.

6.3 Results and discussion

After the test, all specimens were covered by a thin layer of deposits formed by the condensation of geothermal steam, as reported in Figure 39. Such deposits were observed also on non-metallic elements (Figure 26), such as the crevice formers, thereby confirming their predominant origin from the condensation of geothermal steam vapors instead of corrosion products [31].

Figure 39 - Specimen plate with mounted samples after the field exposure test

The investigated specimens exhibited an increase in mass at the end of the field exposure test. The cleaning treatments were not effective in removing the deposits, providing further evidence that they consisted of scaling. The removal of the deposit was achieved through mechanical cleaning; however, the specimen mass remained slightly higher than the initial value, indicating that the material did not undergo significant degradation during the exposure test. The slight mass increase observed in some specimens is attributed to the presence of persistent deposit residues that were not completely removed during chemical cleaning. Further pickling was deliberately avoided to prevent alteration of the surface corrosion morphology. As expected, an exception was represented by X5CrNiMo12-6-1.5, which exhibited significant mass loss (Table 13). The corrosion rate of X5CrNiMo12-6-1.5 was estimated to be slightly below one millimeter per year, representing a substantial material degradation

rate. This behavior indicates the inability of this material to form and maintain a stable passive film under the tested geothermal conditions.

Table 13 - Summary table of mass loss measurements

Material	Type	N°	Initial weight [g]	Final weight [g]	Corrosion rate [mm/y]
X5CrNiMo12-6-1.5 (S41425)	Crevice specimen	1	55,4175	50,9885	0.88
	U-bend	2	17,0109	-	Fractured
Alloy 725	Crevice specimen	3	57,1910	57,2338	Undetectable
	U-bend	4	19,0563	19,2637	Undetectable
Alloy 725 LPBF	Crevice specimen	5	52,2491	52,4994	Undetectable
	Crevice specimen	6	52,7731	53,0114	Undetectable
	U-bend	7	18,5077	18,6501	Undetectable
	U-bend	8	17,8115	17,8755	Undetectable
	U-bend	9	19,5809	19,9556	Undetectable
	U-bend	10	16,5300	16,5341	Undetectable
Alloy 625 DED	Crevice specimen	11	47,7866	47,9804	Undetectable
	U-bend	12	21,2215	21,4277	Undetectable

Indeed, the crevice specimen made of X5CrNiMo12-6-1.5 exhibits corrosion over the entire surface exposed outside the covered area. The attack morphology is highly heterogeneous, and cross-sectional observations reveal the presence of semi-spherical corrosion features penetrating into the material (Figure 40). No crevice corrosion was observed in the area shielded by the crevice former.

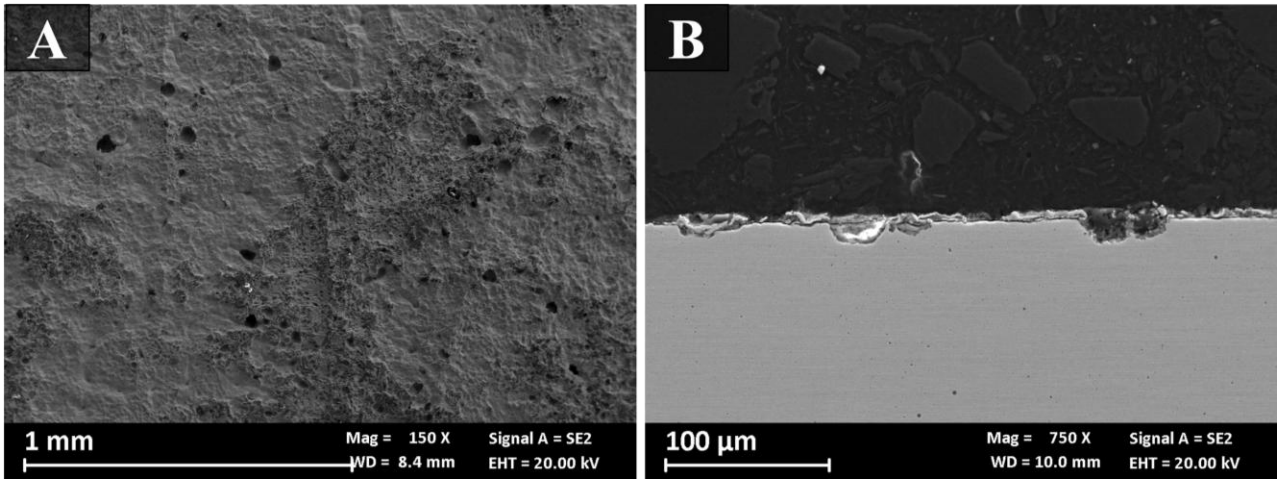

Figure 40 - FESEM micrography of Crevice specimen in X5CrNiMo12-6-1.5. A) Surface image after cleaning B) Cross section

In Alloy 725 and Alloy 625, no evidence of crevice corrosion beneath the crevice former sectors was observed, either for the wrought specimens or for the LPBF variants. This result is of fundamental importance, as it demonstrates that these materials exhibited resistance to crevice corrosion under the tested geothermal conditions. However, on the specimen surfaces, a few locations showing slight

under-deposit corrosion were observed under all the experimental conditions investigated. The detected attacks were very limited and did not compromise the integrity of the specimens (Figure 41). These features did not result in measurable section loss and were associated with largely intact passive films. Moreover, under-deposit corrosion was also observed on the conventionally produced Alloy 725 currently adopted for actual service turbine blade, indicating that this phenomenon is not specific to additively manufactured materials.

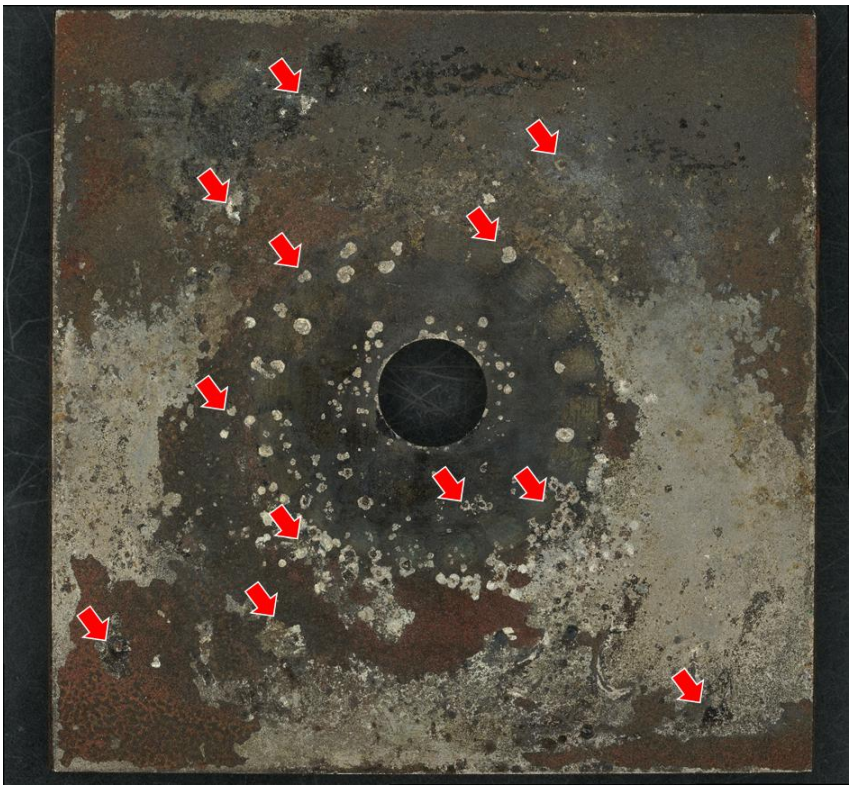

Figure 41 - Digital optical image of crevice specimen made of Alloy 725 produced by forging and precipitation hardened. Red arrows underline under-deposit corrosion.

Further FESEM examination of the surface morphology (Figure 42) provided additional insight into the under-deposit attack observed on super nickel alloys. The morphology of these anodic regions underlined the microstructure. In the LPBF-manufactured Alloy 725, localized dissolution highlighted a fine cellular subgrain texture, whereas in the heat-treated material (both LPBF and forged) the attack occurred preferentially along grain boundaries, in agreement with the intergranular corrosion behavior observed in laboratory testing. For Alloy 625 produced by DED, interdendritic region are visible inside the anodic region are that is consistent with the solidification microstructure typical of the deposition process.

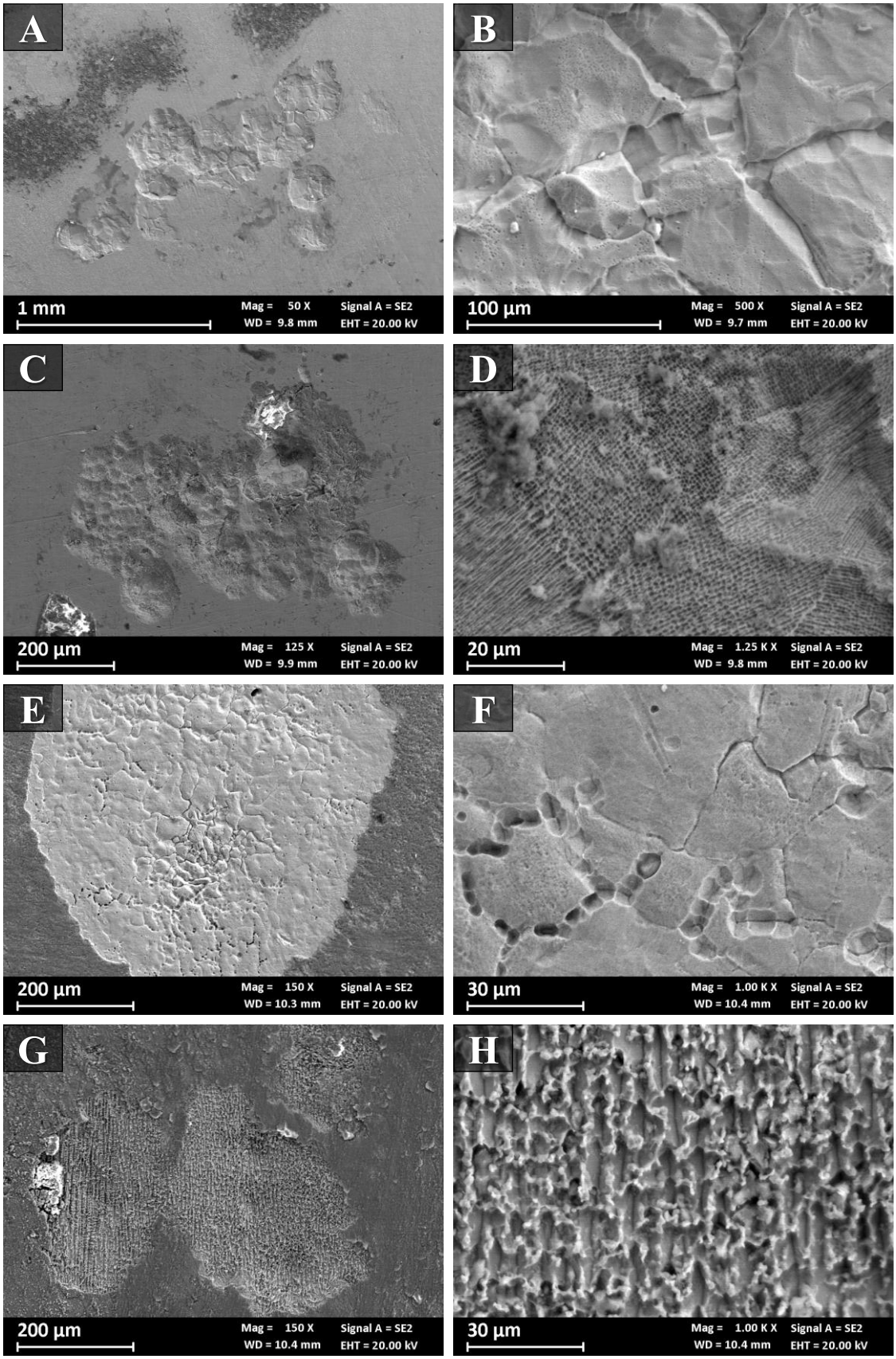

Figure 42 - FESEM image of under-deposit corrosion of A), B) Alloy 725, C), D) Alloy 725 LPBF, E), F) Alloy 725 LPBF PH and G), H) Alloy 625 DED.

In both alloys, however, the dissolution remained very shallow and non-propagating as visible in Figure 43. The absence subsurface penetration fronts confirms that the observed morphology is consistent with superficial dissolution rather than true pitting corrosion.

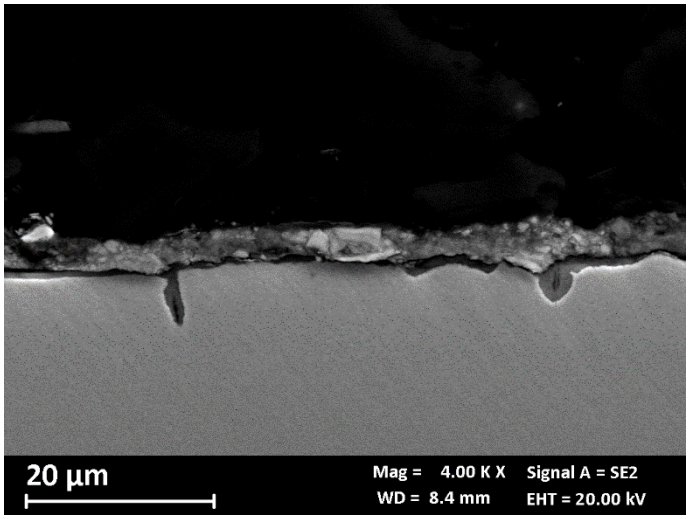

Figure 43 - Cross section of crevice specimen in Alloy 725 produced by LPBF and precipitation hardened

The test results of U-bend specimens confirmed the critical role of environmental conditions in promoting stress corrosion cracking in martensitic stainless steels with nickel contents close to 6%, as demonstrated by the failure of U-bend specimen made of X5CrNiMo12-6-1.5 [25]. The specimens exhibit an extensive presence of branched transverse cracks that are typical of SCC (Figure 44). Moreover, numerous localized attacks are also clear demonstrating the effectiveness of the test conducted. Conversely, no failures or cracks were detected in any of the Alloy 625 and Alloy 725 specimens, whether produced by conventional routes or by AM techniques.

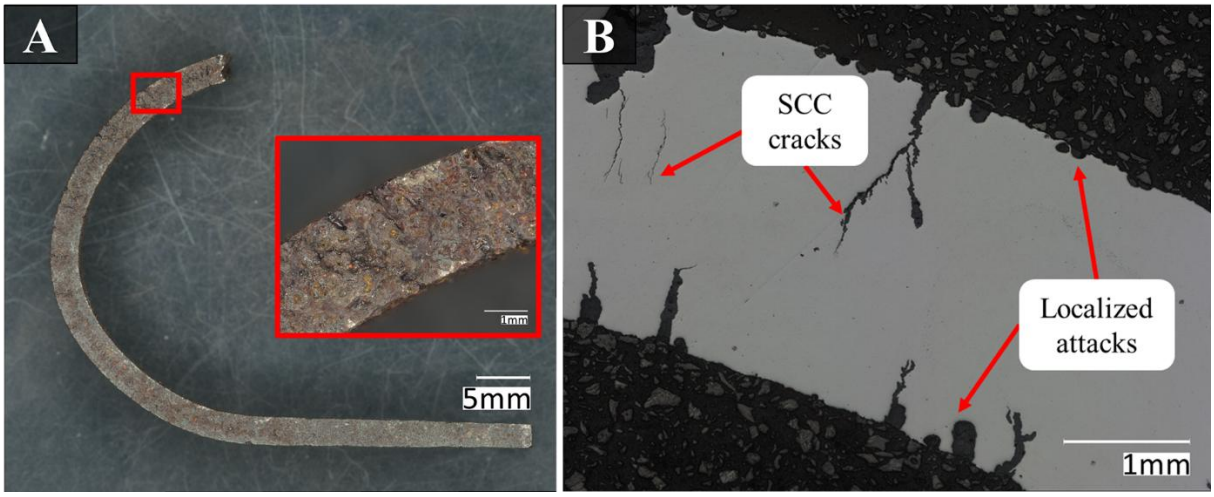

Figure 44 - U-bend in X5CrNiMo12-6-1.5 after the exposure test. A) OM micrograph B) Cross section

6.4 Conclusion

Exposure tests conducted in a geothermal steam test chamber operated by Enel Green Power provided valuable insight into the corrosion behavior of nickel-based alloys under real service-relevant conditions.

The occurrence of stress corrosion cracking on the X5 alloy demonstrates the effectiveness of the test in reproducing incipient condensation conditions within the exposure chamber. Findings regarding nickel superalloys are fully consistent with the trends observed in laboratory corrosion testing discussed in previous chapters. Alloy 725 demonstrated excellent resistance to corrosion with no occurrence of crevice and SCC, both in its conventionally manufactured form and when produced via LPBF, confirming its suitability for geothermal turbine applications. Alloy 625 also showed favorable corrosion behavior and comparable to the Alloy 725.

This work lays the groundwork for the integration of advanced manufacturing technologies within the geothermal sector. In this context, Alloy 625 produced by DED has proven to be a viable solution for laser-based repair and cladding of geothermal turbine components, offering an effective strategy for component repair and surface protection.

In addition, the exposure tests performed on Alloy 725 demonstrate that represents a suitable material for geothermal environments. This enables closed-loop material cycles, which can reuse end-of-life components and promote more sustainable material management strategies within geothermal power plants.

Chapther 7. Case study II: degradation of titanium alloys in geothermal environments

7.1 Chapter introduction

Titanium and its alloys are widely employed in the geothermal sector because of their excellent corrosion resistance; however, their use requires careful assessment to ensure compatibility with the specific chemical and thermodynamic conditions of the service environment [32,36].

A lot of contribution on literature is available on the corrosion behavior of titanium alloys, including the development of advanced grades specifically designed to enhance resistance in acidic and reducing environments or to mitigate hydrogen-related degradation mechanisms [73,75,201–206]. In line with these studies, corrosion-enhanced titanium alloys are increasingly adopted in the geothermal sector, particularly for components exposed to aggressive fluids [207–209].

Despite this extensive scientific background, the open literature contains only limited case studies addressing the failure of titanium operating in geothermal systems [210]. In particular, documented failures occurring under real in-service operating conditions remain scarce.

This work presents a case of a titanium Grade 2 tube of a geothermal heat exchanger, where a hydrogen embrittlement phenomenon led to the failure of the component during service. The study reports the fracture case demonstrating that the cause of fracture is HE with different techniques, that allowed to suppose the mechanism of fracture. This study shows that the use of Grade 2 titanium in geothermal wells may pose a risk and should only be considered after detailed assessment of material compatibility with the expected service conditions.

7.2 Materials and methods

7.2.1 Material

The case of this failure analysis is a commercially pure titanium Grade 2 in according with ASTM B338 (UNS R50400) tube extracted from a shell-and-tube heat exchanger operating in the geothermal plant of Amiata Energia. The tube with an outer diameter of 18 mm and a wall thickness of 0.9 mm exhibited a fracture extending axially for approximately 150 mm, with two branching zones at the extremities. One of these extremities shows significant plastic deformation (Figure 45), resulting from the mechanical removal of the damaged section.

Figure 45- Heat exchanger tube along the fracture a) Reconstruction of the entire fracture using digital optical microscope b), c) Details

The exchanger operates with superheated steam produced at the Bagnore 3 geothermal well flowing inside the tubes at mean temperature of 190°C and an inlet pressure of approximately 12 bar. Outside the tube bundle geothermal waters is heated and destined for the S. Fiora district-heating network, typically leaving the exchanger at 93 °C with operating pressures varying seasonally between 5.5 and 7 bar. Chemical analysis of steam and water of the heat exchanger has been measured in field and laboratory (Table 14). Water treatment involves an oxygen scavenger and an alkalizing agent.

Table 14 - Chemical analysis of steam condensation and liquid (water in the shell) of the heat exchanger

Type	Analysis	Unit	Bagnore condensation	Bagnore liquid
Field analysis	Gas/Vap	(Nl/Kg)	43,79	***
	T	(°C)	12,33	25,67
	pH		8,06	7,81
	Cond.	(µS/cm)	9300,00	4293,33
	Alc.	(meq/l HCl)	100,30	18,48
	Alc. Rit	(mg/l)	***	8,07
	H2S	(mg/l)	566,67	39,07
Laboratory analysis	pH		7,88	7,93
	Cond.	(µS/cm)	9994,33	4018,00
	Alc.	Meq/HCl	100,55	18,37
	Alc rit.	Meq/HCl	93,41	10,91

Na	mg/l	***	300,33
K	mg/l	***	92,27
Ca	mg/l	***	1,57
Mg	mg/l	***	0,04
Cl^-	mg/l	46,23	731,00
SiO_4^{2-}	mg/l	***	7,50
SiO_2 tot	mg/l	***	783,67
SiO_2 mono	mg/l	***	772,00
H_3BO_3	mg/l	481,63	7117,33
$NH4^+$	mg/l	1742,67	335,00
Li	mg/l	***	6,48
Rb	mg/l	***	1,21
Cs	mg/l	***	0,50
Sr	mg/l	***	0,02
Sb	mg/l	***	25,77
As	mg/l	***	12,56
Hg	mg/l	***	0,02
Al	mg/l	***	0,94
Fe	mg/l	***	0,03
F^-	mg/l	***	6,87
Br^-	mg/l	***	2,30

The tube sheet was made of forged AISI 316L stainless steel, while the shell consisted of high-strength fine-grain steel suitable for pressure equipment, as represented in Figure 46.

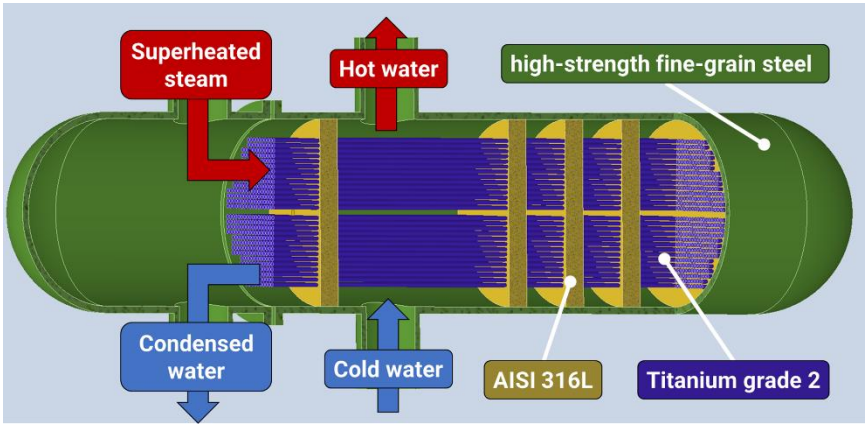

Figure 46- Simplified diagram of the heat exchanger

The unit provides a heat-transfer surface of 205 m² and a thermal power of 8593 kW. The heat exchanger, manufactured in 2003, operated alternately with another exchanger installed in series. Before each recommissioning cycle, the unit underwent visual inspections, as well as the initial hydrostatic pressure tests (45.2 bar on the tube side and 24 bar on the shell side) for twelve hours with positive results. Between 2010 and 2012, fractures were detected in several tubes, which were subsequently removed from service. The tube analyzed in this study was sampled following a rupture that occurred in 2024 during the scheduled leak test before a new service cycle. Chemical analysis has been carried out after the extraction of the ex-service tube and are presented in Table 15.

Table 15 - Chemical composition of tube after the service

Element	Ti	Fe	O	C	N
ASTM B338	Balance	≤ 0.3	≤ 0.25	≤ 0.08	≤ 0.03
Base metal	Balance	0.056	0.17	0.012	0.021
Weld beam	Balance	0.055	0.16	0.038	0.015

7.2.2 Microscopic analysis

Methodology and experimental equipment for metallographic analysis and microscopy investigation are the same reported in chapter 3.2.2 – materials and methods, except for metallographic reagent.
The titanium tube was mechanically cut to investigate the cross section and for metallographic purpose. Kroll's reagent (3 mL HF, 6 mL HNO_3, H_2O to 1000 mL) was used to reveal the microstructure, while Lactic hydride reagent (100 mL lactic acid, 3 mL HF, 97 mL HNO_3) was applied to assess the distribution of hydrides [211].

7.2.3 Hardness testing

Knoop hardness test was assessed by means of a UHL VMHT microhardness tester, set to apply a load of 10 g for 15 s. A minimum of 15 indentations per sample were performed. The hardness tests were performed on the cross section of the tube. The 84 measurements were conducted along 4 rows along the radial direction of the tube.

7.2.4 Hydrogen content analysis

The analyses were performed using a LECO ONH836 analyzer at 2200°C. The determination of the analysis was carried out using a comparator at a 1% (percentage of the sample peak at which the analysis terminates). The calibration has been made using titanium-tin caps with 17 ppm of hydrogen for 90 second at 2200°C. A total of 10 specimens were extracted from a region adjacent to the fracture, with half taken from the fusion zone (FZ) and half from the unaffected base material (BM). The specimens, weighing between 0.08 and 0.2 g, were obtained using Electrical Discharge Machining (EDM) to minimize material alteration. Subsequently, the specimens were polished using 1200-grit abrasive paper to remove corrosion products and the oxide layer formed during the EDM process. The samples were then rinsed with distilled water and cleaned in ultrasonic bath in acetone to ensure surface purity. Specimens extracted from a Grade 2 titanium sheet were used as reference.

7.3 Results and discussion

7.3.1 Tube condition

The tube exhibits a complex fracture morphology in the proximity of the weld that can be divided into three distinct characteristic zones, as shown in Figure 47. The primary fracture is a longitudinal crack that developed between the heat-affected zone (HAZ) and the fusion zone (FZ), and propagated predominantly along the axial direction of the tube. During its propagation, the crack path deviated on three occasions, fully crossing the weld bead before continuing its propagation in the axial direction. At these crossing locations, several secondary cracks are observed, typical of environmentally assisted cracking phenomena. At both extremities of the main axial fracture, the

crack morphology changes significantly, leading to branching zones that propagate into the base metal (BM) of the tube (the part not affected by the welding).

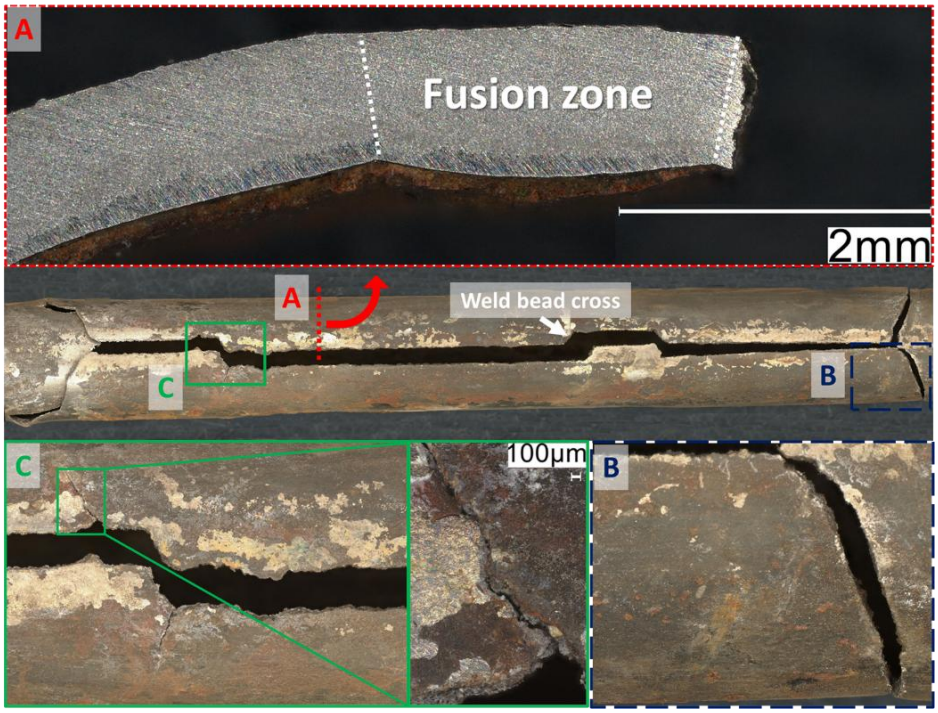

Figure 47 - Classification of the different fracture zones. A) Axial break section along the edge of the weld seam, B) Branching and C) Secondary cracks

Solid masses (Figure 48 A) were found inside the tube and EDS analysis showed to be rich in Fe, O, P, Ca, and S. In addition, a homogeneously dispersed red-brown scale was observed on both the inner and outer surfaces of the tube. This scale appeared loosely adherent to the tube. EDS analysis of the surface scale confirmed the presence of Fe, S, and O, indicating the formation of iron-rich corrosion products with a significant sulfur content. These deposits are reasonably attributed to corrosion products originating from steel components located upstream of the heat exchanger and subsequently transported inside the heat exchanger.

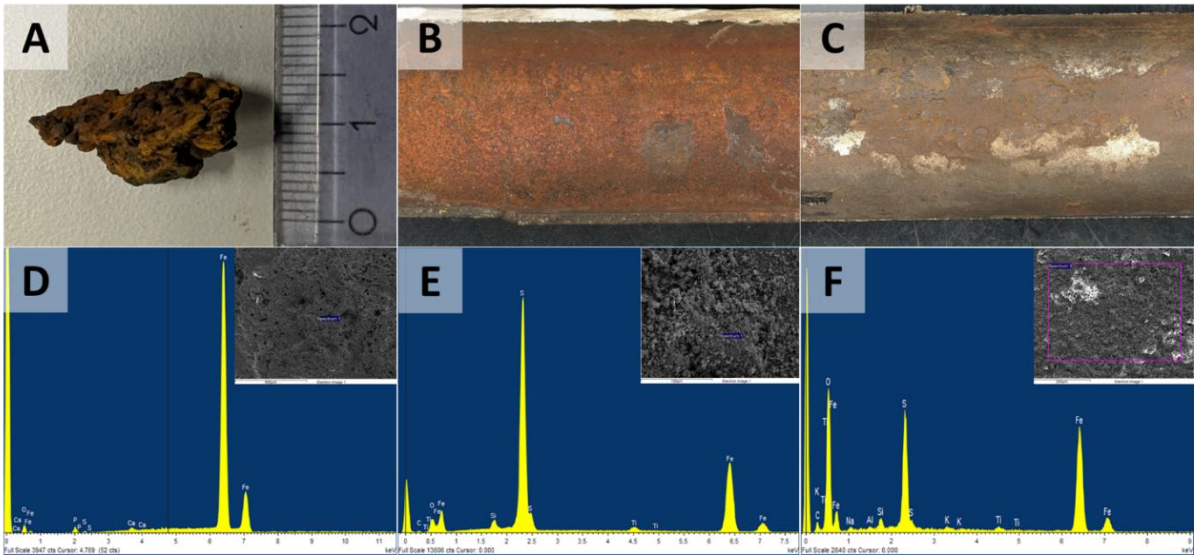

Figure 48 – Images of deposits and particles at the tube side (images A, B and C)) and respective EDS spectrum (D, E and F)

Cross-section observation revealed two distinct layers of corrosion products on the inner surface of the tube, as visible in Figure 49. EDS analysis showed that layer in contact with the tube is rich in S and Fe, so it reasonable to assume that it is iron sulfide produced by corrosion of steel upstream of the exchanger. An additional outer layer is observed and characterized by a different morphology and composition, infact EDS analysis demonstrated to be rich in O and Fe (Figure 49). This layer, being more external, appears credible to be iron oxide formed by atmospheric corrosion between the time of tube fracture and the analysis conducted in the laboratory. The presence of sulfur in geothermal environments is typically associated with hydrogen sulfide (H_2S), which readily dissociates and lowers the pH of the medium. Under these acidic conditions, hydrogen generation on titanium may occur, particularly when it is galvanically coupled to actively corroding materials such as carbon steel or stainless steel [212].

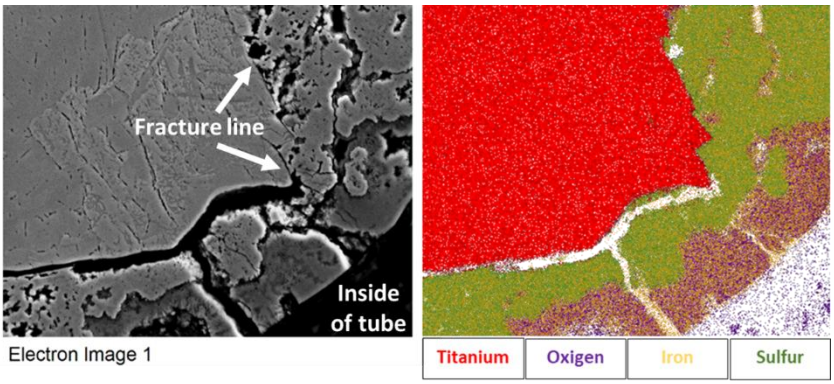

Figure 49 - EDS analysis of a cross section of the fracture of the damaged tube

A distinct microstructural transition is observed from the base metal (BM) to the fusion zone (FZ). The BM is characterized by equiaxed α-phase grains, while the heat-affected zone (HAZ) shows a progressive grain coarsening that gradually evolves into a basketweave-type microstructure. Due to the intrinsically low thermal conductivity of commercially pure titanium, heat dissipation during welding is limited, promoting further grain growth and the development of coarse grains within the FZ. Consequently, the FZ displays a Widmanstätten α-phase structure, formed under moderate rapid cooling conditions. Overall, the observed microstructures are compliant with typical of unalloyed welded titanium, as previously reported in the literature [70,213,214].

In all areas of the tube, lenticular plate hydrides are present. Their spatial distribution varies depending on microstructure. In general, hydrides formation in titanium is heterogeneous, depending on different microstructural characteristic such as the host lattice, the distribution of phases, orientation of the grains, vacancies, solute atoms, dislocations and grain boundaries [38,215]. Briant et al. [37] demonstrated that hydride formation in commercially pure titanium initiates preferentially at grain boundaries. In their study, hydrides were exclusively observed along grain boundaries for hydrogen concentrations up to 2950 wppm, where they appeared as finely dispersed particles. As the hydrogen content increased, the hydrides became coarser and more defined. Only at a concentration of 3490 wppm were hydrides found uniformly distributed throughout the material [37].

In the BM of the tube, hydrides are primarily located along equiaxed grain boundaries, in agreement with literature. In contrast, in the HAZ, hydrides are observed both at grain boundaries and within the grains. Their orientation in this region tends to follow specific directions aligned with the Widmanstätten lamellae. To the authors' knowledge, no studies have been reported addressing the formation and distribution of hydrides in commercially pure titanium exhibiting a Widmanstätten microstructure. For Ti-6Al-4V alloys, however, similar microstructures have been associated with hydride formation along α/β interfaces, iron-containing intermetallic particles, and grain boundaries [38,202,216,217].

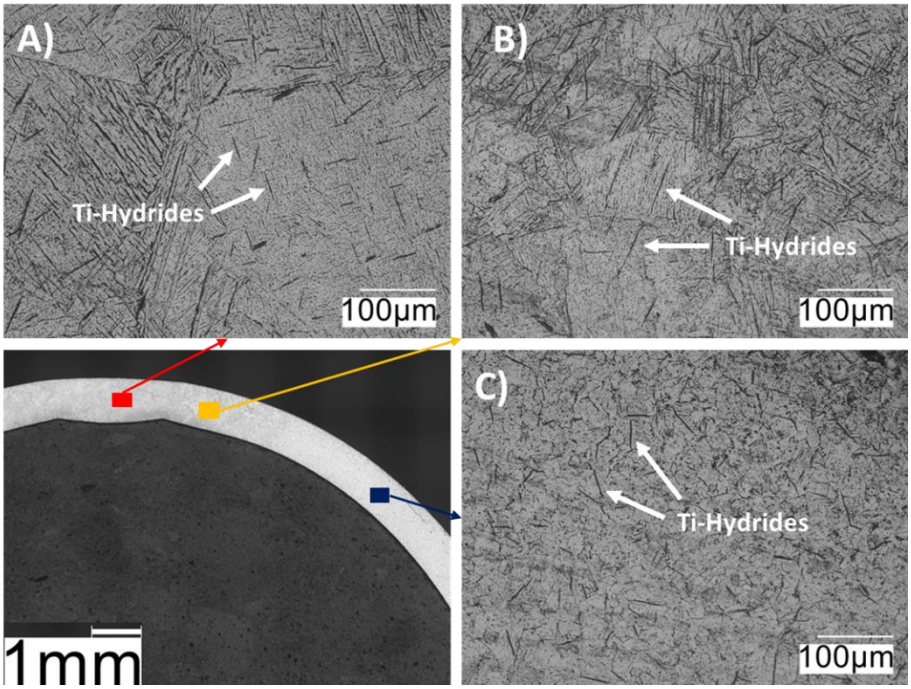

Figure 50 - Metallography of the tube in A) Fusion zone, B) Heat affected zone and C) Base metal

Hardness measurements show no significant variation between the base metal (BM) and the regions affected by welding, including the heat-affected zone (HAZ) and the fusion zone (FZ). In addition, no systematic hardness gradient is observed across the wall thickness of the tube. The measured hardness values fall within a comparable range for all investigated regions. This behavior is consistent with literature on weld characterization of commercially pure titanium, which report limited hardness variations associated with welding due to the absence of phase transformations and strengthening mechanisms typically observed in alloyed titanium grades [213,218,219].

Tabella 1 – HK0.01 of different areas of the tube

	Base metal	Heat affected zone	Fusion zone
Mean	219.4	201.0	204.6
St. dev.	28.0	22.8	11.4

7.3.2 Mechanism and cause of fracture

The tube failure is attributed to hydrogen embrittlement. Several experimental observations support this conclusion, including the presence of titanium hydrides, hydrogen-induced cracking features, and the occurrence of secondary cracks, which are commonly reported characteristics of hydrogen embrittlement phenomena (Figure 51). Lactic hydride etching (Figure 47Figure 51B) revealed that cracks propagations preferentially proceed along hydrides, thus fracture paths are strongly influenced

by the orientation of the lamellar microstructure. Consequently, crack propagation proceeds along specific crystallographic directions associated with the Widmanstätten lamellae. This behavior is consistent with a reduction in fracture toughness induced by the formation of brittle titanium hydrides. As reported in the literature, increasing hydrogen content in commercially pure titanium leads to a progressive loss of ductility and promotes a transition in fracture mode from ductile microvoid coalescence to brittle or quasi-cleavage fracture [37,215,220].

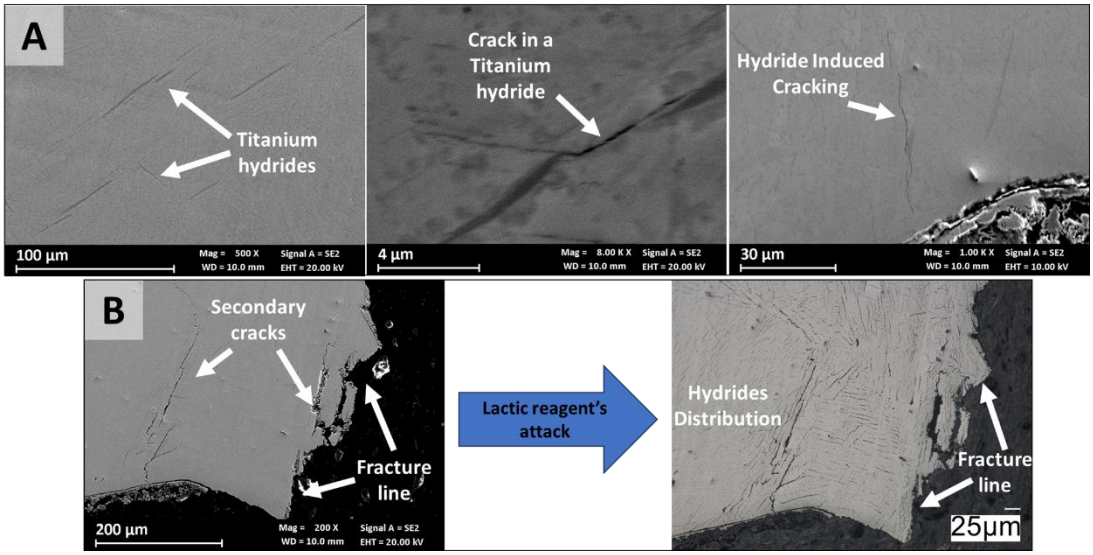

Figure 51- Cross section of the tube. A) FESEM image of polished surface B) Optical image after lactic reagent's attack to detect titanium hydrides

Fractographic analysis confirms features consistent with hydrogen embrittlement (HE) (Figure 52), revealing a predominantly brittle fracture both in the axial fracture and in the branching zone [37,39,221]. In the fusion zone (FZ), the fracture surface is characterized by larger and more extended brittle facets compared to those observed in the branching regions. In addition, secondary cracks are frequently observed and tend to follow paths that correlate with the spatial distribution of titanium hydrides. The brittle surfaces are often inclined with respect to the maximum stress plane and exhibit a flat, smooth morphology. This behavior can be attributed to hydrogen segregation, which reduces grain boundary cohesion, thereby promoting crack propagation. Despite the predominance of brittle features, localized plastic deformation is also observed in both the axial fracture and the branching zones, indicating the coexistence of brittle and ductile fracture mechanisms. Such mixed-mode fracture behavior is widely recognized as a characteristic feature of hydrogen embrittlement in titanium and its alloys [37–39,222]. As hydrogen content increases, the fracture surface progressively evolves toward a more brittle morphology initially characterized by large micro voids, then by a

combination of brittle facets and smaller voids, and ultimately by a fully brittle surface dominated by cleavage facets [37].

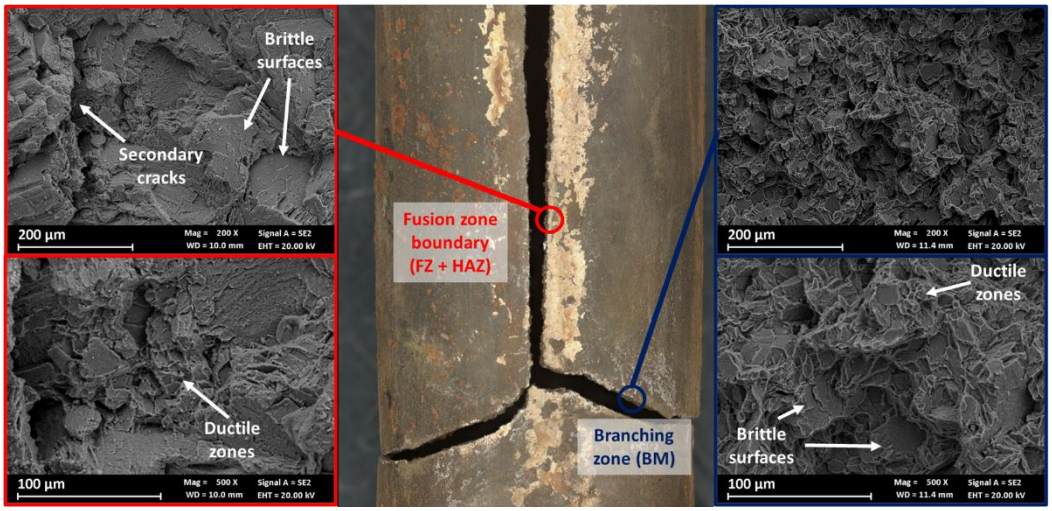

Figure 52- Fracture analysis of the tube in the fusion zone and in the base metal

The failure of this tube occurred through the formation of hydrogen-induced cracks at the edge of the fusion zone (FZ), which subsequently propagated along the axial direction of the tube until branching occurred in the base metal (BM) region. Crack nucleation associated with hydrogen embrittlement is known to initiate near stress concentrators, such as notches [38]. Therefore, in a welded tube, HE-related failure is expected to originate at the boundary of the fusion zone, where local stress concentrations are highest due to residual stresses and geometrical features.

The possible causes of hydrogen embrittlement leading to the observed failure can be attributed to two possible mechanisms. The first is associated with the manufacturing, in fact titanium is known to be susceptible to hydrogen uptake if the welding process is not properly controlled. In the presence of inadequate shielding, surface contamination, or unfavorable thermal cycles hydrogen can be absorbed during welding and subsequently become trapped in regions characterized by high residual stresses, such as the fusion zone and the adjacent heat-affected zone [223]. Cross et al. [224] demonstrated that hydrogen embrittlement in titanium weldments is not necessarily evident after fabrication, as cracking may occur delayed. Following hydrogen uptake, the material becomes embrittled, while crack nucleation may take place at a later stage, once welding is completed and the component appear intact. The presence of hydrides increases the yield strength while significantly reducing plastic deformation capability, thus promoting crack initiation in areas of localized stress concentration during service [225]. A representative example of hydrogen embrittlement induced by inadequate welding conditions was reported by Tawancy et al. [217], who described the premature

failure of a welded floater made with titanium Grade 2. In that case, excessive hydrogen absorption during welding led to hydride precipitation and brittle cracking after few weeks.

Hydrogen embrittlement could be also originated by the service environment. Titanium may be susceptible to hydrogen absorption during service in environments capable of sustaining continuous hydrogen generation. It is well established that hydrogen up-take in titanium requires the simultaneous occurrence of specific environmental and electrochemical conditions. These include either acidic or strongly alkaline environments, typically characterized by a solution pH below approximately 3 or above 12, as well as elevated temperatures, generally above about 80 °C. However, hydride formation may also occur at lower temperatures in the presence of severe tensile stresses and a continuous source of hydrogen generation. Such hydrogen sources can arise from galvanic coupling with dissimilar metals, corrosion processes involving titanium itself, or the application of excessive cathodic protection currents [212,226]. In geothermal applications, elevated temperatures, steam containing aggressive species may promote hydrogen evolution and ingress into the material [65,207,209]. In such cases, hydrogen embrittlement may develop independently of the welding process and affect both welded and unwelded regions of the component.

The hydrogen concentrations throughout the tube exceed the limit of 150 ppm specified by ASTM B338 for commercially pure titanium, so this suggest that the root of the embrittlement can be attributed to an increase of H content during the service life. Hydrogen analysis revealed concentrations of 277.3 ppm in the FZ and HAZ and 183.0 ppm in the BM, whereas the reference titanium Grade 2 material exhibited a hydrogen content of only 4.7 ppm. Hydrogen concentrations on the order of 200 ppm are known to promote hydrogen-induced cracking in titanium [227]. When combined with the presence of brittle fracture surfaces and titanium hydrides, even within the BM, these results indicate that embrittlement occurred also in regions not directly affected by welding.

The difference in hydrogen concentration between the FZ and the BM could be attributed to a variation in HE susceptibility associated with differences in microstructure. Several studies have shown that hydride formation is strongly influenced by grain size and orientation [38,39]. Moreover, residual stresses and the local stress distribution play a key role in the mechanism of hydride precipitation. Even when the hydrogen concentration is below the critical threshold for hydride formation, prolonged exposure to stress in localized regions can still promote hydride precipitation [215,220]. Hydride formation is accompanied by a volumetric expansion of approximately 24.2%, which generates a self-sustaining stress field around the precipitate. This promotes an autocatalytic mechanism, whereby the growth of an initial hydride facilitates the nucleation of additional hydrides nearby [39]. Furthermore, it can be hypothesized that if microcracks were already present in the weldment, hydrogen atoms would tend to diffuse toward the crack tip. In this region, the triaxial stress

state results in the formation of large interstitial sites in the lattice, which can more easily accommodate hydrogen atoms and serve as preferential sites for hydrogen accumulation [214].

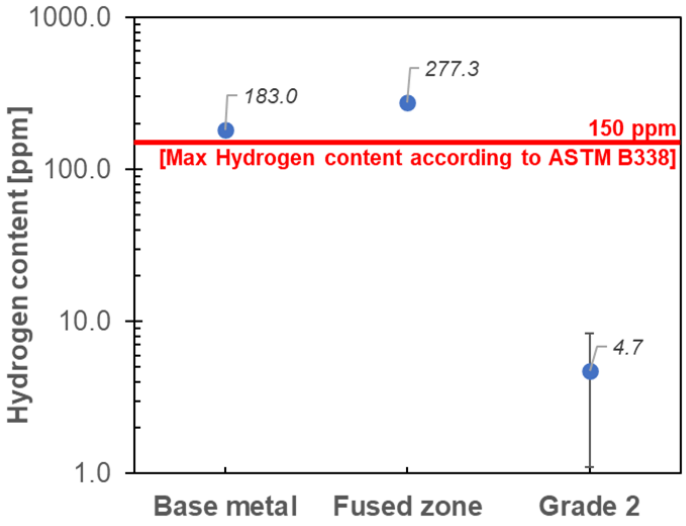

Figure 53 - Hydrogen content in the titanium tube

Overall, the experimental evidence clearly supports hydrogen embrittlement as the failure mechanism responsible for the rupture of the investigated tube. The presence of titanium hydrides, hydrogen-assisted cracking features, predominantly brittle fracture surfaces, and hydrogen contents exceeding the ASTM B338 limit provide a consistent and self-supporting framework for this conclusion. However, it was not possible to unequivocally determine whether hydrogen embrittlement was primarily caused by the service conditions of the tube, by the initial condition of the material, or by a combination of both factors. Even if the technical data sheet of the tube reports that the material was compliant with the standard ASTM B338, the lack of hydrogen content measurements in the as-received material prior to service prevents a definitive distinction between hydrogen uptake occurring during manufacturing and that accumulated during long-term service exposure. For a component that operated for approximately 10 years, it is therefore more appropriate to consider the welded region as a structural and microstructural weak link, rather than as the sole source of hydrogen.

Several strategies can be considered to reduce the risk of hydrogen embrittlement in similar applications. If modification in material selection is not feasible, the first step should be given to systematic control of hydrogen content in incoming materials to discriminate the nature of hydrogen embrittlement. In addition, the use of titanium alloys specifically developed for acidic and reducing environments should be considered. Alloys containing platinum group metal additions, such as Grade 29, or alloys with a high molybdenum content, such as Ti-6Al-2Sn-4Zr-6Mo, are specially developed for sour geothermal service where HE is a critical phenomenon [207,208,228]. Another solution could

be mitigating the harshness of the environment with upstream treatment of geothermal steam. Controlling pH, removing corrosive species such as H_2S and CO_2, or limiting the formation of acidic condensates, can significantly reduce degradation mechanisms in geothermal heat exchanger [29,229]. Such approaches are commonly adopted in geothermal installations to mitigate corrosion and scaling phenomena and may indirectly decrease hydrogen uptake by metallic components.

7.4 Conclusion

The failure of the titanium Grade 2 tube was caused by hydrogen embrittlement, confirmed by the presence of hydrides, brittle fracture, and elevated hydrogen content throughout the entire material.
The fracture originated at the fusion zone, where stress concentrations favored nucleation of hydride and crack propagation. Hydrides were also detected all over the tube, suggesting that embrittlement was extended also in not-welded region. These observations have been confirmed by hydrogen content measurements.
This study reports a failure analysis in geothermal sectors of titanium which tends to be considered a material immune to corrosion problems. Findings confirm that titanium is not always completely immune to in-service failure, challenging the assumption that this material represents a universally safe solution for aggressive geothermal environments. This consideration motivates the investigation of advanced titanium alloys discussed in the following chapter.

Chapther 8. Corrosion behavior of titanium alloys in reducing acidic media produced by AM technologies

8.1 Chapter introduction

The outstanding corrosion resistance of titanium alloys is primarily associated with the formation of a thin, adherent, and self-healing passive oxide film, mainly composed of TiO_2 [69]. This oxide exhibits a wide stability domain in terms of both potential and pH (Figure 8) except for low potential and acidic conditions where the stability of the passive oxide layer can be compromised. In the geothermal sector, titanium alloys are widely applied for components such as heat exchangers, tubing, turbine blades and structural elements [207]. Nevertheless, highly aggressive environments characterized by reducing acidic conditions and elevated temperatures tends to require the use of titanium alloys specifically developed to enhance corrosion resistance under such conditions.

The present study investigates the corrosion resistance of selected titanium alloys produced by AM under acidic reducing conditions, with the aim of identifying promising candidates for geothermal applications. Ti-6Al-4V was selected as a reference material because is most widely used titanium alloy and is extensive adopted in AM across aerospace, energy, and biomedical sectors [88,89]. In addition, Ti-6Al-2Sn-4Zr-6Mo, a titanium alloy specifically developed for aggressive environments, was included owing to its improved resistance to general and crevice corrosion in chloride-containing acidic media [70,91].

Titanium aluminides represent a distinct class of materials primarily developed for high-temperature structural applications, owing to their low density and excellent oxidation resistance [230]. AM offers significant advantages for TiAl alloys, as it enables the production of components with enhanced microstructural homogeneity that is difficult to achieve through casting [231,232] .

The reference materials consist of the most widely used titanium alloy (Ti-6Al-4V) and its version specifically developed to enhance corrosion resistance in reducing acidic environments (Ti-6Al-4V-Ru).

The results of this work provide valuable insights for the material selection of titanium-based materials intended for service in reducing acidic environments, contributing to a more informed use of both conventionally processed and additively manufactured alloys in aggressive operating conditions, with relevance for geothermal applications.

8.2 Materials and methods

8.2.1 Materials

The additively manufactured materials investigated in this study include two titanium alloys (Ti-6Al-4V and Ti-6Al-2Sn-4Zr-6Mo) and two titanium aluminides (Ti-48Al-2Cr-2Nb and Ti-48Al-2Cr-8Nb). The materials investigated in this study and their corresponding designations are summarized in Table 16.

Table 16 – Material considered in this study

Material	Common designation	UNS code	Technology
Ti-6Al-4V	Ti64	R56400	Wrought and LPBF
Ti-6Al-4V-Ru	Ti64-Ru	R56401	LPBF
Ti-6Al-2Sn-4Zr-6Mo	Ti6246	R56260	EBM
Ti-48Al-2Cr-2Nb	γ-TiAl	—	EBM
Ti-48Al-2Cr-8Nb	γ-TiAl-Nb	—	Wrought

LPBF-manufactured specimens of Ti-6Al-4V were manufactured using an EOS M270 Dual Mode system equipped with an Yb laser source under an argon atmosphere. The process parameters were laser power of 170 W, a scanning speed of 1250 mm/s and a hatching distance of 100 μm. It's a common knowledge that Ti-6Al-4V form metastable martensitic α′ phase due to the extremely high cooling rates of the LPBF process [233]. For this reason, a stress-relief heat treatment at 680°C for 4h under high vacuum was applied to reduce residual stresses and to promote the decomposition of the brittle α′ martensite into a more stable α+β lamellar microstructure. Further details can be found in [234].

Titanium aluminides were produced from gas-atomized pre-alloyed powder with two different atomic percentage composition (Ti-48Al-2Cr-2Nb and Ti-48Al-2Cr-8Nb) using an Arcam system operating under high-vacuum conditions. A controlled helium atmosphere was employed during melting to prevent electrostatic charging and limit contamination. After fabrication, the samples were subjected to hot isostatic pressing (HIP) at 1260 °C under 1700 bar for 4 h, followed by a post-HIP heat treatment at 1320 °C for 2 h to promote the formation of a duplex lamellar microstructure. Further details can be found in [231,232].

Ti-6Al-2Sn-4Zr-6Mo samples were produced by LPBF using a pre-alloyed gas-atomized powder on an EOS M270 Xtended system. Processing parameters consist of a laser power of 190 W, a scan speed of 1100 mm/s, and a hatching distance of 0.10 mm, corresponding to a volumetric energy density of 57.6 J/mm^3. A previous study investigating the feasibility of producing this material by LPBF highlighted that Ti-6Al-2Sn-4Zr-6Mo exhibits a microstructure characterized by the formation of brittle α″ martensite in the as-built condition [91]. For this reason, the specimens were subjected to a stress-relief heat treatment at 750 °C for 2 h under high vacuum, followed by slow furnace cooling.

Ti-6Al-4V was selected as a benchmark material because it is the most widely used and commercially common titanium alloy. In particular, two condition of Ti-6Al-4V annealed was considered: Grade 5 as the baseline condition and Grade 29 which includes the addition of 0.1 wt.% Ru to significantly enhance the resistance in reducing acidic environments. The chemical compositions of all investigated materials are summarized in Table 17.

Table 17 – Chemical composition of titanium alloys tested

Material	Condition	Al	V	Sn	Zr	Mo	Cr	Nb	Ru	O	N	H	Fe	C	Ti
Ti-6Al-4V	Bar	6.24	4.23	/	/	/	/	/	/	0.172	0.012	0.001	0.137	0.01	Bal.
Ti-6Al-4V	Powder	5.86	3.99	/	/	/	/	/	/	0.08	0.003	0.002	0.18	0.01	Bal.
Ti-48Al-2Cr-2Nb*	Powder	34.1	/	/	/	/	2.4	4.8	/	0.06	0.004	/	0.03	0.005	Bal.
Ti-48Al-2Cr-8Nb*	Powder	31.3	/	/	/	/	2.2	17.2	/	0.04	/	/	/	/	Bal.
Ti-6Al-2Sn-4Zr-6Mo	Powder	5.5–6.5	/	1.75–2.25	3.5–4.5	5.5–6.5	/	/	/	<0.15	<0.04	/	<0.15	<0.04	Bal.
Ti-6Al-4V-0.1Ru	Bar	5.8	3.99	<0.030	0.005	0.13	0.022	0.038	0.099	/	<0.005	/	0.17	<0.005	Bal.

*Fot titanium aluminides the common designations are based on atomic composition rather than weight percentage.

8.2.2 Microscopic analysis

Images were acquired using a KEYENCE VHX-7100 digital optical microscope and a Gemini Sigma 300 FESEM was employed to analyses the surface of the specimens after the corrosion tests and for metallographic purpose. Kroll's reagent (3 mL HF, 6 mL HNO_3, H_2O to 1000 mL) was used to reveal the microstructure.

8.2.3 Hardness testing

Vickers microhardness measurements were carried out using a UHL VMHT microhardness tester, applying a load of 1000 gf for 15 seconds (HV1). A minimum of 10 indentations were performed on each sample condition.

8.2.4 Immersion tests for generalized corrosion in acidic media

Generalized corrosion tests were carried out in accordance with ASTM G31. Prior to testing, cylindrical specimens with 15 mm of diameter and 5 mm of height were obtained through W-EDM cutting. Surface preparation consisted of grinding with SiC abrasive papers up to 1200 grit. Before and after immersion tests, the specimens were removed from the solution, thoroughly rinsed with distilled water, washed with acetone, dried, and weighed using an analytical balance with a sensitivity of 0.01 mg. Tests were performed in a 1 L Erlenmeyer flask fitted with a reflux condenser.
The corrosive environment consisted of boiling hydrochloric acid (HCl) solutions at different concentrations (0.01 M, 0.1 M, and 1 M). For each condition, one specimen was immersed in a glass beaker, ensuring a constant volume solution to exposed area ratio of 0.5 mL/mm^2. The immersion tests were performed for a total duration of 24 h.

8.2.5 Immersion tests for localized corrosion

Localized corrosion tests were performed in boiling saturated magnesium chloride solution using a 1 L Erlenmeyer flask fitted with a reflux condenser. The tests were conducted at 130 °C, 150 °C, and 175 °C. Due to the difficulty in accurately measuring the volume of the highly concentrated boiling solution, a fixed amount of 600 g of magnesium chloride hexahydrate was used for each specimen. Nevertheless, a minimum of volume solution to exposed area ratio of 0.5 mL/mm^2 was ensured for all tests. After exposure, the specimens were cleaned following the same procedure adopted for the

generalized corrosion tests and weighed using an analytical balance. In all cases, the measured mass losses were negligible. The assessment of localized corrosion was therefore primarily based on microstructural observations. The exposed surfaces were systematically examined by OM and FESEM to verify if localized corrosion phenomena had effectively occurred.

8.3 Results and discussion

8.3.1 Microstructures and mechanical behavior

Figure 54 shows the microstructures of the investigated materials. Ti-6Al-4V and Ti-6Al-2Sn-4Zr-6Mo belong to the class of α+β titanium alloys, characterized by the coexistence of a hexagonal close-packed (hcp) α phase and a body-centered cubic (bcc) β phase. In annealed conditions, these materials develop a duplex microstructure with globular primary α grains embedded in a transformed β matrix, from which secondary α may precipitate during cooling [235,236]. This microstructural configuration is observed in the benchmark materials wrought Ti-6Al-4V and Ti-6Al-Ru, where rolling provided also a preferential grain elongation.

In contrast, LPBF process is characterized by very high solidification and cooling rates, which suppress diffusion transformations. Under these conditions, α+β titanium alloys experience martensitic transformation, analogous to quenching, leading to the formation of metastable α′ or α″ martensite [237]. This mechanism represents the primary hardening process in as-built AM components, as the martensitic microstructure is composed of very fine acicular laths. It is well established that LPBF-processed Ti-6Al-4V exhibits a brittle as-built microstructure dominated by α′ martensite [233]; similarly, Carrozza et al. demonstrated that the Ti-6Al-2Sn-4Zr-6Mo alloy undergoes an analogous transformation during AM, with the formation of α″ martensite [91]. As shown in Figure 54, stress-relieving led to a decomposition of the martensitic phase, resulting in a fine lamellar α+β microstructure both in Ti-6Al-4V and Ti-6Al-2Sn-4Zr-6Mo.

Conversely, titanium aluminide alloys are not characterized by the common α and β phases of titanium alloys. When the aluminum content ranges between 44 and 49 at. %, a dual-phase microstructure composed of γ-TiAl and α_2-Ti_3Al is generally formed. The mechanical properties of TiAl intermetallic are strongly dependent on their microstructure and on the spatial distribution of phases within the material[238,239]. In this context, AM represents a particularly attractive processing route for TiAl alloys, as it has been demonstrated to provide a significantly improved microstructural homogeneity compared to conventional casting[240].

The Ti-48Al-2Cr-2Nb and Ti-48Al-2Cr-8Nb alloys investigated in this study exhibit a duplex microstructure consisting of equiaxed γ grains and lamellar γ/α_2 colonies, as already documented in previous works on these materials [231,232]. Heat treatments promote the stabilization of this microstructure, where the α_2-Ti_3Al phase originates from the decomposition of the high-temperature α phase.

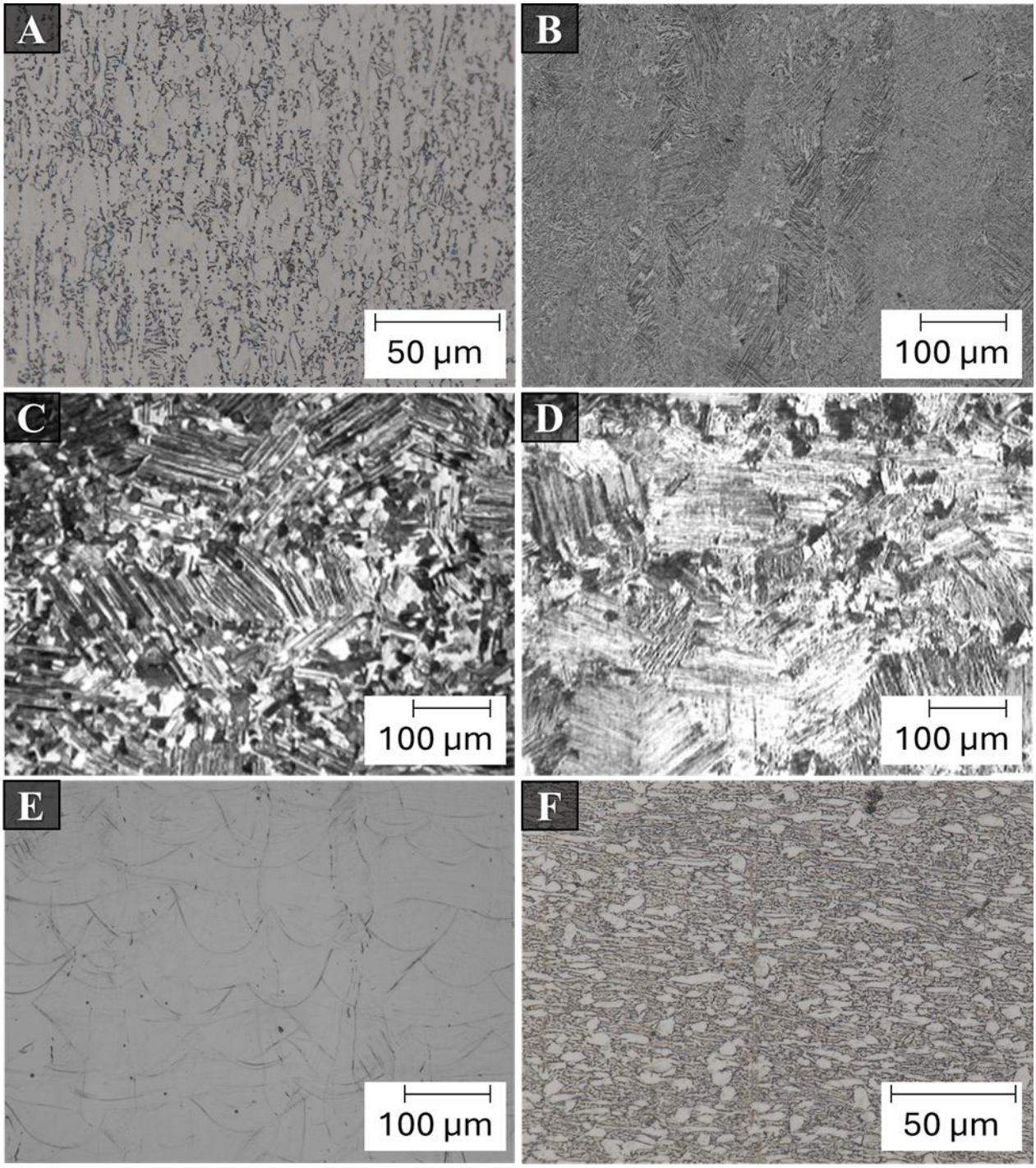

Figure 54 – Microstructures of the investigated materials: A) Ti-6Al-4V HW, B) Ti-6Al-4V LPBF, C) Ti-48Al-2Cr-2Nb [231], D) Ti-48Al-2Cr-8Nb [232], E) Ti-6Al-2Sn-4Zr-6Mo F) Ti-6Al-4V-Ru.

The microstructure of the material has a direct influence on the hardness of the Ti-6Al-4V alloy. In particular, the highest hardness values were measured for LPBF-produced Ti-6Al-4V because of the fine lamellar. In contrast, the same alloy produced by conventional routes exhibits hardness values approximately 50 Vickers points lower, consistent with a coarser grain structure. Moreover, the comparison between the two benchmark materials confirms that the addition of 0.1 wt.% Ru does not produce a measurable hardening effect.

The Ti-6Al-2Sn-4Zr-6Mo alloy exhibits outstanding hardness values, although these remain in line with those expected for this material [70]. This behavior can be explained by considering that it has higher content of β-stabilizer compared to Ti-6Al-4V, which promotes the formation of α″ martensite rather than α′ during rapid cooling. The α″ martensitic phase is known to be comparatively softer and more deformable than α′, owing to its orthorhombic structure and lower lattice distortion. Carrozza et Al. [236] demonstrated that the decomposition of α″ martensite through heat treatment leads to a significant increase in hardness. The material exhibiting the lowest hardness is Ti-48Al-2Cr-2Nb. However, a marked increase in hardness is observed for Ti-48Al-2Cr-8Nb. This behavior can be attributed to the addition of Nb, which enhances the hardness of γ-TiAl alloys through solid-solution strengthening and stabilize the lamellar microstructure by lowering the atomic diffusion [239].

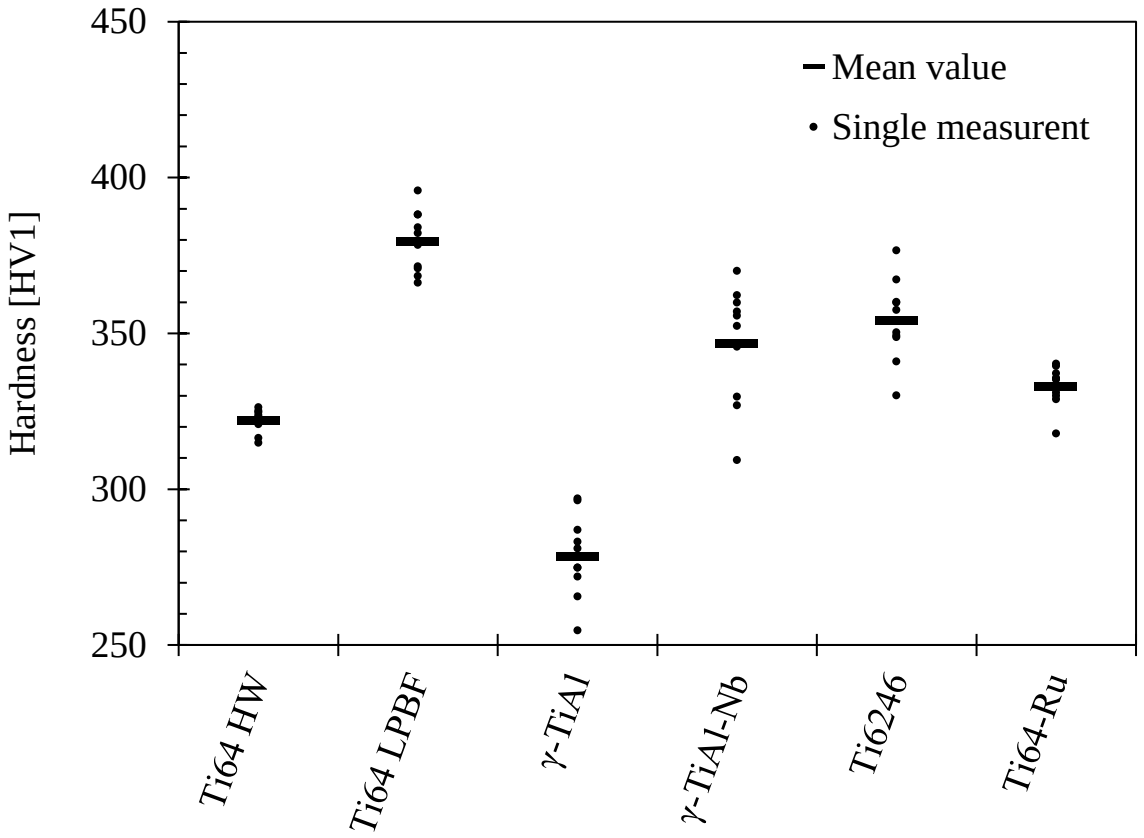

Figure 55 - Vickers hardness (HV1) of the investigated materials. Dots represent individual measurements, while horizontal bars indicate mean values.

8.3.2 Generalized corrosion behavior in boiling HCl

After the immersion tests conducted at pH 2, the specimens exhibited final weights comparable to their initial values and no visible anodic dissolution zones or color changes of the surface were detected. These results indicate a fully passive condition of all investigated materials in boiling solution of 0.01 M HCl for an exposure time of 24 h, including both titanium alloys and titanium aluminides.

At pH 1, the intermetallic specimens began to exhibit visible corrosion phenomena, whereas the titanium alloys don't show apparent surface degradation. This behavior highlights the lower passive range in reducing acidic conditions of the oxide film of γ-TiAl compared to titanium alloys.

Differently, specimens of every investigated material were severely corroded after tests conducted in pH0, as visible in Figure 56.

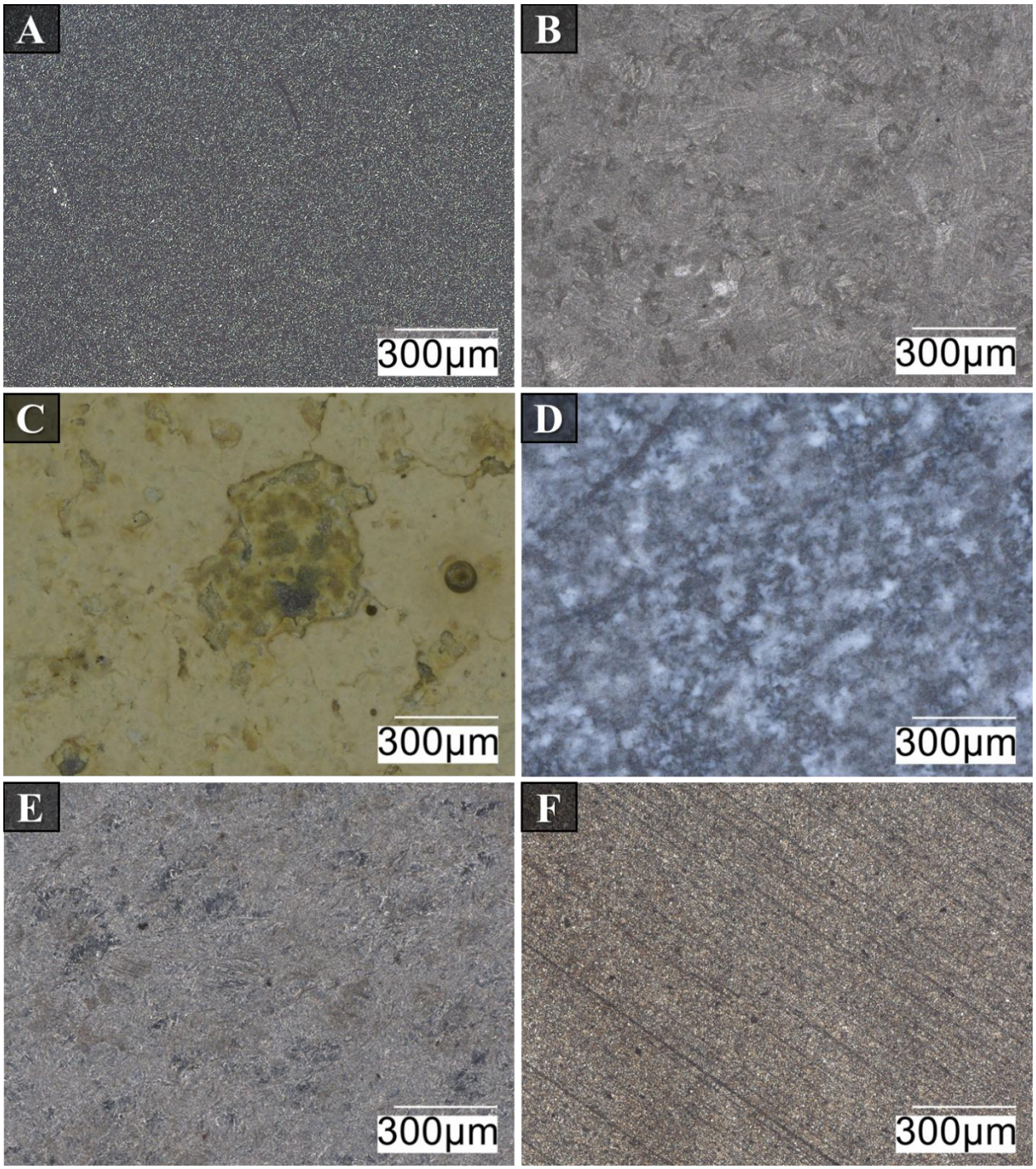

Figure 56 - Surface morphology of the investigated materials after immersion in boiling HCl at pH0: A) Ti-6Al-4V HW, B) Ti-6Al-4V LPBF, C) Ti-48Al-2Cr-2Nb, D) Ti-48Al-2Cr-8Nb, E) Ti-6Al-2Sn-4Zr-6Mo F) Ti-6Al-4V-Ru.

The results obtained from acidic corrosion tests show that the presence of aluminum in titanium-based materials leads to a drastic deterioration of corrosion resistance in reducing acidic environments. Among the investigated materials, Ti-48Al-2Cr-2Nb exhibited the highest corrosion rate (Table 18), indicating severe generalized attack under strongly acidic conditions. This behavior is primarily attributed to the presence of aluminum, which it's known to worsen the corrosion resistance of titanium in acidic media [69,203,241]. The addition of Nb in Ti-48Al-2Cr-8Nb resulted

in a reduction of the corrosion rate by approximately one order of magnitude at both pH0 and pH1; however, the corrosion rates remained significantly higher than those measured for conventional titanium alloys. The beneficial effect of Nb on the corrosion resistance of titanium alloys has been previously reported in the literature. Yu and Scully [242] revealed that additions of Nb, Zr, and Mo improved the corrosion resistance and passivity of Ti in 5 M HCl solution. Lee et al. [243] discovered that the addition of 11 at. % Nb to Ti_3Al intermetallic improves the corrosion and pitting properties in neutral and acidic solutions. Shukla et al. [244] demonstrated that replacing V with Nb in Ti-6Al-4V enhances corrosion resistance by improving the stability of the passive oxide film. Nevertheless, despite this beneficial role, the corrosion rates measured for Ti-48Al-2Cr-8Nb remain higher than those of the commonly used Ti-6Al-4V alloy, indicating that the presence of higher content of aluminum still dominates the corrosion response in strongly acidic environments. Both wrought and LPBF Ti-6Al-4V showed intermediate corrosion rates at pH0, with comparable values despite the different manufacturing routes. This behavior indicates that the production process mainly affects the mechanical properties, while it has a limited influence on corrosion behavior in acidic media, which is primarily governed by alloy chemistry. An example of the limited influence of microstructure on the corrosion resistance of this alloy is that heat-affected zones in weldments generally do not experience corrosion-related weaknesses in welded components [205].

In contrast, Ti-6Al-2Sn-4Zr-6Mo exhibited a substantially lower corrosion rate, demonstrating excellent resistance even in boiling HCl at pH0. This behavior can be attributed to the high Mo content, which is known to enhance the stability and protectiveness of the passive film in acidic chloride-containing environments [69,70,203]. The beneficial role of Mo is well established in titanium alloys such as Grade 12, which is specifically employed for its superior resistance to crevice and general corrosion in aggressive media [245]. Molybdenum improves the corrosion resistance of titanium by promoting cathodic depolarization, thereby reducing the overall corrosion kinetics in acidic reducing environments. Within this context, platinum group elements, such as ruthenium, play an even more effective role, as much smaller additions are required to compare the effect of Mo. Accordingly, the lowest corrosion rates among all investigated materials were measured for Ti-6Al-4V-Ru, confirming the strong beneficial effect of Ru addition in reducing acidic environments. Platinum group elements act as powerful cathodic modifiers by promoting noble-metal enrichment at the surface, which facilitates rapid repassivation and significantly reduces anodic dissolution kinetics under reducing acidic conditions [75,107,208,246].

Table 18 - Corrosion rate of the investigated materials in boiling HCl solutions at pH0 and pH1.

Material	Technology	pH0	pH1

		Mean [mm/y]	Dev.St. [mm/y]	Mean [mm/y]	Dev.St. [mm/y]
Ti64	HW	19.1	0.2	0.770	0.021
Ti64	LPBF	18.6	0.1	0.712	0.056
γ-TiAl	EBM	585.8	12.1	29.533	0.725
γ-TiAl-Nb	EBM	135.6	3.8	4.366	0.156
Ti6246	LPBF	7.6	0.1	0.017	0.005
Ti64-Ru	HW	1.2	0.0	0.332	0.007

8.3.3 Localized corrosion behavior in boiling $MgCl_2$

The OM micrographs in Figure 57 show an example of pitting corrosion developed on Ti-6Al-4V after exposure to boiling $MgCl_2$ solution. The pits exhibit a semi-spherical morphology with porous corrosion products inside. Near the localized attack, iridescent regions are observed, which can be attributed to the formation of titanium oxide layers. The presence of these oxides is reasonably associated with the precipitation of titanium ions outside the anodic pitting region.

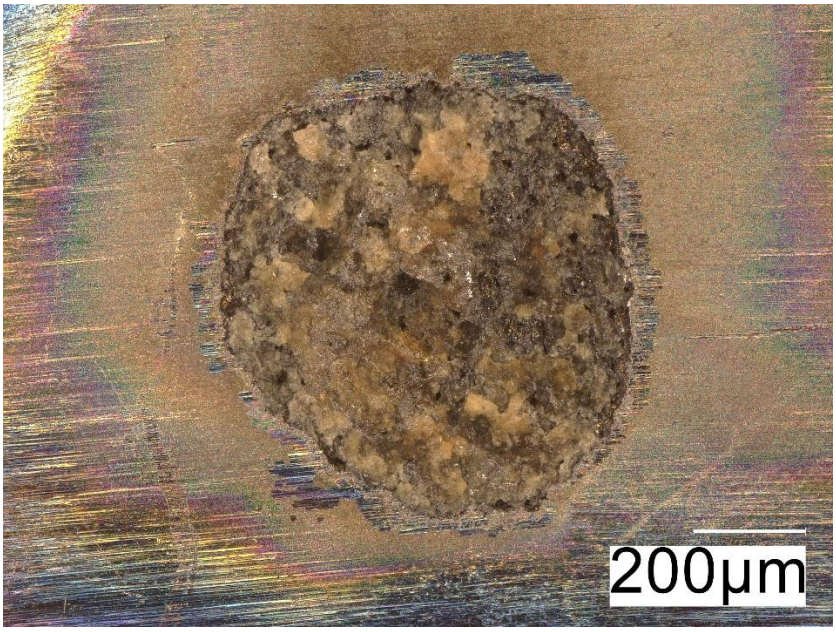

Figure 57 - OM micrograph of localized attack on Ti-6Al-4V after an immersion tests in a boiling solution of $MgCl_2$

These observations, common to all tested materials, confirm that the corrosion damage is dominated by localized attack (Figure 58). Specimens that successfully passed the test did not exhibit any visible surface damage after cleaning in acetone. In contrast, specimens affected by localized corrosion

showed well-defined cavities surrounded by iridescent, rainbow-like regions. The localized attacks observed in all investigated materials initially exhibit a globular morphology and progressively propagate into the material.

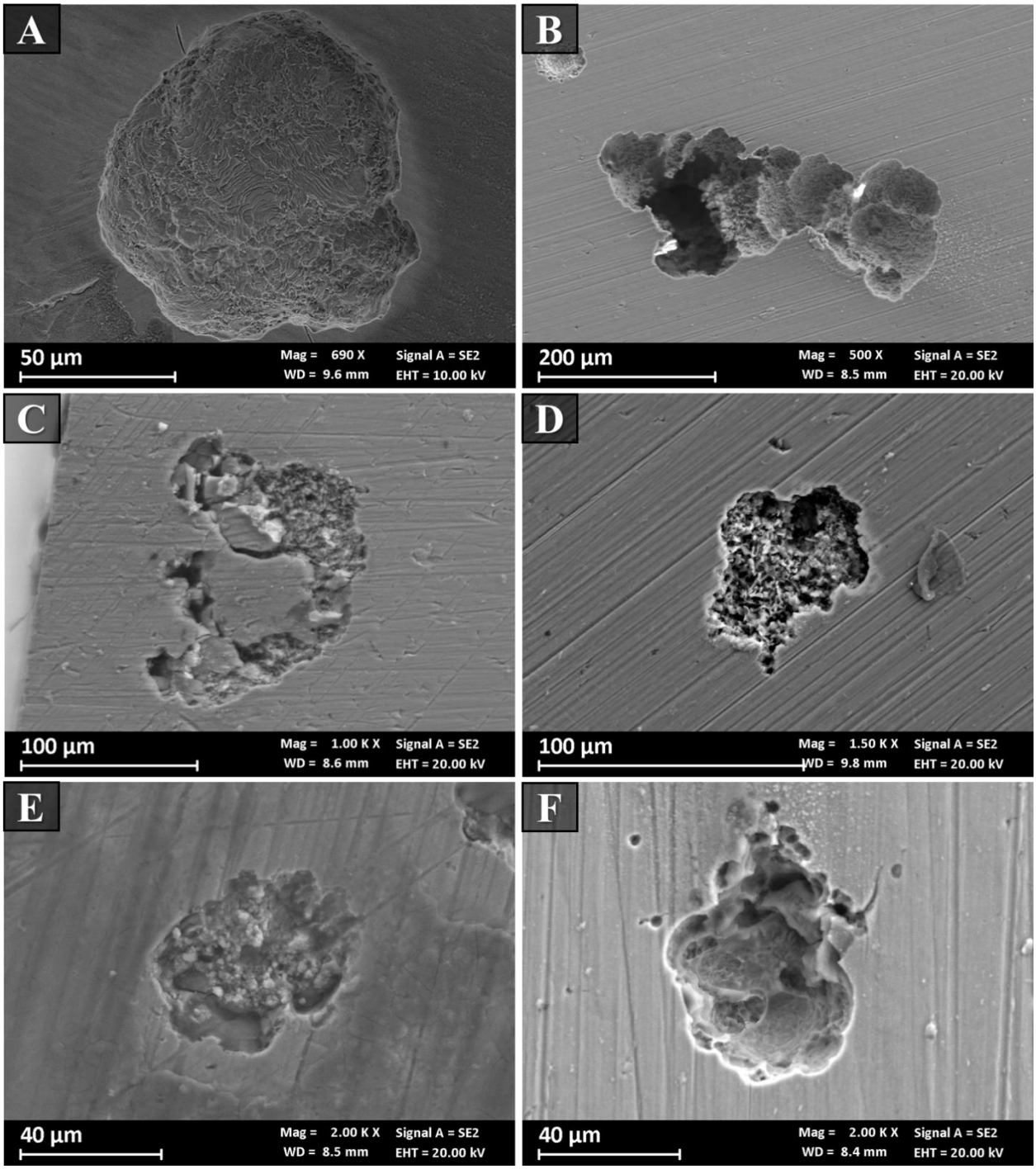

Figure 58 - FESEM micrographs of pitting corrosion morphologies observed on the investigated materials after immersion in boiling $MgCl_2$ solution. A) Ti-6Al-4V HW at 150°C, B) Ti-6Al-4V LPBF at 150°C, C) Ti-48Al-2Cr-2Nb at 130°C, D) Ti-48Al-2Cr-8Nb at 175°C, E) Ti-6Al-2Sn-4Zr-6Mo at 175°C F) Ti-6Al-4V-Ru at 175°C.

At the lowest investigated temperature, all the materials exhibit no pitting, indicating a relatively stable passive behavior except for Ti-48Al-2Cr-2Nb where an elevated Al content compromises resistance to localized corrosion. At 150 °C, pitting becomes progressively more frequent on Ti-48Al-2Cr-2Nb, and Ti-6Al-4V also exhibits localized attack in both wrought and LPBF-manufactured specimens. A notable exception is represented by Ti-48Al-2Cr-8Nb, which shows an excellent resistance to localized corrosion, remaining unaffected up to 150 °C in boiling $MgCl_2$. The superior behavior of this intermetallic alloy compared to Ti-6Al-4V may be related to the lower acidity of the $MgCl_2$ Although magnesium chloride hydrolysis promotes acidification, but it does not reach the extremely low pH values oh the HCl tests [247]. Increasing the temperature to 175 °C promotes pitting phenomena in all the investigated materials, confirming that temperature significantly increases the aggressiveness of the solution. Among the tested alloys, Ti-48Al-2Cr-8Nb, Ti-6Al-2Sn-4Zr-6Mo, and Ti-6Al-4V-0.1Ru exhibited the highest resistance to localized corrosion.

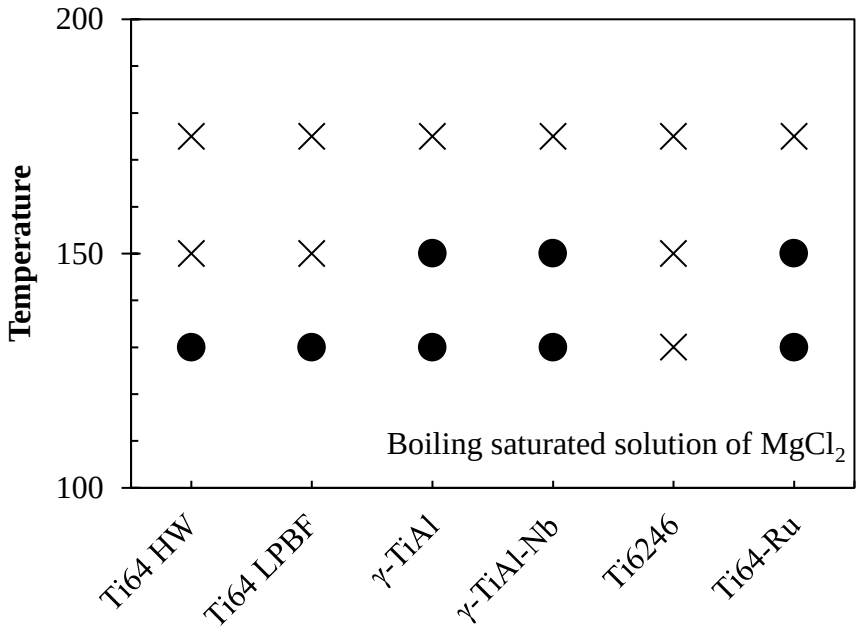

Figure 59 - Results of boiling $MgCl_2$ immersion tests. ● indicate the absence of detectable pitting, while x denotes the occurrence of localized attacks.

8.4 Conclusion

This study investigated the effects of manufacturing-induced microstructure and alloying elements on corrosion behavior of titanium-based materials for applications in reducing acidic environments. The results are the initial step for the qualification of new materials for AM in a geothermal environment.

LPBF produces Ti-6Al-4V with a higher hardness and a comparable a corrosion behavior than the wrought alloy, confirming the promising potential for aggressive service conditions.

Aluminum was shown to be a detrimental element for the corrosion resistance of titanium-based materials in reducing acidic environments. In fact, titanium aluminides exhibited significantly higher corrosion rates in boiling HCl compared to tested titanium alloys. Nevertheless, the addition of Nb has a beneficial effect by reducing the corrosion rates and by markedly improving the resistance to localized corrosion. In this regard, Ti-48Al-2Cr-8Nb emerges as a promising material for applications in moderately acidic reducing environments.
The LPBF-produced Ti-6Al-2Sn-4Zr-6Mo alloy exhibited the best corrosion resistance in reducing acidic environments, with a performance comparable to Ti-6Al-4V-Ru alloys, highlighting the effectiveness of Mo as a corrosion-resistant alloying element in titanium-based systems.

Conclusions and future perspectives

General conclusions

This doctoral thesis demonstrated the fundamental importance of appropriate material selection for applications in aggressive environments, in order to avoid unexpected failures. It showed that AM can be effectively employed to produce materials for applications in aggressive geothermal environments if proper characterization and qualification is carried out.

As demonstrated by the study on Alloy 625, different AM technologies lead to distinct microstructures and defects, which play a decisive role in governing both mechanical properties and corrosion behavior. The results confirmed that fusion-based AM routes currently represent the most reliable solutions for geothermal applications, while emerging sinter-based technologies still require further optimization before being considered for critical application.

The successful qualification of recycled Alloy 725 further demonstrated that AM can represent a strategic resource for producing new components operating under severe conditions starting from end-of-life materials. Alloy 725 produced through AM proved to exhibit mechanical properties and corrosion behavior comparable to the original material.

Field exposure tests finally validated the integration of these closed-loop materials, as well as future laser cladding applications based on Alloy 625 produced by DED, for components such as turbine blades operating under DwP conditions. These solutions appear particularly attractive not only from a sustainability perspective, but also from an economic standpoint, considering the high cost of specialty alloys used in geothermal applications.

For titanium-based materials, the results highlighted that corrosion resistance in reducing acidic environments is primarily controlled by alloy chemistry rather than by the manufacturing route. For the tests conducted so far, AM did not introduce detrimental effects on titanium alloys when compared to conventional processing. These findings provide a clear framework for the selection of titanium alloys suitable for the most aggressive geothermal conditions.

Limitation of the study

Despite the comprehensive experimental approach adopted in this thesis, some limitations must be acknowledged. The interaction between corrosion and other degradation mechanisms, such as erosion and fatigue, was not systematically investigated. Although these phenomena are highly relevant for geothermal applications, their analysis would require dedicated experimental setups and extended testing campaigns beyond the scope of this thesis.

Field exposure tests were specifically employed to partially overcome the limitations of laboratory-scale testing by evaluating materials under real operating conditions. However, not all newly proposed candidate materials for geothermal applications could be tested in field exposure due to limited availability in the test chamber and constraints associated with the production of dedicated specimens conforming to crevice former and U-bend type B geometries.

These limitations define the boundaries within which the conclusions of this study should be interpreted and highlight the need for further investigations.

Future research and perspectives

Results highlighted that materials produced for AM technologies may have microstructure and properties different from their conventionally produced counterparts, especially when considering new AM technologies. Additional studies are required to create guidelines for additively manufactured materials in aggressive industrial environments.

For Alloy 625, future studies could focus on the characterization of material deposition and repair strategies, with particular attention to potential criticalities associated with the manufacturing of geothermal turbine blades. In this context, a study of erosion–corrosion behavior and its correlation with the expected service life of turbine blades would represent relevant research.

Regarding Alloy 725, further work interests the customization of heat treatment tailored for LPBF-processed material. The rapid cooling results in a high supersaturation of alloying elements making the investigation of direct aging treatments immediately after fabrication particularly attractive.

For titanium-based systems, a primary research step would be a field exposure test on suitable titanium alloys to assess their behavior under the actual operating environments. In addition, an extended experimental campaign involving a broader range of titanium alloys would allow a better understand between alloying elements and resistance to reducing acidic environments. The development of empirical parameters analogous to PREN used for stainless steels could provide valuable tools for material selection in geothermal applications.

Finally, a research topic not addressed within this thesis concerns the study of hydrogen embrittlement mechanisms in titanium alloys. As discussed in Chapter 7, this phenomenon is strongly influenced

by microstructure and phase distribution and so materials produced by AM may exhibit different embrittlement behavior compared to the same material obtained in conventional way.

Appendices

List of figures

Figure 1 - Schematic of a LPBF machine [1]. 4

Figure 2 - Schematic of a DED machine [1]. 5

Figure 3 - Schematic of a MEX machine [1]. 6

Figure 4 - 3D void structure of Alloy 625 produced by MEX [11] 6

Figure 5 - Schematic of a typical BJ machine [1]. 7

Figure 6 - Effect of alloying elements on phase diagram of titanium alloys [69] 18

Figure 7 - Pseudo-binary section through a β isomorphous phase diagram [69] 19

Figure 8 - Pourbaix diagram for the titanium-water system at 25°C [76] 20

Figure 9 - Classification of titanium alloys for reducing environments from ASTM B 348 21

Figure 10 - Relationships between powder properties, bulk powder behavior, powder performance in process and the manufactured part quality *[112]* 26

Figure 11 - Images of ex-service turbine blades 31

Figure 12 - Details of degradation in turbine blades. A, B) craters of corrosion-erosion of component made in Alloy 725 and C, D, E) craters of corrosion-erosion and cracks of SCC of component made in Alloy 718 33

Figure 13 – A) Cross-sectional FESEM micrograph showing a crack in an Alloy 718 turbine blade; B) EDS analysis of corrosion products inside the crack; C) FESEM fracture surface of cracks in the Alloy 718 turbine blade. 34

Figure 14 - Cross-sectional micrograph of the pressure side of the components made with alloy A) 718 and B) 725. 34

Figure 15 - Effect of nickel content and PREN value on A) pitting and B) SCC in geothermal fluid at 150 °C and 5 bar, figure adapted from Cabrini et Al. [25] 35

Figure 16 – A, B) Representative microstructures of Alloy 718; C) EDS line scan performed across precipitates in Alloy 718; D, E) Representative microstructures of Alloy 725; F) EDS elemental maps of precipitates in Alloy 725. 37

Figure 17 - XRD analysis of turbine blade in Alloy 718 and 725 38

Figure 18 - Cross section of alloy A) 718 and B) 725 tested according to ASTM G28-A.....39

Figure 19 - Cross section of MEX-manufactured specimen showing macro-defects.....47

Figure 20 - Microstructures of the LPBF (a), DED (b), MEX (c), HW (d) and BJ (e) specimens adapted from Carrozza et Al.[11]. 48

Figure 21 - XRD analysis of Alloy 625 obtained by means of BJ.....49

Figure 22 - HV1 test for the AM-processed specimens (the horizontal lines represent the average values) adapted from Carrozza et Al. [11].....51

Figure 23 - Corrosion rates and maximum attack penetration after ASTM G 28-A tests on Alloy 625 produced by means of different AM techniques. LPBF data from [170] and DED data from [11] 51

Figure 24 - Cross section of specimens after ASTM G28-A test produced by different AM techniques. A) LPBF [170] B) DED, C) MEX [11] AND D) BJ 52

Figure 25 – Volta potential map measured under ambient condition using AFM of Alloy 625 produced by means of LPBF A), DED B), MEX C) e BJ D) measured under ambient condition using AFM. The red line refers to the line scan potential profile of E) LPBF, F) DED, G) MEX and H) BJ. 54

Figure 26 - Potentiodynamic polarization curves of Alloy 625 produced by mean of different AM technologies in A) 0.5 M H2SO4 (pH0) and 0.6 M NaCl at B) pH3 and C) pH7. The corresponding values of open circuit potential, breakdown potential, repassivation potential, current density and current density in passivity range are reported respectively in D), E), F), G), H). Image FESEM analysis showing crevice corrosion in sintered based AM are visible in I).....55

Figure 27 - Potentiostatic polarization curves of Alloy 625 produced by mean of different AM technologies in 0.6 M NaCl at A) pH7 and B) pH3. The corresponding values of current density at C) pH7 and D) pH3.....56

Figure 28 - Optical image analysis of exposed surface of Alloy 625 to 50% of H_2SO_4.....58

Figure 29 - FESEM image analysis of exposed surface of Alloy 625 to 50% of H_2SO_4 produced by means of A) HW, B) LPBF, C) DED, D) MEX and E) BJ.....58

Figure 30 - Corrosion rate of Alloy 625 obtained by means of different AM techniques in immersion tests in H_2SO_4 at different temperatures [187].....59

Figure 31 - program of the printing samples for mechanical and corrosion behaviors tests 64

Figure 32 - Metallography at OM of Alloy 725 in different manufacturing and heat treatment conditions. A) Forged B) Forged and precipitation hardened C) LPBF D) LPBF and precipitation hardened 67

Figure 33 - FESEM micrographs of microstructure of Alloy 725 in different manufacturing and heat treatment conditions. A) Forged B) Forged and precipitation hardened C) LPBF D) LPBF and precipitation hardened 68

Figure 34 – XRD analysis of Alloy 725 in different conditions. A) Forged, B) Forrged + PH, C) LPBF and D) LPBF + PH 69

Figure 35 – FESEM cross-section micrographs of Alloy 725 specimens after ASTM G28A intergranular corrosion testing in different manufacturing and heat treatment conditions. 73

Figure 36 - The Bode plots for passive films of Alloy 725 in 0.6 M NaCl acidified to pH 3 at 40 °C 74

Figure 37 – Potentiodynamics polarization test of Alloy 725 in 0.6 M NaCl acidified to pH 3 at 40 °C 75

Figure 38 - Assembly diagram of the A) Crevice and B) U-bend specimens on the plate 79

Figure 39 - Specimen plate with mounted samples after the field exposure test 80

Figure 40 - FESEM micrography of Crevice specimen in X5CrNiMo12-6-1.5. A) Surface image after cleaning B) Cross section 81

Figure 41 - Digital optical image of crevice specimen made of Alloy 725 produced by forging and precipitation hardened. Red arrows underline under-deposit corrosion. 82

Figure 42 - FESEM image of under-deposit corrosion of A), B) Alloy 725, C), D) Alloy 725 LPBF, E), F) Alloy 725 LPBF PH and G), H) Alloy 625 DED. 83

Figure 43 - Cross section of crevice specimen in Alloy 725 produced by LPBF and precipitation hardened 84

Figure 44 - U-bend in X5CrNiMo12-6-1.5 after the exposure test. A) OM micrograph B) Cross section 85

Figure 45- Heat exchanger tube along the fracture a) Reconstruction of the entire fracture using digital optical microscope b), c) Details 87

Figure 46- Simplified diagram of the heat exchanger 89

Figure 47 - Classification of the different fracture zones. A) Axial break section along the edge of the weld seam, B) Branching and C) Secondary cracks 91

Figure 48 – Images of deposits and particles at the tube side (images A, B and C)) and respective EDS spectrum (D, E and F) 92

Figure 49 - EDS analysis of a cross section of the fracture of the damaged tube..... 92

Figure 50 - Metallography of the tube in A) Fusion zone, B) Heat affected zone and C) Base metal 94

Figure 51- Cross section of the tube. A) FESEM image of polished surface B) Optical image after lactic reagent's attack to detect titanium hydrides 95

Figure 52- Fracture analysis of the tube in the fusion zone and in the base metal 96

Figure 53 - Hydrogen content in the titanium tube..... 98

Figure 54 – Microstructures of the investigated materials: A) Ti-6Al-4V HW, B) Ti-6Al-4V LPBF, C) Ti-48Al-2Cr-2Nb [231], D) Ti-48Al-2Cr-8Nb [232], E) Ti-6Al-2Sn-4Zr-6Mo F) Ti-6Al-4V-Ru. 106

Figure 55 - Vickers hardness (HV1) of the investigated materials. Dots represent individual measurements, while horizontal bars indicate mean values. 108

Figure 56 - Surface morphology of the investigated materials after immersion in boiling HCl at pH0: A) Ti-6Al-4V HW, B) Ti-6Al-4V LPBF, C) Ti-48Al-2Cr-2Nb, D) Ti-48Al-2Cr-8Nb, E) Ti-6Al-2Sn-4Zr-6Mo F) Ti-6Al-4V-Ru. 109

Figure 57 - OM micrograph of localized attack on Ti-6Al-4V after an immersion tests in a boiling solution of $MgCl_2$..... 111

Figure 58 - FESEM micrographs of pitting corrosion morphologies observed on the investigated materials after immersion in boiling $MgCl_2$ solution. A) Ti-6Al-4V HW at 150°C, B) Ti-6Al-4V LPBF at 150°C, C) Ti-48Al-2Cr-2Nb at 130°C, D) Ti-48Al-2Cr-8Nb at 175°C, E) Ti-6Al-2Sn-4Zr-6Mo at 175°C F) Ti-6Al-4V-Ru at 175°C. 112

Figure 59 - Results of boiling $MgCl_2$ immersion tests. ● indicate the absence of detectable pitting, while x denotes the occurrence of localized attacks. 113

.....

List of tables

Table 1 - Composition of Alloy 718 and 725 following ASTM standards.....31

Table 2 - Chemical composition of the studied materials.....43

Table 3 – Volumetric porosity and relative fraction pores with Feret diameter higher than 50 µm .46

Table 4 - Grain size of specimen produced by MEX and BJ following ASTM E 112.....52

Table 5 - Weight loss and corrosion rates of Alloy 625 produced by different technologies after 24 h immersion in 50 wt.% H_2SO_4 at 50 °C, 80 °C, and boiling temperature. 57

Table 6 – Mean value and deviation standard of chemical composition of ex-service turbine blade made of Inconel 725 (wt%).....61

Table 7 - Chemical composition of the Inconel 725 recycled powder (wt%) 62

Table 8 - LPBF process parameters used for the design of experiments and relative material characteristics.....63

Table 9 - Hardness (HRC) of Alloy 725 for different processing and heat treatment conditions. 70

Table 10 - Tensile properties of LPBF-manufactured Alloy 725 and comparison with ASTM B805 standard. 70

Table 11 - Corrosion rates of Alloy 725 after ASTM G28-A.....72

Table 12 – summary table of materials.....78

Table 13 - Summary table of mass loss measurements 81

Table 14 - Chemical analysis of steam condensation and liquid (water in the shell) of the heat exchanger 87

Table 15 - Chemical composition of tube after the service 89

Table 16 – Material considered in this study 101

Table 17 – Chemical composition of titanium alloys tested.....103

Table 18 - Corrosion rate of the investigated materials in boiling HCl solutions at pH0 and pH1. 110

Bibliography

[1] **M. Armstrong, H. Mehrabi, N. Naveed, An overview of modern metal additive manufacturing technology, J. Manuf. Process. 84 (2022) 1001–1029. https://doi.org/10.1016/J.JMAPRO.2022.10.060.**

[2] **A. Vafadar, F. Guzzomi, A. Rassau, K. Hayward, Advances in Metal Additive Manufacturing: A Review of Common Processes, Industrial Applications, and Current Challenges, Applied Sciences 2021, Vol. 11, 11 (2021) 1–33. https://doi.org/10.3390/APP11031213.**

[3] **W.E. Frazier, Metal additive manufacturing: A review, J. Mater. Eng. Perform. 23 (2014) 1917–1928. https://doi.org/10.1007/S11665-014-0958-Z/FIGURES/9.**

[4] **M. Karmuhilan, S. Kumanan, A Review on Additive Manufacturing Processes of Inconel 625, J. Mater. Eng. Perform. 31 (2022) 2583–2592. https://doi.org/10.1007/S11665-021-06427-3/TABLES/5.**

[5] **D.G. Ahn, Directed Energy Deposition (DED) Process: State of the Art, International Journal of Precision Engineering and Manufacturing-Green Technology 2021 8:2 8 (2021) 703–742. https://doi.org/10.1007/S40684-020-00302-7.**

[6] **A. Saboori, A. Aversa, G. Marchese, S. Biamino, M. Lombardi, P. Fino, A. Saboori, A. Aversa, G. Marchese, S. Biamino, M. Lombardi, P. Fino, Application of Directed Energy Deposition-Based Additive Manufacturing in Repair, Applied Sciences 2019, Vol. 9, 9 (2019). https://doi.org/10.3390/APP9163316.**

[7] **F. Zafar, O. Emadinia, J. Conceição, M. Vieira, A. Reis, A Review on Direct Laser Deposition of Inconel 625 and Inconel 625-Based Composites—Challenges and Prospects, Metals 2023, Vol. 13, Page 787 13 (2023) 787. https://doi.org/10.3390/MET13040787.**

[8] **M. Li, W. Du, A. Elwany, Z. Pei, C. Ma, Metal binder jetting additive manufacturing: A literature review, Journal of Manufacturing Science and Engineering, Transactions of the ASME 142 (2020). https://doi.org/10.1115/1.4047430/1084395.**

[9] **K. Jasik, L. Śnieżek, J. Kluczyński, K. Jasik, L. Śnieżek, J. Kluczyński, Additive Manufacturing of Metals Using the MEX Method: Process Characteristics and**

Performance Properties—A Review, Materials 2025, Vol. 18, 18 (2025) 2744. https://doi.org/10.3390/MA18122744.

[10] Y. Thompson, J. Gonzalez-Gutierrez, C. Kukla, P. Felfer, Fused filament fabrication, debinding and sintering as a low cost additive manufacturing method of 316L stainless steel, Addit. Manuf. 30 (2019) 100861. https://doi.org/10.1016/J.ADDMA.2019.100861.

[11] A. Carrozza, S. Lorenzi, F. Carugo, S. Fest-Santini, M. Santini, G. Marchese, G. Barbieri, F. Cognini, M. Cabrini, T. Pastore, A comparative analysis between material extrusion and other additive manufacturing techniques: Defects, microstructure and corrosion behavior in nickel alloy 625, Mater. Des. 225 (2023) 111545. https://doi.org/10.1016/J.MATDES.2022.111545.

[12] S. Lorenzi, G. D'Urso, L. Nani, M. Quarto, S. Fest-Santini, T. Pastore, Effect of the deposition strategy and endogenous defect pattern on the plastic deformability and the fracture mechanism of 316L stainless steel obtained using material extrusion, Eng. Fail. Anal. 171 (2025) 109395. https://doi.org/10.1016/J.ENGFAILANAL.2025.109395.

[13] Y. Lee, P. Nandwana, S. Simunovic, Powder spreading, densification, and part deformation in binder jetting additive manufacturing, Progress in Additive Manufacturing 2021 7:1 7 (2021) 111–125. https://doi.org/10.1007/S40964-021-00214-1.

[14] S. Mirzababaei, S. Pasebani, S. Mirzababaei, S. Pasebani, A Review on Binder Jet Additive Manufacturing of 316L Stainless Steel, Journal of Manufacturing and Materials Processing 2019, Vol. 3, 3 (2019). https://doi.org/10.3390/JMMP3030082.

[15] D. Huber, L. Vogel, A. Fischer, The effects of sintering temperature and hold time on densification, mechanical properties and microstructural characteristics of binder jet 3D printed 17-4 PH stainless steel, Addit. Manuf. 46 (2021) 102114. https://doi.org/10.1016/J.ADDMA.2021.102114.

[16] Q. Porter, Z. Pei, C. Ma, Binder Jetting and Infiltration of Metal Matrix Nanocomposites, J. Manuf. Sci. Eng. 144 (2022). https://doi.org/10.1115/1.4053156/1129060.

[17] E. Pei, G.H. Loh, Future challenges in functionally graded additive manufacturing, Additive Manufacturing - Developments in Training and Education (2018) 219–228. https://doi.org/10.1007/978-3-319-76084-1_15/FIGURES/2.

[18] N. Knofius, M.C. van der Heijden, W.H.M. Zijm, Consolidating spare parts for asset maintenance with additive manufacturing, Int. J. Prod. Econ. 208 (2019) 269–280. https://doi.org/10.1016/J.IJPE.2018.11.007.

[19] J.C. Najmon, S. Raeisi, A. Tovar, Review of additive manufacturing technologies and applications in the aerospace industry, Additive Manufacturing for the Aerospace Industry (2019) 7–31. https://doi.org/10.1016/B978-0-12-814062-8.00002-9.

[20] S. Talib, S. Gupta, V. Chaudhary, P. Gupta, M.A. Wahid, Additive manufacturing: Materials, techniques and biomedical applications, Mater. Today Proc. 46 (2021) 6847–6851. https://doi.org/10.1016/J.MATPR.2021.04.438.

[21] M.H. Dickson, M. Fanelli, Geothermal background, in: M.H. Dickson, M. Fanelli (Eds.), Geothermal Energy: Utilization and Technology, 2003.

[22] M. El Haj Assad, E. Bani-Hani, M. Khalil, Performance of geothermal power plants (single, dual, and binary) to compensate for LHC-CERN power consumption: comparative study, Geothermal Energy 5 (2017) 1–16. https://doi.org/10.1186/S40517-017-0074-Z/FIGURES/18.

[23] F. Brownlie, T. Hodgkiess, A. Pearson, A.M. Galloway, A study on the erosion-corrosion behaviour of engineering materials used in the geothermal industry, Wear 477 (2021) 203821. https://doi.org/10.1016/J.WEAR.2021.203821.

[24] P. Iberl, N.S.A. Alt, E. Schluecker, Evaluation of corrosion of materials for application in geothermal systems in Central Europe, Materials and Corrosion 66 (2015) 733–755. https://doi.org/10.1002/MACO.201407864.

[25] M. Cabrini, S. Lorenzi, T. Pastore, M. Favilla, R. Perini, B. Tarquini, Materials selection for dew-point corrosion in geothermal fluids containing acid chloride, Geothermics 69 (2017) 139–144.

[26] G. Allegrini, G. Benvenuti, Corrosion characteristics and geothermal power plant protection (collateral processes of abrasion, erosion and scaling), Geothermics (1970) 2462–2466.

[27] P. Hirtz, C. Buck, R. Kunzman, Current techniques in acid-chloride corrosion control and monitoring at The Geysers, (1991).

[28] S. Hjartarson, G. Saevarsdóttir, H. Pálsson, K. Ingason, B. Pálsson, W. Harvey, Utilization of CHloride Bearing, Superheated Steam, Georg.Cluster.IsS Hjartarson, G Sævarsdóttir, H Pálsson, K Ingason, B Pálsson, W HarveyWorkshop on Geothermal Reservoir Engineering. Standford, California,

2012•georg.Cluster.Is (n.d.). https://georg.cluster.is/wp-content/uploads/2016/12/utilization-of-chloride-bearing-superheated-steam.pdf (accessed May 20, 2025).

[29] C. Penot, D. Martelo, S. Paul, C. Penot, D. Martelo, S. Paul, Corrosion and Scaling in Geothermal Heat Exchangers, Applied Sciences 2023, Vol. 13, 13 (2023). https://doi.org/10.3390/APP132011549.

[30] S.N. Karlsdóttir, Corrosion, scaling and material selection in geothermal power production, Comprehensive Renewable Energy 7 (2012) 241–259. https://doi.org/10.1016/B978-0-08-087872-0.00706-X.

[31] K. Hassani, W. Zheng, A review of recent advances in mineral scaling in geothermal energy systems: mechanisms, mitigation, and case studies, Environmental Earth Sciences 2025 84:14 84 (2025) 418-. https://doi.org/10.1007/S12665-025-12416-9.

[32] T. Kaya, P. Hoshan, Corrosion and Material Selection for Geothermal Systems, in: Materials science (Ed.), Proceedings World Geothermal Congress, Antalya, Turkey, 2005: pp. 24–29. https://www.academia.edu/69353632/Corrosion_and_Material_Selection_for_Geothermal_Systems.

[33] L.R. Miller, Chemistry and Materials in Geothermal Systemns, in: T.P. LA Casper (Ed.), Geothermal Scaling and Corrosion, ASTM International, 1980. https://doi.org/https://doi.org/10.1520/STP30061S.

[34] C. Penot, D. Martelo, S. Paul, Corrosion and Scaling in Geothermal Heat Exchangers, Applied Sciences 2023 13 (2023) 11549. https://doi.org/10.3390/APP132011549.

[35] P.H. Tevfik KAYA, Corrosion and Material Selection for Geothermal Systems, Proceedings World Geothermal Congress 2005 Antalya, Turkey, 24-29 April 2005 (n.d.).

[36] M. Conover, P. Ellis, A. Curzon, Material selection guidelines for geothermal power systems: An overview, ASTM Special Technical Publications STP 717 (1980) 24–40. https://doi.org/10.1520/STP30063S.

[37] C.L. Briant, Z.F. Wang, N. Chollocoop, Hydrogen embrittlement of commercial purity titanium, Corros. Sci. 44 (2002) 1875–1888. https://doi.org/10.1016/S0010-938X(01)00159-7.

[38] **E. Tal-Gutelmacher, D. Eliezer, Hydrogen-assisted degradation of titanium based alloys, Mater. Trans. 45 (2004) 1594–1600. https://doi.org/10.2320/MATERTRANS.45.1594.**

[39] **D.S. Shih, I.M. Robertson, H.K. Birnbaum, Hydrogen embrittlement of α titanium: In situ tem studies, Acta Metallurgica 36 (1988) 111–124. https://doi.org/10.1016/0001-6160(88)90032-6.**

[40] **T.C. Dzogbewu, D.J. de Beer, Additive manufacturing of selected ecofriendly energy devices, Virtual Phys. Prototyp. 18 (2023). https://doi.org/10.1080/17452759.2023.2276245.**

[41] **J.I. Arrizubieta, O. Ukar, M. Ostolaza, A. Mugica, Study of the Environmental Implications of Using Metal Powder in Additive Manufacturing and Its Handling, Metals 2020, Vol. 10, 10 (2020). https://doi.org/10.3390/MET10020261.**

[42] **Y. Polsky, K. Armstrong, C. Price, J.-C. Su, A. Wang, S. Porse, Study of Additive Manufacturing Application to Geothermal Technologies, (2020).**

[43] **C. Price, K. Armstrong, Y. Polsky, A. Wang, S. Nimbalkar, P. Chesser, B. Post, J.C. Su, A techno-economic framework for comparing conventionally and additively manufactured parts for geothermal applications, J. Manuf. Process. 72 (2021) 458–468. https://doi.org/10.1016/J.JMAPRO.2021.10.028.**

[44] **M. Kabirnajafi, T. Gemeda, W. Demisse, S. Estrada, L. Wang, J. Xu, Design and development of a novel additively manufactured geothermal heat exchanger, Int. J. Energy Res. 46 (2022) 3335–3348. https://doi.org/10.1002/ER.7384;SUBPAGE:STRING:FULL.**

[45] **A.S. Sabau, A. Bejan, D. Brownell, K. Gluesenkamp, B. Murphy, F. List, K. Carver, C.R. Schaich, J.W. Klett, Design, additive manufacturing, and performance of heat exchanger with a novel flow-path architecture, Appl. Therm. Eng. 180 (2020) 115775. https://doi.org/10.1016/J.APPLTHERMALENG.2020.115775.**

[46] **I.A. Ferreira, R. Godina, H. Carvalho, Waste Valorization through Additive Manufacturing in an Industrial Symbiosis Setting, Sustainability 2021, Vol. 13, 13 (2020) 1–21. https://doi.org/10.3390/SU13010234.**

[47] **V. Tebaldo, G. Gautier di Confiengo, D. Duraccio, M.G. Faga, Sustainable Recovery of Titanium Alloy: From Waste to Feedstock for Additive Manufacturing, Sustainability 2024, Vol. 16, 16 (2023). https://doi.org/10.3390/SU16010330.**

[48] **F. Walachowicz, I. Bernsdorf, U. Papenfuss, C. Zeller, A. Graichen, V. Navrotsky, N. Rajvanshi, C. Kiener, Comparative Energy, Resource and Recycling Lifecycle Analysis of the Industrial Repair Process of Gas Turbine Burners Using Conventional Machining and Additive Manufacturing, J. Ind. Ecol. 21 (2017) S203–S215. https://doi.org/10.1111/JIEC.12637;CSUBTYPE:STRING:SPECIAL;PAGE:STRING:ARTICLE/CHAPTER.**

[49] **M.S. Kenevisi, F.S. Gobber, P. Fino, M. Lombardi, F. Bondioli, S. Biamino, D. Ugues, Tool steels and their additive manufacturing for fabrication and repair via PBF and DED processes: techniques, challenges, and applications, Mater. Des. 258 (2025) 114639. https://doi.org/10.1016/J.MATDES.2025.114639.**

[50] **R. Blaha, J. Hajnys, J. Mesicek, A. Mechali, D. Krisak, M. Pagac, Review of Directed Energy Deposition (DED) in Component Repair, Lecture Notes in Networks and Systems 1062 LNNS (2024) 197–205. https://doi.org/10.1007/978-3-031-65656-9_20/FIGURES/3.**

[51] **J. Bennett, D. Garcia, M. Kendrick, T. Hartman, G. Hyatt, K. Ehmann, F. You, J. Cao, Repairing Automotive Dies with Directed Energy Deposition: Industrial Application and Life Cycle Analysis, Journal of Manufacturing Science and Engineering, Transactions of the ASME 141 (2019). https://doi.org/10.1115/1.4042078/477557.**

[52] **K. Raoufi, S. Badwe, K.R. Haapala, Improvement of Environmental Performance of Nickel Powder Production Through Material Circularity, (2025). https://doi.org/10.1115/DETC2025-169128.**

[53] **M.J. Donachie, S.J. Donachie, Superalloys: A Technical Guide, Superalloys (2002). https://doi.org/10.31399/ASM.TB.STG2.9781627082679.**

[54] **N.M. Dawood, A.M. Salim, A Review on Characterization, Classifications, and Applications of Super Alloys, Journal of University of Babylon for Engineering Sciences (2021) 53–62. https://mail.journalofbabylon.com/index.php/JUBES/article/view/3505 (accessed January 27, 2026).**

[55] **A.K. Jena, M.C. Chaturvedi, The role of alloying elements in the design of nickel-base superalloys, J. Mater. Sci. 19 (1984) 3121–3139. https://doi.org/10.1007/BF00549796/METRICS.**

[56] C.T. Sims, A contemporary view of nickel-base superalloys, JOM 1966 18:10 18 (2017) 1119–1130. https://doi.org/10.1007/BF03378505.

[57] G.R. Thellaputta, P.S. Chandra, C.S.P. Rao, Machinability of Nickel Based Superalloys: A Review, Mater. Today Proc. 4 (2017) 3712–3721. https://doi.org/10.1016/J.MATPR.2017.02.266.

[58] S. Bell, M. de Bruyn, T. Steinberg, G. Will, C-276 nickel alloy corrosion in eutectic Na2CO3/NaCl molten salt under isothermal and thermal cycling conditions, Solar Energy Materials and Solar Cells 240 (2022) 111695. https://doi.org/10.1016/J.SOLMAT.2022.111695.

[59] G.D. Smith, B.A. Baker, Nickel and Its Alloys, Mechanical Engineers' Handbook 1 (2005) 256–277. https://doi.org/10.1002/0471777447.CH6.

[60] A.I. Thorhallsson, A. Stefansson, D. Kovalov, S.N. Karlsdottir, Corrosion testing of materials in simulated superheated geothermal environment, Corros. Sci. 168 (2020) 108584. https://doi.org/10.1016/J.CORSCI.2020.108584.

[61] S.N. Karlsdottir, K.R. Ragnarsdottir, I.O. Thorbjornsson, A. Einarsson, Corrosion testing in superheated geothermal steam in Iceland, Geothermics 53 (2015) 281–290. https://doi.org/10.1016/J.GEOTHERMICS.2014.06.007.

[62] R.D. McCright, Corrosion Behavior of Materials Exposed to Hypersaline Geothermal Brine, (1981) 1–10. https://doi.org/10.5006/C1981-81228.

[63] R. Bäßler, J. Sobetzki, H.S. Klapper, Corrosion Resistance of High-Alloyed Materials in Artificial Geothermal Fluids, CORROSION 2013 (2013) 1–8. https://doi.org/10.5006/C2013-02327.

[64] H.S. Klapper, R. Baessler, K. Weidauer, D. Stuerzbecher, Evaluation of Suitability of High-Alloyed Materials for Geothermal Applications in the North German Basin, Corrosion 68 (2012) 016001–1. https://doi.org/10.5006/1.3676631.

[65] B.C. Krogh, H. Husby, B. Nyhus, Laboratory Testing of Corrosion Resistant Alloys in Deep Geothermal Well Environment, (2021) 1–15. https://doi.org/10.5006/C2021-16693.

[66] M. Conover, P. Ellis, A. Curzon, Material Selection Guidelines for Geothermal Power Systems—An Overview, ASTM Special Technical Publication STP 717 (1980) 24–40. https://doi.org/10.1520/STP30063S.

[67] H.S. Klapper, M.M. Baker, M.P. Baker, Scaling and corrosion behavior of metallic materials after long-Term exposure to the geothermal fluid of the north German

basin, NACE - International Corrosion Conference Series 5 (2016) 3470–3478. https://doi.org/10.5006/C2016-07644/57490.

[68] C. Cui, B.M. Hu, L. Zhao, S. Liu, Titanium alloy production technology, market prospects and industry development, Mater. Des. 32 (2011) 1684–1691. https://doi.org/10.1016/J.MATDES.2010.09.011.

[69] G. Lütjering, Titanium. 2nd ed., Springer, 2007.

[70] W. Gerhard, Materials Properties Handbook : Titanium Alloys, in: R. Boyer (Ed.), ASM International, 1993: pp. 192–198.

[71] I.J. Polmear, Light alloys : from traditional alloys to nanocrystals, (2006) 421.

[72] P. Barriobero-Vila, G. Requena, F. Warchomicka, A. Stark, N. Schell, T. Buslaps, Phase transformation kinetics during continuous heating of a β-quenched Ti–10V–2Fe–3Al alloy, J. Mater. Sci. 50 (2015) 1412–1426. https://doi.org/10.1007/S10853-014-8701-6.

[73] F. Hua, K. Mon, P. Pasupathi, G. Gordon, D. Shoesmith, A review of corrosion of titanium grade 7 and other titanium alloys in nuclear waste repository environments, Corrosion 61 (2005) 987–1003. https://doi.org/10.5006/1.3280899.

[74] ASM, ASM handbook Volume 2 - Properties and selection: Nonferrous alloys and special-purpose materials, ASM Metals Handbook 2 (1993) 1300. https://www.asminternational.org/asm-handbook-volume-2-properties-and-selection-nonferrous-alloys-and-special-purpose-materials/results/-/journal_content/56/06182G/PUBLICATION/ (accessed July 20, 2023).

[75] R.W. Schutz, Ruthenium Enhanced Titanium Alloys, (n.d.).

[76] ASM, ASM Handbook Volume 13: Corrosion, ASM Metals Handbook (2003) 1–1135. https://www.asminternational.org/asm-handbook-volume-13a-corrosion-fundamentals-testing-and-protection/results/-/journal_content/56/06494G/PUBLICATION/ (accessed July 20, 2023).

[77] ASTM, B348/B348M Standard Specification for Titanium and Titanium Alloy Bars and Billets, (n.d.). https://www.astm.org/b0348_b0348m-21.html (accessed July 24, 2023).

[78] R. W. Schutz and M. Xiao, ENHANCING CORROSION RESISTANCE OF THE Ti-3Al-8V-6Cr-4Zr-4Mo (Beta-CTM) ALLOY FOR INDUSTRIAL APPLICATIONS, RMI Titanium Company (n.d.).

[79] Q. Liu, H. Liu, J. Xie, W. fu Zhang, Y. ming Zhang, C. Feng, G. shan Li, Y. Yu, S. yin Song, C. xian Yin, Influence of Ru on structure and corrosion behavior of

passive film on Ti-6Al-4V alloy in oil and gas exploration conditions, Scientific Reports 2022 12:1 12 (2022) 1–17. https://doi.org/10.1038/s41598-022-21047-0.

[80] Y. Okazaki, Y. Ito, K. Kyo, T. Tateishi, A Corrosion resistance and corrosion fatigue strength of new titanium alloys for medical implants without V and A1, ~Iaterials Science and Engineering 213 (1996) 138–147.

[81] Z.B. Wang, H.X. Hu, Y.G. Zheng, W. Ke, Y.X. Qiao, Comparison of the corrosion behavior of pure titanium and its alloys in fluoride-containing sulfuric acid, Corros. Sci. 103 (2016) 50–65. https://doi.org/10.1016/J.CORSCI.2015.11.003.

[82] B.B. Straumal, A. Korneva, A.R. Kilmametov, L. Lityńska-Dobrzyńska, A.S. Gornakova, R. Chulist, M.I. Karpov, P. Zięba, Structural and Mechanical Properties of Ti–Co Alloys Treated by High Pressure Torsion, Materials 12 (2019). https://doi.org/10.3390/MA12030426.

[83] D. Gu, Y.C. Hagedorn, W. Meiners, G. Meng, R.J.S. Batista, K. Wissenbach, R. Poprawe, Densification behavior, microstructure evolution, and wear performance of selective laser melting processed commercially pure titanium, Acta Mater. 60 (2012) 3849–3860. https://doi.org/10.1016/J.ACTAMAT.2012.04.006.

[84] H. Attar, M. Calin, L.C. Zhang, S. Scudino, J. Eckert, Manufacture by selective laser melting and mechanical behavior of commercially pure titanium, Materials Science and Engineering: A 593 (2014) 170–177. https://doi.org/10.1016/J.MSEA.2013.11.038.

[85] H. Attar, S. Ehtemam-Haghighi, D. Kent, X. Wu, M.S. Dargusch, Comparative study of commercially pure titanium produced by laser engineered net shaping, selective laser melting and casting processes, Materials Science and Engineering: A 705 (2017) 385–393. https://doi.org/10.1016/J.MSEA.2017.08.103.

[86] T. Zhang, C.T. Liu, Design of titanium alloys by additive manufacturing: A critical review, Advanced Powder Materials 1 (2022) 100014. https://doi.org/10.1016/J.APMATE.2021.11.001.

[87] F. Bartolomeu, M. Gasik, F.S. Silva, G. Miranda, Mechanical Properties of Ti6Al4V Fabricated by Laser Powder Bed Fusion: A Review Focused on the Processing and Microstructural Parameters Influence on the Final Properties, Metals 2022, Vol. 12, Page 986 12 (2022) 986. https://doi.org/10.3390/MET12060986.

[88] N. Kazantseva, P. Krakhmalev, M. Thuvander, I. Yadroitsev, N. Vinogradova, I. Ezhov, Martensitic transformations in Ti-6Al-4V (ELI) alloy manufactured by 3D

Printing, Mater. Charact. 146 (2018) 101–112. https://doi.org/10.1016/J.MATCHAR.2018.09.042.

[89] S. Cao, Y. Zou, C.V.S. Lim, X. Wu, S. Cao, Y. Zou, C.V.S. Lim, X. Wu, Review of laser powder bed fusion (LPBF) fabricated Ti-6Al-4V: process, post-process treatment, microstructure, and property, Light: Advanced Manufacturing 2 (2021) 313–332. https://doi.org/10.37188/LAM.2021.020.

[90] J.C. Colombo-Pulgarín, C.A. Biffi, M. Vedani, D. Celentano, A. Sánchez-Egea, A.D. Boccardo, J.P. Ponthot, Beta Titanium Alloys Processed By Laser Powder Bed Fusion: A Review, Journal of Materials Engineering and Performance 2021 30:9 30 (2021) 6365–6388. https://doi.org/10.1007/S11665-021-05800-6.

[91] A. Carrozza, A. Aversa, P. Fino, M. Lombardi, A study on the microstructure and mechanical properties of the Ti-6Al-2Sn-4Zr-6Mo alloy produced via Laser Powder Bed Fusion, J. Alloys Compd. 870 (2021) 159329. https://doi.org/10.1016/J.JALLCOM.2021.159329.

[92] A. Carrozza, A. Aversa, P. Fino, M. Lombardi, Towards customized heat treatments and mechanical properties in the LPBF-processed Ti-6Al-2Sn-4Zr-6Mo alloy, Mater. Des. 215 (2022) 110512. https://doi.org/10.1016/J.MATDES.2022.110512.

[93] H. Peng, S. Wu, W.H. Kan, S.C.V. Lim, Y. Zhu, A. Huang, Rapid hardening response of ultra-hard Ti-6Al-2Sn-4Zr-6Mo alloy produced by laser powder bed fusion, Scr. Mater. 226 (2023) 115209. https://doi.org/10.1016/J.SCRIPTAMAT.2022.115209.

[94] H. Hassanin, Y. Zweiri, L. Finet, K. Essa, C. Qiu, M. Attallah, Laser Powder Bed Fusion of Ti-6Al-2Sn-4Zr-6Mo Alloy and Properties Prediction Using Deep Learning Approaches, Materials 2021, Vol. 14, Page 2056 14 (2021) 2056. https://doi.org/10.3390/MA14082056.

[95] T. Ishimoto, K. Hagihara, K. Hisamoto, S.H. Sun, T. Nakano, Crystallographic texture control of beta-type Ti–15Mo–5Zr–3Al alloy by selective laser melting for the development of novel implants with a biocompatible low Young's modulus, Scr. Mater. 132 (2017) 34–38. https://doi.org/10.1016/J.SCRIPTAMAT.2016.12.038.

[96] S.H. Sun, K. Hagihara, T. Ishimoto, R. Suganuma, Y.F. Xue, T. Nakano, Comparison of microstructure, crystallographic texture, and mechanical properties in Ti–15Mo–5Zr–3Al alloys fabricated via electron and laser beam

powder bed fusion technologies, Addit. Manuf. 47 (2021) 102329. https://doi.org/10.1016/J.ADDMA.2021.102329.

[97] A. Takase, T. Ishimoto, R. Suganuma, T. Nakano, Lattice distortion in selective laser melting (SLM)-manufactured unstable β-type Ti-15Mo-5Zr-3Al alloy analyzed by high-precision X-ray diffractometry, Scr. Mater. 201 (2021) 113953. https://doi.org/10.1016/J.SCRIPTAMAT.2021.113953.

[98] A. Takase, T. Ishimoto, R. Suganuma, T. Nakano, Surface residual stress and phase stability in unstable β-type Ti–15Mo–5Zr–3Al alloy manufactured by laser and electron beam powder bed fusion technologies, Addit. Manuf. 47 (2021) 102257. https://doi.org/10.1016/J.ADDMA.2021.102257.

[99] M. Mizuno, K. Sugita, K. Do, T. Ishimoto, T. Nakano, H. Araki, Stability of vacancies in β-type Ti-15Mo-5Zr-3Al alloy fabricated via laser powder bed fusion, Additive Manufacturing Letters 7 (2023) 100162. https://doi.org/10.1016/J.ADDLET.2023.100162.

[100] M.A. Macias-Sifuentes, C. Xu, O. Sanchez-Mata, S.Y. Kwon, S.E. Atabay, J.A. Muñiz-Lerma, M. Brochu, Microstructure and mechanical properties of β-21S Ti alloy fabricated through laser powder bed fusion, Progress in Additive Manufacturing 6 (2021) 417–430. https://doi.org/10.1007/S40964-021-00181-7/FIGURES/16.

[101] M. Pellizzari, A. Jam, M. Tschon, M. Fini, C. Lora, M. Benedetti, A 3D-Printed Ultra-Low Young's Modulus β-Ti Alloy for Biomedical Applications, Materials 2020, Vol. 13, Page 2792 13 (2020) 2792. https://doi.org/10.3390/MA13122792.

[102] M. Pellizzari, A. Jam, V. Tonon, M. Benedetti, C. Lora, Ageing behavior of Beta-Ti21S produced by laser powder bed fusion, (n.d.) 42.

[103] A. Jam, M. Pellizzari, L. Emanuelli, G. Valsecchi, A. du Plessis, M. Benedetti, Influence of heat treatment on the mechanical performance of Ti21S octet truss lattice structure fabricated by laser powder bed fusion, Progress in Additive Manufacturing (2023) 1–11. https://doi.org/10.1007/S40964-023-00494-9/FIGURES/9.

[104] L. Emanuelli, R. De Biasi, A. du Plessis, C. Lora, A. Jam, M. Benedetti, M. Pellizzari, Metrological characterization of porosity graded β-Ti21S triply periodic minimal surface cellular structure manufactured by laser powder bed fusion, Int. J. Bioprint. 9 (2023). https://doi.org/10.18063/IJB.729.

[105] L. Emanuelli, A. Jam, A. du Plessis, C. Lora, R. De Biasi, M. Benedetti, M. Pellizzari, Manufacturability of functionally graded porous β-Ti21S auxetic architected biomaterials produced by laser powder bed fusion: Comparison between 2D and 3D metrological characterization, Int. J. Bioprint. 9 (2023). https://doi.org/10.18063/IJB.728.

[106] C. Madikizela, L.A. Cornish, L.H. Chown, H. Möller, Microstructure and mechanical properties of selective laser melted Ti-3Al-8V-6Cr-4Zr-4Mo compared to Ti-6Al-4V, Materials Science and Engineering: A 747 (2019) 225–231. https://doi.org/10.1016/J.MSEA.2018.12.100.

[107] C. Qiu, A. Fones, H.G.C. Hamilton, N.J.E. Adkins, M.M. Attallah, A new approach to develop palladium-modified Ti-based alloys for biomedical applications, Mater. Des. 109 (2016) 98–111. https://doi.org/10.1016/J.MATDES.2016.07.055.

[108] J.A. Slotwinski, E.J. Garboczi, Metrology Needs for Metal Additive Manufacturing Powders, JOM 67 (2015) 538–543. https://doi.org/10.1007/S11837-014-1290-7/FIGURES/2.

[109] M. Qian, Metal Powder for Additive Manufacturing, JOM 67 (2015) 536–537. https://doi.org/10.1007/S11837-015-1321-Z/METRICS.

[110] C.N. Hulme-Smith, V. Hari, P. Mellin, Spreadability Testing of Powder for Additive Manufacturing, BHM Berg- Und Hüttenmännische Monatshefte 2020 166:1 166 (2021) 9–13. https://doi.org/10.1007/S00501-020-01069-9.

[111] M. Mehrabi, J. Gardy, F.A. Talebi, A. Farshchi, A. Hassanpour, A.E. Bayly, An investigation of the effect of powder flowability on the powder spreading in additive manufacturing, Powder Technol. 413 (2023) 117997. https://doi.org/10.1016/J.POWTEC.2022.117997.

[112] S. Vock, B. Klöden, A. Kirchner, T. Weißgärber, B. Kieback, Powders for powder bed fusion: a review, Progress in Additive Manufacturing 4 (2019) 383–397. https://doi.org/10.1007/S40964-019-00078-6/TABLES/3.

[113] J.A. Slotwinski, E.J. Garboczi, P.E. Stutzman, C.F. Ferraris, S.S. Watson, M.A. Peltz, Characterization of Metal Powders Used for Additive Manufacturing, 119 (2014). https://doi.org/10.6028/jres.119.018.

[114] A. Cooke, J. Slotwinski, Properties of Metal Powders for Additive Manufacturing: A Review of the State of the Art of Metal Powder Property Testing, (n.d.). https://doi.org/10.6028/NIST.IR.7873.

[115] S. Dietrich, M. Wunderer, A. Huissel, M.F. Zaeh, A New Approach for a Flexible Powder Production for Additive Manufacturing, Procedia Manuf. 6 (2016) 88–95. https://doi.org/10.1016/J.PROMFG.2016.11.012.

[116] C. Brice, R. Shenoy, M. Kral, K. Buchannan, Precipitation behavior of aluminum alloy 2139 fabricated using additive manufacturing, Materials Science and Engineering: A 648 (2015) 9–14. https://doi.org/10.1016/J.MSEA.2015.08.088.

[117] D. Liu, D. Wu, R. Wang, J. Shi, F. Niu, G. Ma, Formation mechanism of Al-Zn-Mg-Cu alloy fabricated by laser-arc hybrid additive manufacturing: Microstructure evaluation and mechanical properties, Addit. Manuf. 50 (2022) 102554. https://doi.org/10.1016/J.ADDMA.2021.102554.

[118] J. Dawes, R. Bowerman, R. Trepleton, Introduction to the additive manufacturing powder metallurgy supply chain, Johnson Matthey Technology Review 59 (2015) 243–256. https://doi.org/10.1595/205651315X688686.

[119] P. Samal, J. Newkirk, eds., Powder Metallurgy, (2015). https://doi.org/10.31399/ASM.HB.V07.9781627081757.

[120] Y. Il Kim, D.K. Kim, I.Y. Kim, S. Cheol Park, D. Lee, B. Lee, Enhancing spreadability of hydrogenation-dehydrogenation titanium powder and novel method to characterize powder spreadability for powder bed fusion additive manufacturing, Mater. Des. 223 (2022) 111247. https://doi.org/10.1016/J.MATDES.2022.111247.

[121] K. Kassym, A. Perveen, Atomization processes of metal powders for 3D printing, Mater. Today Proc. 26 (2020) 1727–1733. https://doi.org/10.1016/J.MATPR.2020.02.364.

[122] L.V.M. Antony, R.G. Reddy, Processes for production of high-purity metal powders, JOM 55 (2003) 14–18. https://doi.org/10.1007/S11837-003-0153-4/METRICS.

[123] G. Chen, S.Y. Zhao, P. Tan, J. Wang, C.S. Xiang, H.P. Tang, A comparative study of Ti-6Al-4V powders for additive manufacturing by gas atomization, plasma rotating electrode process and plasma atomization, Powder Technol. 333 (2018) 38–46. https://doi.org/10.1016/J.POWTEC.2018.04.013.

[124] P. Sun, Z.Z. Fang, Y. Zhang, Y. Xia, Review of the Methods for Production of Spherical Ti and Ti Alloy Powder, JOM 69 (2017) 1853–1860. https://doi.org/10.1007/S11837-017-2513-5/TABLES/1.

[125] I.E. Anderson, E.M.H. White, R. Dehoff, Feedstock powder processing research needs for additive manufacturing development, Curr. Opin. Solid State Mater. Sci. 22 (2018) 8–15. https://doi.org/10.1016/J.COSSMS.2018.01.002.

[126] M.H. Sehhat, J. Chandler, Z. Yates, A review on ICP powder plasma spheroidization process parameters, Int. J. Refract. Metals Hard Mater. 103 (2022) 105764. https://doi.org/10.1016/J.IJRMHM.2021.105764.

[127] A. Vafadar, F. Guzzomi, A. Rassau, K. Hayward, Advances in Metal Additive Manufacturing: A Review of Common Processes, Industrial Applications, and Current Challenges, Applied Sciences 2021, Vol. 11, Page 1213 11 (2021) 1213. https://doi.org/10.3390/APP11031213.

[128] Z. Chen, C. Han, M. Gao, S.Y. Kandukuri, K. Zhou, A review on qualification and certification for metal additive manufacturing, Https://Doi.Org/10.1080/17452759.2021.2018938 17 (2021) 382–405. https://doi.org/10.1080/17452759.2021.2018938.

[129] G. Sander, J. Tan, P. Balan, O. Gharbi, D.R. Feenstra, L. Singer, S. Thomas, R.G. Kelly, J.R. Scully, N. Birbilis, Corrosion of Additively Manufactured Alloys: A Review, Corrosion 74 (2018) 1318–1350. https://doi.org/10.5006/2926.

[130] ISO/TC 156, Requirements for localised corrosion and environmentally assisted cracking testing of additively manufactured metals and alloys, (2022). https://www.iso.org/standard/76602.html?browse=tc (accessed September 14, 2023).

[131] ISO/TC 156, Measurement of the electrochemical critical localized corrosion temperature (E-CLCT) for Ti alloys fabricated via the additive manufacturing method, (2020). https://www.iso.org/standard/74150.html?browse=tc (accessed September 14, 2023).

[132] ISO/TC 156, Measurement of the electrochemical critical localized corrosion potential (E-CLCP) for Ti alloys fabricated via additive manufacturing method in simulated biomedical solutions, (2023). https://www.iso.org/standard/80195.html?browse=tc (accessed September 14, 2023).

[133] D. Srinivasan, Challenges in Qualifying Additive Manufacturing for Turbine Components: A Review, Transactions of the Indian Institute of Metals 74 (2021) 1107–1128. https://doi.org/10.1007/S12666-021-02199-5/TABLES/8.

[134] S. Kandukuri, · Chen Ze, Progress of Metal AM and Certification Pathway, Transactions of the Indian National Academy of Engineering 2021 6:4 6 (2021) 909–915. https://doi.org/10.1007/S41403-021-00242-X.

[135] R.P. Badrak, Corrosion Testing of Additive Manufactured Materials, (2023). https://dx.doi.org/ (accessed November 6, 2023).

[136] R. Parri, F. Lazzeri, R. Cataldi, Larderello: 100 years of geothermal power plant evolution in Italy, Geothermal Power Generation: Developments and Innovation (2016) 537–590. https://doi.org/10.1016/B978-0-08-100337-4.00019-X.

[137] S. McCoy, B. Puckett, E.H. Balance, High performance age-hardenable nickel alloys solve problems in sour oil and gas service, Stainless Steel World (n.d.).

[138] W.L. Mankins, S. Lamb, Nickel and Nickel Alloys, in: ASM Metal Handbook V2, ASM, n.d.

[139] J. Wang, T. Zhu, Y. Wu, K. Chen, X. Guo, Q. Ren, Y. Li, C. Tang, H. Yi, L. Ye, S. Xu, J. Zhang, W. Tian, L. Zhang, The effect of nano-sized precipitates on stress corrosion cracking propagation of Alloy 718 under constant loads in PWR primary water, Corros. Sci. 242 (2025) 112577. https://doi.org/10.1016/J.CORSCI.2024.112577.

[140] A. Yazdanpanah, M. Franceschi, R.I. Revilla, S. Khademzadeh, I. De Graeve, M. Dabalà, Revealing the stress corrosion cracking initiation mechanism of alloy 718 prepared by laser powder bed fusion assessed by microcapillary method, Corros. Sci. 208 (2022) 110642. https://doi.org/10.1016/J.CORSCI.2022.110642.

[141] A. Oradei-Basile, J.R.- Superalloys, undefined 1991, A current TTT diagram for wrought alloy 718, in: E.A. Loria (Ed.), Superalloys 718, 625, 706 and Various Derivatives, TMS, 2001. https://www.tms.org/Superalloys/10.7449/1991/Superalloys_1991_325_335.pdf.

[142] S. Mannan, F. Veltry, Time-Temperature-Trasformation diagram of alloy 725, in: E.A. Loria (Ed.), Superalloys 718, 625, 706 and Various Derivatives, TMS, 2001. https://www.tms.org/superalloys/10.7449/2001/01-5107-345.pdf.

[143] J. Zhang, C. Zeng, H. Zheng, C. Gu, Thermodynamic and Kinetic Analysis of TiN Precipitation in Nickel-Based Superalloys During Solidification, Materials 2024, Vol. 17, Page 5443 17 (2024) 5443. https://doi.org/10.3390/MA17225443.

[144] C.J. Todaro, M. Rashidi, R.L. Liu, S. Gao, T.P. Le, J.E. Fronda, J. Setyadji, Y.T. Tang, M. Seita, Laser powder bed fusion of high-strength and corrosion-resistant Inconel alloy 725, Mater. Charact. 194 (2022) 112454.

[145] M. Cabrini, S. Lorenzi, C. Testa, T. Pastore, F. Brevi, S. Biamino, P. Fino, D. Manfredi, G. Marchese, F. Calignano, F. Scenini, Evaluation of Corrosion Resistance of Alloy 625 Obtained by Laser Powder Bed Fusion, J. Electrochem. Soc. 166 (2019) C3399–C3408. https://doi.org/10.1149/2.0471911JES/XML.

[146] R. Yamanoğlu, E. Avcu, H. İsmail Yavuz, M. Kiraç, Ü.G. Başçi, E.F. Sevinç, E. Bayram, Effect of laser energy density on porosity and microstructural features of Inconel 625 alloy produced by selective laser melting, J Adv Manuf Eng 5 (2024) 84–93. https://doi.org/10.14744/ytu.jame.2024.00010.

[147] P. Ledwig, H. Pasiowiec, K. Cichocki, P. Lisiecka-Graca, K. Gola, R. Wróbel, B. Dubiel, Tailoring Microstructure and Mechanical Properties of Additively Manufactured Inconel 625 by Remelting Strategy in Laser Powder Bed Fusion, Metall. Mater. Trans. A Phys. Metall. Mater. Sci. 55 (2024) 2485–2508. https://doi.org/10.1007/S11661-024-07412-W/FIGURES/14.

[148] G. Sander, J. Tan, P. Balan, O. Gharbi, D.R. Feenstra, L. Singer, S. Thomas, R.G. Kelly, J.R. Scully, N. Birbilis, Corrosion of Additively Manufactured Alloys: A Review, Corrosion 74 (2018) 1318–1350. https://doi.org/10.5006/2926.

[149] J.R. Poulin, A. Kreitcberg, V. Brailovski, Effect of hot isostatic pressing of laser powder bed fused Inconel 625 with purposely induced defects on the residual porosity and fatigue crack propagation behavior, Addit. Manuf. 47 (2021) 102324. https://doi.org/10.1016/J.ADDMA.2021.102324.

[150] W.H. Kan, L.N.S. Chiu, C.V.S. Lim, Y. Zhu, Y. Tian, D. Jiang, A. Huang, A critical review on the effects of process-induced porosity on the mechanical properties of alloys fabricated by laser powder bed fusion, J. Mater. Sci. 57 (2022) 9818–9865. https://doi.org/10.1007/S10853-022-06990-7/FIGURES/11.

[151] C. Suwanpreecha, A. Manonukul, C. Suwanpreecha, A. Manonukul, A Review on Material Extrusion Additive Manufacturing of Metal and How It Compares with Metal Injection Moulding, Metals 2022, Vol. 12, 12 (2022). https://doi.org/10.3390/MET12030429.

[152] S.S. Joshi, S. Sharma, S. Mazumder, M. V. Pantawane, N.B. Dahotre, Solidification and microstructure evolution in additively manufactured H13 steel via directed energy deposition: Integrated experimental and computational approach, J. Manuf. Process. 68 (2021) 852–866. https://doi.org/10.1016/J.JMAPRO.2021.06.009.

[153] U. Scipioni Bertoli, G. Guss, S. Wu, M.J. Matthews, J.M. Schoenung, In-situ characterization of laser-powder interaction and cooling rates through high-speed imaging of powder bed fusion additive manufacturing, Mater. Des. 135 (2017) 385–396. https://doi.org/10.1016/J.MATDES.2017.09.044.

[154] A. Sukumaran, R.K. Gupta, V. Anil Kumar, Effect of Heat Treatment Parameters on the Microstructure and Properties of Inconel-625 Superalloy, Journal of Materials Engineering and Performance 2017 26:7 26 (2017) 3048–3057. https://doi.org/10.1007/S11665-017-2774-8.

[155] S. Floreen, G.E. Fuchs, W.J. Yang, The Metallurgy of Alloy 625, Superalloys 718, 625, 706 and Various Derivatives (1994) (1994) 13–37. https://doi.org/10.7449/1994/SUPERALLOYS_1994_13_37.

[156] P. Mohammadpour, H. Yuan, A.B. Phillion, Microstructure evolution of Inconel 625 alloy during single-track Laser Powder Bed Fusion, Addit. Manuf. 55 (2022) 102824. https://doi.org/10.1016/J.ADDMA.2022.102824.

[157] T.E. Abioye, P.K. Farayibi, A.T. Clare, A comparative study of Inconel 625 laser cladding by wire and powder feedstock, Materials and Manufacturing Processes 32 (2017) 1653–1659. https://doi.org/10.1080/10426914.2017.1317787.

[158] D. Gurianov, S. Fortuna, S. Tarasov, V. Semenchuk, N. Shamarin, A. Chumaevskii, V. Rubtsov, A.M. Korsunsky, E. Kolubaev, D. Gurianov, S. Fortuna, S. Tarasov, V. Semenchuk, N. Shamarin, A. Chumaevskii, V. Rubtsov, A.M. Korsunsky, E. Kolubaev, The Comparison of Microstructure, Phase Composition and Mechanical Properties of Inconel 625 Alloys Obtained by Wire Arc and Wire Electron Beam Additive Manufacturing, Crystals 2025, Vol. 15, 15 (2025) 848. https://doi.org/10.3390/CRYST15100848.

[159] O.M. Akselsen, R. Bjørge, H.W. Ånes, X. Ren, B. Nyhus, O.M. Akselsen, R. Bjørge, H.W. Ånes, X. Ren, B. Nyhus, Microstructure and Properties of Wire Arc Additive Manufacturing of Inconel 625, Metals 2022, Vol. 12, 12 (2022). https://doi.org/10.3390/MET12111867.

[160] G. Marchese, M. Lorusso, S. Parizia, E. Bassini, J.W. Lee, F. Calignano, D. Manfredi, M. Terner, H.U. Hong, D. Ugues, M. Lombardi, S. Biamino, Influence of heat treatments on microstructure evolution and mechanical properties of Inconel 625 processed by laser powder bed fusion, Materials Science and Engineering: A 729 (2018) 64–75. https://doi.org/10.1016/J.MSEA.2018.05.044.

[161] Y.N. Aditya, S. Rohila, S. Hosseinimehr, D. Ester, M.J. Benoit, Elucidating the effect of sintering time on the process-structure-property relationship of Inconel 625 produced by metal extrusion additive manufacturing, Materials Science and Engineering: A 944 (2025) 148880. https://doi.org/10.1016/J.MSEA.2025.148880.

[162] P.D. Enrique, E. Marzbanrad, Y. Mahmoodkhani, Z. Jiao, E. Toyserkani, N.Y. Zhou, Surface modification of binder-jet additive manufactured Inconel 625 via electrospark deposition, Surf. Coat. Technol. 362 (2019) 141–149. https://doi.org/10.1016/j.surfcoat.2019.01.108.

[163] A. Mostafaei, Y. Behnamian, Y.L. Krimer, E.L. Stevens, J.L. Luo, M. Chmielus, Brief data overview of differently heat treated binder jet printed samples made from argon atomized alloy 625 powder, Data Brief 9 (2016) 556. https://doi.org/10.1016/J.DIB.2016.09.042.

[164] L. Jiang, W.Z. Zhang, Z.F. Xu, H.F. Huang, X.X. Ye, B. Leng, L. Yan, Z.J. Li, X.T. Zhou, M2C and M6C carbide precipitation in Ni-Mo-Cr based superalloys containing silicon, Mater. Des. 112 (2016) 300–308. https://doi.org/10.1016/J.MATDES.2016.09.075.

[165] N. Lecis, M. Mariani, R. Beltrami, L. Emanuelli, R. Casati, M. Vedani, A. Molinari, Effects of process parameters, debinding and sintering on the microstructure of 316L stainless steel produced by binder jetting, Materials Science and Engineering: A 828 (2021) 142108. https://doi.org/10.1016/J.MSEA.2021.142108.

[166] K. Pengikatan dan Pensinteran ke atas Sifat dan Rintangan Kakisan Acuan Suntikan Serbuk, L. -Keluli Tahan Karat MUHAMMAD RAFI RAZA, F. Ahmad, N. Muhamad, A. Bakar Sulong, M. Omar, Effects of Debinding and Sintering Atmosphere on Properties and Corrosion Resistance of Powder Injection Molded 316 L-Stainless Steel, Sains Malays. 46 (2017) 285–293. https://doi.org/10.17576/jsm-2017-4602-13.

[167] P. Nandwana, R. Kannan, D. Siddel, Microstructure evolution during binder jet additive manufacturing of H13 tool steel, Addit. Manuf. 36 (2020) 101534. https://doi.org/10.1016/J.ADDMA.2020.101534.

[168] B. Levenfeld, A. Várez, J.M. Torralba, Effect of residual carbon on the sintering process of M2 high speed steel parts obtained by a modified metal injection molding process, Metallurgical and Materials Transactions A 2002 33:6 33 (2002) 1843–1851. https://doi.org/10.1007/S11661-002-0192-4.

[169] A. Schnell, C. Colin, Debinding, A Key Stage In The Manufacture Of Inconel 718 Parts By Metal Binder Jetting, (n.d.). https://doi.org/10.2497/jjspm.16A-T7-26.

[170] M. Cabrini, S. Lorenzi, C. Testa, F. Brevi, S. Biamino, P. Fino, D. Manfredi, G. Marchese, F. Calignano, T. Pastore, Microstructure and Selective Corrosion of Alloy 625 Obtained by Means of Laser Powder Bed Fusion, Materials 2019, Vol. 12, Page 1742 12 (2019) 1742. https://doi.org/10.3390/MA12111742.

[171] K.D. Ralston, N. Birbilis, Effect of Grain Size on Corrosion: A Review, Corrosion 66 (2010) 075005–1. https://doi.org/10.5006/1.3462912.

[172] P. Ganesan, C.M. Renteria, J.R. Crum, Versatile Corrosion Resistance of INCONEL" alloy 625 in Various Aqueous and Chemical Processing Environments, (n.d.).

[173] G.D. Smith, S.J. Patel, THE ROLE OF NIOBIUM IN WROUGHT PRECIPITATION-HARDENED NICKEL-BASE ALLOYS, (n.d.).

[174] K. Gola, P. Ledwig, B. Dubiel, Effect of Microstructure of Additively Manufactured Inconel 625 on Long-Term Corrosion Behaviour in Sulfuric Acid Media, JOM 75 (2023) 1242–1250. https://doi.org/10.1007/S11837-023-05708-7/TABLES/2.

[175] W. Zhang, Y. Xu, Y. Shi, G. Su, Y. Gu, K. Volodymyr, Intergranular corrosion characteristics of high-efficiency wire laser additive manufactured Inconel 625 alloys, Corros. Sci. 205 (2022) 110422. https://doi.org/10.1016/J.CORSCI.2022.110422.

[176] Vrije Universiteit Brussel Methods-On the Application of Ambient Scanning Kelvin Probe Force Microscopy to Understand Micro-Galvanic Corrosion Phenomena: Interpretation and Challenges Revilla, Reynier I, (n.d.). https://doi.org/10.1149/1945-7111/acafab.

[177] C. Örnek, C. Leygraf, J. Pan, On the Volta potential measured by SKPFM – fundamental and practical aspects with relevance to corrosion science, Corrosion Engineering, Science and Technology 54 (2019) 185–198. https://doi.org/10.1080/1478422X.2019.1583436.

[178] P. Schmutz, G.S. Frankel, Corrosion Study of AA2024-T3 by Scanning Kelvin Probe Force Microscopy and In Situ Atomic Force Microscopy Scratching, J. Electrochem. Soc. 145 (1998) 2295–2306. https://doi.org/10.1149/1.1838634/XML.

[179] P. Schmutz, G.S. Frankel, Characterization of AA2024-T3 by Scanning Kelvin Probe Force Microscopy, J. Electrochem. Soc. 145 (1998) 2285–2295. https://doi.org/10.1149/1.1838633/XML.

[180] M.C. Örnek, J. Walton, T. Hashimoto, al -, C. Örnek, C. Leygraf, J. Pan, In-Situ Time-Lapse SKPFM Investigation of Sensitized AA5083 Aluminum Alloy to Understand Localized Corrosion, J. Electrochem. Soc. 167 (2020) 141502. https://doi.org/10.1149/1945-7111/ABC30D.

[181] M. Iannuzzi, K.L. Vasanth, G.S. Frankel, Unusual Correlation between SKPFM and Corrosion of Nickel Aluminum Bronzes, J. Electrochem. Soc. 164 (2017) C488–C497. https://doi.org/10.1149/2.0391709JES/XML.

[182] J.C. Lourenço, L.P. Souza, M.I.S.T. Faria, C.A. Nunes, C.R. Tomachuk, M.A. Baker, Influence of the iron content on the microstructure and electrochemical behavior of as-cast modified Inconel 625, Corros. Sci. 193 (2021) 109892. https://doi.org/10.1016/J.CORSCI.2021.109892.

[183] Q. Guo, Y. Li, J. Qian, H. Yu, C. Chen, Study of the pitting corrosion at welding joints of Inconel 625 alloy under high temperature and high H2S/CO2 partial pressure, Int. J. Electrochem. Sci. 12 (2017) 8929–8943. https://doi.org/10.20964/2017.10.46.

[184] P. Pedeferri, Corrosion Science and Engineering , Springer, Cham, Milano, 2018. https://doi.org/10.1007/978-3-319-97625-9_4.

[185] J. Korb, D. Olson, ASM Metals Handbook, ASM International, n.d.

[186] A. Mishra, Performance of corrosion-resistant alloys in concentrated acids, Acta Metallurgica Sinica (English Letters) 30 (2017) 306–318. https://doi.org/10.1007/S40195-017-0538-Y/TABLES/3.

[187] HAYNES® 625 - Haynes International, (n.d.). https://haynesintl.com/en/alloys/alloy-portfolio/high-temperature-alloys/haynes-625/#iso-corrosion-diagrams (accessed November 27, 2025).

[188] F.S. Gobber, P.C. Priarone, A. Pennacchio, M. Actis Grande, Effect of inert gas pressure on the properties and carbon footprint of UNS S32760 powders made from waste materials by gas atomization, Journal of Materials Research and Technology 33 (2024) 8814–8828. https://doi.org/10.1016/J.JMRT.2024.11.195.

[189] G. Locatelli, S. Bocchi, M. Quarto, G.D.' Urso, Laser powder bed fusion of atomized industrial waste-derived Inconel 725 alloy powders: A machine learning-

assisted process optimization Materials Science in Additive Manufacturing, 5 (2026) 1. https://doi.org/10.36922/MSAM025320072.

[190] L.E. Shoemaker, ALLOYS 625 AND 725: TRENDS IN PROPERTIES AND APPLICATIONS, (n.d.).

[191] J.J. Debarbadillo, S.K. Mannan, Alloy 718 for oilfield applications, JOM 64 (2012) 265–270. https://doi.org/10.1007/S11837-012-0238-Z.

[192] M.S. Hazarabedian, M. Iannuzzi, The role of nano-sized intergranular phases on nickel alloy 725 brittle failure, Npj Materials Degradation 2021 5:1 5 (2021) 1–9. https://doi.org/10.1038/s41529-021-00185-2.

[193] R.G. Samvel'yan, E.S. Abovyan, S.G. Agbalyan, N.N. Manukyan, M.S. Sakanyan, X-ray diffraction examination of the process of thermal stabilization of powder thermal bimetals, in: Soviet Powder Metallurgy and Metal Ceramics, Kluwer Academic Publishers-Plenum Publishers, 1991: pp. 606–609. https://doi.org/10.1007/BF00794656/METRICS.

[194] Z. Chen, P. Wei, H. Chen, X. Chen, Y. Ruan, W. Zhou, S. Lu, Z. Chen, P. Wei, H. Chen, X. Chen, Y. Ruan, W. Zhou, S. Lu, Laser Powder Bed Fusion of K418 Superalloy: Process, Microstructure, Texture Feature, and Mechanical Property, Metals 2022, Vol. 12, 12 (2022). https://doi.org/10.3390/MET12040611.

[195] HENTHORNE M, DEBOLD TA, Intergranular Corrosion Resistance of Carpenter 20Cb-3, Corrosion 27 (1971) 255–262. https://doi.org/10.5006/0010-9312-27.6.255.

[196] R.B. LEONARD, Thermal Stability of Hastelloy Alloy C-276, Corrosion 25 (1969) 222–232. https://doi.org/10.5006/0010-9312-25.5.222.

[197] M.A. STREICHER, Relationship of Heat Treatment And Microstructure to Corrosion Resistance In Wrought Ni-Cr-Mo Alloys, Corrosion 19 (1963) 272t–284t. https://doi.org/10.5006/0010-9312-19.8.272.

[198] M.A. Streicher, Effect of Composition and Structure on Crevice, Intergranular, and Stress Corrosion of Some Wrought Ni-Cr-Mo Alloys, CORROSION 32 (1976) 79–93. https://doi.org/10.5006/0010-9312-32.3.79.

[199] M.H. BROWN, The Relationship of Heat Treatment to the Corrosion Resistance of Stainless Alloys, Corrosion 25 (1969) 438–443. https://doi.org/10.5006/0010-9312-25.10.438.

[200] **G. Mori, S. Sutthiruangwong, M. Czerny, T. Partlic, Metallurgical and Surface Influence on the Corrosion Resistance of Ni-Cr-Mo Alloys According to ASTM G 28, Corrosion 60 (2004) 1082–1091. https://doi.org/10.5006/1.3299221.**

[201] **B. Seo, H.K. Park, C.S. Park, K. Park, Effect of alloying elements on corrosion properties of high corrosion resistant titanium alloys in high concentrated sulfuric acid, Mater. Today Commun. 34 (2023) 105131. https://doi.org/10.1016/J.MTCOMM.2022.105131.**

[202] **H.G. Nelson, D.P. Williams, J.E. Stein, Environmental hydrogen embrittlement of an α-β titanium alloy: Effect of microstructure, Metallurgical Transactions 3 (1972) 473–479. https://doi.org/10.1007/BF02642051/METRICS.**

[203] **S.Y. Yu, J.R. Scully, C.M. Vitus, Influence of Niobium and Zirconium Alloying Additions on the Anodic Dissolution Behavior of Activated Titanium in HCl Solutions, J. Electrochem. Soc. 148 (2001) B68. https://doi.org/10.1149/1.1337605.**

[204] **James D. Destefani, Introduction to Titanium and Titanium Alloys, in: ASM Metal Handbook, 1990: pp. 1770–1782. https://doi.org/https://doi.org/10.31399/asm.hb.v02.9781627081627.**

[205] **R.W. Schutz, Corrosion of Titanium and Titanium Alloys, in: Jr. Stephen D. Cramer; Bernard S. Covino (Ed.), Corrosion: Materials, ASM International, 2005: pp. 252–299. https://doi.org/10.31399/ASM.HB.V13B.A0003822.**

[206] **D. Eliezer, T.H. Böllinghaus, Hydrogen effects in titanium alloys, Gaseous Hydrogen Embrittlement of Materials in Energy Technologies: The Problem, Its Characterisation and Effects on Particular Alloy Classes (2012) 668–706. https://doi.org/10.1533/9780857093899.3.668.**

[207] **R. Thomas, Titanium in the geothermal industry, Geothermics 32 (2003) 679–687. https://doi.org/10.1016/J.GEOTHERMICS.2003.08.004.**

[208] **W.D. MacDonald, J.S. Grauman, Development of New Titanium Alloys for Use in Aggressive Geothermal Environments, (2019). https://dx.doi.org/ (accessed December 26, 2025).**

[209] **A.I. Thorhallsson, S.N. Karlsdottir, Corrosion Behaviour of Titanium Alloy and Carbon Steel in a High-Temperature, Single and Mixed-Phase, Simulated Geothermal Environment Containing H2S, CO2 and HCl, Corrosion and Materials Degradation 2021, Vol. 2, Pages 190-209 2 (2021) 190–209. https://doi.org/10.3390/CMD2020011.**

[210] S.D. Cramer, J.P. Carter, Corrosion in Geothermal Brines of the Salton Sea Known Geothermal Resource Area, ASTM Special Technical Publication STP 717 (1980) 113–141. https://doi.org/10.1520/STP30068S.

[211] L.M. Gammon, R.D. Briggs, J.M. Packard, K.W. Batson, R. Boyer, C.W. Domby, Metallography and Microstructures of Titanium and Its Alloys, in: George F. Vander Voort (Ed.), Metallography and Microstructures, ASM International, 2004: pp. 899–917. https://doi.org/10.31399/ASM.HB.V09.A0003779.

[212] Titanium Metals Corporation (TIMET), Corrosion Resistance of Titanium, in: Timet technical publication, 1999: pp. 25–30.

[213] R. Mitchell, A. Short, T. Pasang, G. Littlefair, Characteristics of Electron Beam Welded Ti & Ti Alloys, Adv. Mat. Res. 275 (2011) 81–84. https://doi.org/10.4028/WWW.SCIENTIFIC.NET/AMR.275.81.

[214] W.A. Baeslack III, Martin Marietta, C.E. Cross, Selection and Weldability of Conventional Titanium Alloys, in: D.L. Olson, T.A. Siewert, S. Liu, G.R. Edwards (Eds.), ASM Handbook Volume 6: Welding, Brazing, and Soldering, 2003: pp. 1289–1330.

[215] J.E. Hack, G.R. Leverant, Influence of microstructure on the susceptibility of titanium alloys to internal hydrogen embrittlement, Metallurgical Transaction A 13 (1982) 1729–1738. https://doi.org/10.1007/BF02647828/METRICS.

[216] Y. Liu, Z.H. Ren, J. Liu, R.F. Schaller, E. Asselin, Electrochemical Investigation and Identification of Titanium Hydrides Formed in Mixed Chloride Sulfuric Acid Solution, J. Electrochem. Soc. 166 (2019) C3096–C3105. https://doi.org/10.1149/2.0121911JES/XML.

[217] H.M. Tawancy, On the Hydrogen Embrittlement of Commercially Pure Alpha Titanium: An Example from the Petrochemical Industry, J. Mater. Eng. Perform. 26 (2017) 504–513. https://doi.org/10.1007/S11665-016-2464-Y/FIGURES/14.

[218] T. Pasang, Y. Tao, M. Azizi, O. Kamiya, M. Mizutani, W. Misiolek, Welding of titanium alloys, in: The 2nd International Conference on Precision Machinery and Manufacturing Technology, Matec web conferences, 2017. https://doi.org/10.1051/matecconf/201712300001.

[219] A. Karpagaraj, N. Siva shanmugam, K. Sankaranarayanasamy, Some studies on mechanical properties and microstructural characterization of automated TIG welding of thin commercially pure titanium sheets, Materials Science and Engineering: A 640 (2015) 180–189. https://doi.org/10.1016/J.MSEA.2015.05.056.

[220] H. Zhang, C. Leygraf, L. Wen, F. Huang, H. Chang, Y. Jin, The formation of hydride and its influence on Ti–6Al–4V alloy fracture behavior, Int. J. Hydrogen Energy 48 (2023) 36169–36184. https://doi.org/10.1016/J.IJHYDENE.2023.05.226.

[221] A.J. McEvily, Titanium Alloys: Atlas of Fractographs, in: D.L. Bagnoli (Ed.), ASM Handbook, ASM INTERNATIONAL, 2003. https://www.asminternational.org/results/-/journal_content/56/06048G/PUBLICATION/.

[222] H.G. Nelson, D.P. Williams, J.E. Stein, Environmental hydrogen embrittlement of an α-β titanium alloy: Effect of microstructure, Metallurgical Transactions 3 (1972) 473–479. https://doi.org/10.1007/BF02642051/METRICS.

[223] E Ranatowski, Weldability of titanium and its alloys-progress in joining, Advances in Materials 8 (2008). https://doi.org/10.2478/V10077-008-0033-2.

[224] C.E. Cross, D. Eliezer, T. Böllinghaus, The Role of Hydrogen in Titanium Alloy Weldments, (n.d.).

[225] F.H. Beck, EFFECT OF HYDROGEN ON M _M_ PROPERTIES OF TITABIL_ AND ITS ALLOYS, (n.d.).

[226] J.R. Myers, H.B. Bomberger, F.H. Froes, Corrosion Behavior and Use of Titanium and Its Alloys, Journal of The Minerals, Metals & Materials Society 36 (1984) 50–60. https://doi.org/10.1007/BF03338589/METRICS.

[227] R.T. Webster, Welding of Titanium Alloys, in: David LeRoy Olson, Thomas A. Siewert, Stephen Liu, Glen R. Edwards (Eds.), Welding, Brazing, and Soldering, ASM International, 1993: pp. 783–786. https://doi.org/10.31399/ASM.HB.V06.A0001440.

[228] B. Han, M. Marya, An Evaluation of the Mechanical Properties and Sulfide Stress Cracking of Additively Manufactured Alloy Ti-6Al-2Sn-4Zr-6Mo for Sour Geothermal Use, (2025) 1–15. https://doi.org/10.5006/C2025-00101.

[229] T. Schott, F. Liautaud, Monitoring and mitigating corrosion in geothermal systems, Materials and Corrosion 73 (2022) 1916–1942. https://doi.org/10.1002/MACO.202213359;JOURNAL:JOURNAL:15214176;WGROUP:STRING:PUBLICATION.

[230] A. Emiralioğlu, R. Ünal, Additive manufacturing of gamma titanium aluminide alloys: a review, J. Mater. Sci. 57 (2022) 4441–4466. https://doi.org/10.1007/S10853-022-06896-4/TABLES/1.

[231] S. Biamino, A. Penna, U. Ackelid, S. Sabbadini, O. Tassa, P. Fino, M. Pavese, P. Gennaro, C. Badini, Electron beam melting of Ti–48Al–2Cr–2Nb alloy: Microstructure and mechanical properties investigation, Intermetallics (Barking). 19 (2011) 776–781. https://doi.org/10.1016/J.INTERMET.2010.11.017.

[232] M. Terner, S. Biamino, P. Epicoco, A. Penna, O. Hedin, S. Sabbadini, P. Fino, M. Pavese, U. Ackelid, P. Gennaro, F. Pelissero, C. Badini, Electron beam melting of high niobium containing TiAl alloy: Feasibility investigation, Steel Res. Int. 83 (2012) 943–949. https://doi.org/10.1002/SRIN.201100282;WGROUP:STRING:PUBLICATION.

[233] B. Vrancken, L. Thijs, J.P. Kruth, J. Van Humbeeck, Heat treatment of Ti6Al4V produced by Selective Laser Melting: Microstructure and mechanical properties, J. Alloys Compd. 541 (2012) 177–185. https://doi.org/10.1016/J.JALLCOM.2012.07.022.

[234] M. Cabrini, A. Carrozza, S. Lorenzi, T. Pastore, C. Testa, D. Manfredi, P. Fino, F. Scenini, Influence of surface finishing and heat treatments on the corrosion resistance of LPBF-produced Ti-6Al-4V alloy for biomedical applications, J. Mater. Process. Technol. 308 (2022) 117730. https://doi.org/10.1016/J.JMATPROTEC.2022.117730.

[235] Y. Lu, H.B. Tang, Y.L. Fang, D. Liu, H.M. Wang, Microstructure evolution of sub-critical annealed laser deposited Ti–6Al–4V alloy, Mater. Des. 37 (2012) 56–63. https://doi.org/10.1016/J.MATDES.2011.12.016.

[236] A. Carrozza, A. Aversa, P. Fino, M. Lombardi, Towards customized heat treatments and mechanical properties in the LPBF-processed Ti-6Al-2Sn-4Zr-6Mo alloy, Mater. Des. 215 (2022) 110512. https://doi.org/10.1016/J.MATDES.2022.110512.

[237] B. Dutta, F.H. (Sam) Froes, The Additive Manufacturing (AM) of titanium alloys, Metal Powder Report 72 (2017) 96–106. https://doi.org/10.1016/J.MPRP.2016.12.062.

[238] L. Jiang, L. Lan, C. Bai, H. Wang, S. Gao, B. He, Research progress on powder bed fusion additive manufacturing of TiAl-based alloy, The International Journal of Advanced Manufacturing Technology 2024 133:3 133 (2024) 1045–1061. https://doi.org/10.1007/S00170-024-13843-X.

[239] H. Clemens, S. Mayer, Design, processing, microstructure, properties, and applications of advanced intermetallic TiAl alloys, Adv. Eng. Mater. 15 (2013) 191–

215. https://doi.org/10.1002/ADEM.201200231;PAGE:STRING:ARTICLE/CHAPTER.

[240] T.C. Dzogbewu, Additive manufacturing of TiAl-based alloys, Manuf. Rev. (Les Ulis). 7 (2020) 35. https://doi.org/10.1051/MFREVIEW/2020032.

[241] J.P. Frayret, A. Caprani, T. Jaszay, F. Priem, Influence of Aluminum and Vanadium on the Anodic Dissolution of Ti-Al and Ti-V Binary Alloys in Concentrated Hydrochloric Acid, Corrosion 41 (1985) 656–664. https://doi.org/10.5006/1.3583000.

[242] S.Y. Yu, J.R. Scully, Corrosion and Passivity of Ti-13% Nb-13% Zr in Comparison to Other Biomedical Implant Alloys, Corrosion 53 (1997) 965–976. https://doi.org/10.5006/1.3290281.

[243] J. Lee, W. Gao, Z. Li, Y. He, Corrosion behaviour of Ti3Al and Ti3Al–11 at.% Nb intermetallics, Mater. Lett. 57 (2003) 1528–1538. https://doi.org/10.1016/S0167-577X(02)01018-2.

[244] A.K. Shukla, R. Balasubramaniam, S. Bhargava, Effect of replacement of V by Fe and Nb on passive film behavior of Ti–6Al–4V in simulated body fluid conditions, J. Alloys Compd. 389 (2005) 144–152. https://doi.org/10.1016/J.JALLCOM.2004.08.005.

[245] M. Kobayashi, Y. Araya, S.Y. Fujiyama S-cinayama, H. Uno, STUDY ON CREVICE CORROSION OF TITANIUM, (n.d.).

[246] H. Satoh, K. Shimogori, F. Kamikubo, The Crevice Corrosion Resistance of Some Titanium Materials A REVIEW OF THE BENEFICIAL EFFECTS OF PALLADIUM, Platinum Metals Rev (1987) 115–121.

[247] I. Leusbrock, S.J. Metz, G. Rexwinkel, G.F. Versteeg, The solubility of magnesium chloride and calcium chloride in near-critical and supercritical water, J. Supercrit. Fluids 53 (2010) 17–24. https://doi.org/10.1016/J.SUPFLU.2009.12.015.